Interface- Induced Ferromagnetism and Superconductivity in Two-Dimensional Electron Gases

Dissertation

zur Erlangung des Doktorgrades der Naturwissenschaften

(Dr. rer. nat.)

der

Naturwissenschaftlichen Fakultat II

Chemie, Physik und Mathematik

der Martin-Luther- Universität

Halle- Wittenberg

Vorgelegt von

Herrn **Mostafa Ibrahim Shehata Marzouk**

Gutachter:

Prof. Dr. Stuart S. P. Parkin

Prof. Dr. Bharat Jalan

Prof. Dr. Kathrin Dörr

Tag der öffentlichen Verteidigung: 14.05.2025

Dedication

To my beloved mother who never stops her valuable unlimited support and sacrifice for keeping us moving in the life, and to my wife Mirna the partner of my journey, as well as to my sister, and my brother. I deeply thank them all for their unconditional support and unwavering faith in me, which has strengthened my resilience through life's challenges. I wish this work can be a kind of admitting their appreciated contributions to my life, without them I would never be able to keep moving. I particularly thank Mirna for her continuous support.

To the memory of Nobel Prize laureate Ahmed H. Zewail, whose brilliance and contributions continue to inspire a love for science and a commitment to advancing society through the application of scientific and technological principles.

Mostafa I. S. Marzouk,

Halle (Saale), Germany

October 25th, 2024

Table of Contents

Abbreviations

List of abbreviations

AHE: Anomalous Hall effect

AF: Antiferromagnetic/Antiferromagnetism

AFM: Atomic Force Microscopy

ARPES: Angle resolved photoelectron spectroscopy

BG: Band gap

DFT: Density functional theory

DMI: Dzyaloshinski-Moriya interaction

DOS: Density of states

FFT: Fast Fourier transform

FM: Ferromagnetic/Ferromagnetism

GL: Ginzburg-Landau

GPA: Geometrical phase analysis algorithm

H_c: Critical field

K- Cell: Knudsen cell

KTO: $KTaO_3$

LAO: $LaAlO_3$

LEED: Low energy-electron diffraction

LFO: $LaFeO_3$

LiTO: $LiTaO_3$

LTO: $LaTiO_3$

MBE: Molecular Beam Epitaxy

MR: Magnetoresistance

OHE: Ordinary Hall effect

PDOS: Projected density of states

PO_3: Pressure of Ozone

PPMS: Physical property measurement system

RHEED: Reflection high-energy electron diffraction

RSM: Reciprocal space mapping

RRR: Residual resistivity ratio

SEM: Scanning electron microscopy

SQUID: Superconducting quantum interference device

STEM: Scanning transmission electron microscopy

STO: $SrTiO_3$

T_c: Superconducting critical (transition) temperature

T_C: Curie temperature

TEM: Transmission electron microscopy

t_{LTO}: Thickness of $LaTiO_3$ layer

T_N: Néel temperature

T_s: Substrate temperature

VSM: Vibrating sample magnetometer

XAS: X-ray absorption spectra

XPS: X-ray photoemission spectroscopy

XRD: X-ray diffraction

XRR: X-ray reflectivity

XMCD: X-ray magnetic circular dichroism

ρ_{AHE}: Anomalous Hall resistivity

$\boldsymbol{\theta_{tilt}}$: Tilting angle of the TiO_6 octahedral

Abstract

"Interface is a device," as Nobel prize laureate Herbert Kroemer famously stated, capturing the idea that interfaces can fundamentally alter material properties. Indeed, engineered interfaces often give rise to exotic phenomena which are not present in the pristine bulk material. Oxide thin films serve as an exceptional platform for such interface engineering, allowing the fine-tuning and control of the physical properties of layered systems. The research of oxides gained significant interest particularly after in 1937 when N.F. Mott observed strong electron-electron correlations in Mott insulator oxides such as NiO and MnO. This interest was then intensified with the discovery of high-temperature superconductivity in CuO_2-based cuprates, positioning oxides as a prominent research focus within condensed matter physics community. Oxide interfaces have proven to host novel two-dimensional electron conduction, analogous to the two-dimensional electron gases (2DEGs) in typical semiconductors. The discovery of 2DEGs at oxide interfaces has since underscored the critical role of interfaces in advancing the field of oxide materials towards many significant applications in electronics and spin-electronics industry. The 2DEGs at oxide interfaces can provide numerous advantages which are absent in the case of semiconductor- based 2DEGs. One of such advantages is the high sheet carrier density which is very crucial for achieving high current density necessary for the power and memory applications. Oxide 2DEGs exhibited recently, ferromagnetism, ferroelectricity, superconductivity and strong spin-orbit coupling as reported in the last decade mainly at $SrTiO_3$ and at $KTaO_3$ interfaces.

In this thesis, we studied the emerging phenomena at the oxide interfaces grown by state-of-the- art molecular beam epitaxy (MBE) with a focus mainly on the two-dimensional electron gases formed at the $KTaO_3$ interfaces. We observed the evolution of ferromagnetism at the $KTaO_3$ (110)/ $LaTiO_3$ and $KTaO_3$ (111)/ $LaTiO_3$ 2DEGs, remarkably these ferromagnetic 2DEGs preserve high- electron mobility as high as (250 cm^2/V. s at 2 K and 20 cm^2/V. s at 300 K). The ferromagnetism is evidenced by anomalous Hall hysteresis loops, butterfly magnetoresistance hysteresis loops (down to 1.7 K), out- of -plane magnetization hysteresis

loops and x-ray magnetic circular dichroism (XMCD) measurements at 2 K. Furthermore, the density functional theory calculations showed that the TiO_6 under tilting is one responsible source of the ferromagnetism. The anomalous Hall effect measurements revealed that the 2DEGs at KTO (111)/$LaTiO_3$ interfaces exhibit significantly higher anomalous Hall resistivity than those at KTO (110)/$LaTiO_3$. Our ferromagnetic 2DEGs also demonstrate superconductivity onset at a transition temperature of approximately 1 K, particularly in the $KTaO_3$ (111)/$LaTiO_3$ interface. Notably, our findings reveal a coexistence of ferromagnetism and superconductivity in the KTO (111)/LTO 2DEGs, where both the superconducting transition temperature and supercurrent display non-monotonic behaviors depending on the $LaTiO_3$ layer thickness. Ferromagnetic and superconducting states appear to compete in thinner $LaTiO_3$ layers, while they coexist in thicker layers. Interestingly, the phase diagram of the superconducting transition temperature versus $LaTiO_3$ thickness resembles a dome-shaped curve, akin to the doping-dependent phase diagram observed in cuprates. This thesis suggests that the coexistence of superconductivity and ferromagnetism in the two-dimensional electron gases at $KTaO_3$/$LaTiO_3$ interfaces may point to unconventional superconductivity.

Additionally, this thesis explores the proximity effect of the 2DEG layer ($KTaO_3$/$LaTiO_3$) on the tuning of superconducting properties at the interface with a disordered superconducting TiN overlayer. This has been achieved by varying the $LaTiO_3$ thickness in the 2DEG. Interestingly, we observed that samples with lower superconducting transition temperatures (thicker $LaTiO_3$) exhibited higher upper critical field values. This could be explained by the evoulution of a new superconducinng layer at the oxide/nitride interface.

1. Introduction and fundamentals

This chapter provides a concise and conclusive explanation of the fundamental physics and background information relevant to this study. We cover the essential theoretical principles that underpin the phenomena observed in this work.

1.1. **Mott Insulators**

Conventional band theory successfully explains various solid-state materials using band diagrams, but it falls short in describing Mott insulators [1-4]. Unlike predictions made by band theory, which suggests that various materials which has odd number of electrons per unit cell should conduct electricity, the Mott materials violate this theory and are found to be insulating, particularly at low temperatures. This discrepancy arises from the strong electron correlations and many-body interactions that simple band theory does not account for as Nevil Mott explained in the case of NiO. Mott insulators are not conducting because of the strong repulsion between electrons in adjacent atoms, see Fig.1.1 for a schematic diagram of both cases. For example, consider a 1D chain of interacting hydrogen atoms, where each electron is localized in an atom and has either an up or down spin. If we consider the correlation between neighboring atoms, one electron can hop (tunnel) to an adjacent atom under certain conditions. The adjacent atom then holds two electrons with opposite spins, subjected to a Coulomb repulsion U. This repulsion is the energy cost for the electron's movement from its original atom. For hydrogen atoms, this hopping cost, according to the Hubbard model [5], is approximately 12.8 eV, indicating an insulating behavior. However, when the bandwidth of the inter-atomic interaction exceeds U, the orbitals of adjacent atoms overlap, potentially leading to conductive behavior at certain temperatures. This model effectively explains the band diagram mechanisms of Mott insulators. The Mott insulators are commonly hosted in strong correlated transition metal oxide and chalcogenides materials enabling the metal to insulator transitions and mostly accompanied with the antiferromagnetism [3]. Among these materials, $LaTiO_3$, $LaNiO_3$, VO_2, NiO are typical examples of Mott insulators. The material

must achieve one criterion to be called Mott insulator; in other words, the relation between the electron density N and the Bohr radius B_r must satisfy the following: $N^{1/3} \times B_r \approx 0.2$. The Mott transition is usually a first order discontinuous transition unless some magnetic frustrations occurs at low temperatures such as in spin-liquids. In conclusion, the insulating behavior of Mott insulator materials is explained in terms of the repulsive coulomb potential energy U, which induces the insulation when it is large enough, on the other hand if the band width or the transfer integral of the neighboring interacting atoms exceeds U value, then the transition from insulator to metal occurs. It is worth noting that, high-T_c superconductivity in cuprates is induced by doping the parent compound which is an antiferromagnetic Mott insulator state.

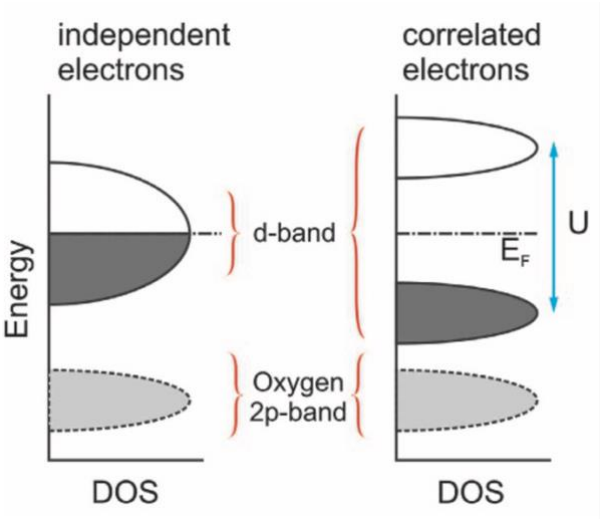

Figure 1. 1. A schematic representation shows the band diagram of non- correlated electrons and correlated electrons according to the band theory and Hubbard-Mott model respectively [6,7].

1.2. **Antiferromagnetism and magnetic materials**

Electrons are entities that carry spins, with each spin occupying a state oriented either up or down, adhering to the Pauli exclusion principle. In the absence of a magnetic field, the magnetic moment spins are arranged in a regular pattern, with an even number of spins oriented oppositely. Consequently, the net magnetic moment in typical antiferromagnetic materials is zero without an applied magnetic field. However, in the presence of an external magnetic field, these materials can exhibit a non-zero magnetic moment, especially at low temperatures due to

spin canting. Antiferromagnetic materials generally require very high magnetic fields to achieve saturation compared to ferrimagnetic or ferromagnetic materials. Some materials exhibit long-range antiferromagnetic order, while others do not. Antiferromagnetic materials are classified into various types, including A-type, C-type, and G-type antiferromagnets. They can be collinear or non-collinear (chiral) and can also be artificially created, such as synthetic antiferromagnets. The ordering and transition in antiferromagnetic materials is defined by the Néel temperature (T_N), which should follow the Curie-Weiss law (See Eq. 1.1). Interestingly, most of the Mott insulators are antiferromagnets.

(Eq. 1.1). $\boldsymbol{\chi_m} = \frac{\mathbf{C}}{\mathbf{T} + \mathbf{T_N}}$ (Curie- Weiss law for antiferromagnets),

such that T_N is the Néel temperature, χ_m is the magnetic susceptibility, C is curie constant and is material specific, T is the temperature.

The spin moments in ferromagnetic materials are arranged in parallel regular order of the same direction and magnitude as response to the applied magnetic field. The electrons in these materials always have a net magnetic moment value even in absence of the magnetic field, thereby have a stray field. The magnetic ordering is defined in terms of the Curie temperature (T_C) and in this case, it follows the Curie-Weiss law of the following form as in Eq.1.2. Fig. 1.2, and Fig 1.3 show a schematic representation of the electrons spin's arrangement as a response to the applied magnetic field in different magnetic materials.

(Eq. 1.2). $\boldsymbol{\chi_m} = \frac{\mathbf{C}}{\mathbf{T} - \mathbf{T_C}}$

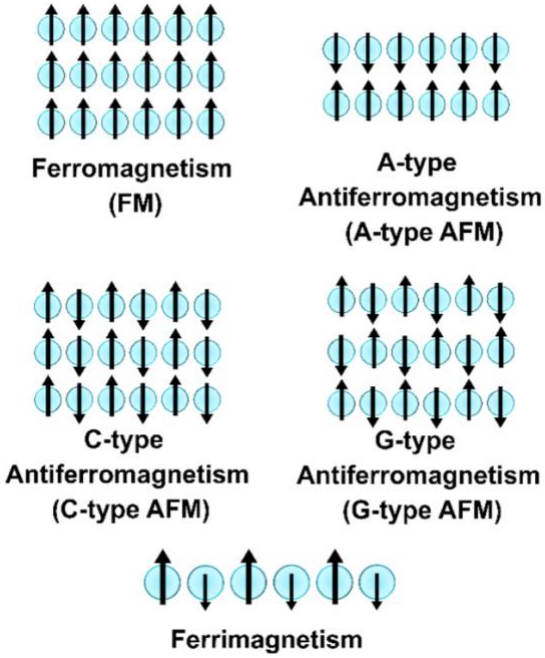

Figure 1. 2. A schematics of the electron's spins arrangement in presence of applied external magnetic field in different magnetic materials [8].

A common question in the condensed matter physics community, particularly in the context of this work, is why we selected antiferromagnetic candidates rather than ferromagnets. Antiferromagnetic materials are particularly advantageous due to their lack of stray fields, enabling higher data storage densities and faster speeds. This makes them ideal candidates for designing densely packed spintronic memory devices. Additionally, the high saturation field and zero net magnetization in the absence of an external field contribute to the fast and efficient switching in antiferromagnetic-based spintronic devices.

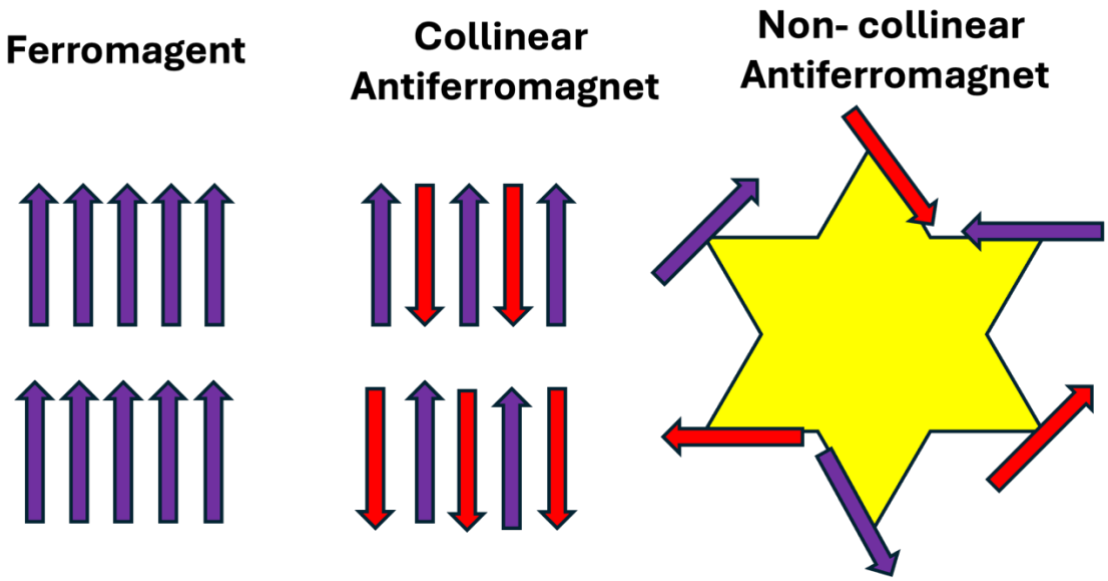

Figure 1. 3. Schematic representations of the spin arrangements in various kinds of magnetic materials; ferromagnets, antiferromagnets of both collinear and non-collinear structure.

1.3. **Anomalous Hall effect**

When a current passes through c conducting material in one direction (positive x-direction) and an external magnetic field is applied perpendicular in the upward z- direction, a transverse component of an electric field is created in the y- direction such as it is perpendicular to both magnetic field and current direction. This happens because of the charge accumulation at the conductor plate. This effect is well known as Hall effect, see Fig. 1.4.

The generated voltage (Hall voltage, V_H) is expressed as function of the magnetic field B, electrical current I and the carrier density n_e as well as the thickness of the conducting plate.

On the other hand, some of the materials have an intrinsic characteristic such as strong spin-orbit coupling which can lead to an internal magnetization even in the absence of magnetic field. These materials are mostly ferromagnetically ordered (sometimes it can be chiral Antiferromagnets) in which this effect is occurring and is called anomalous Hall effect (AHE).

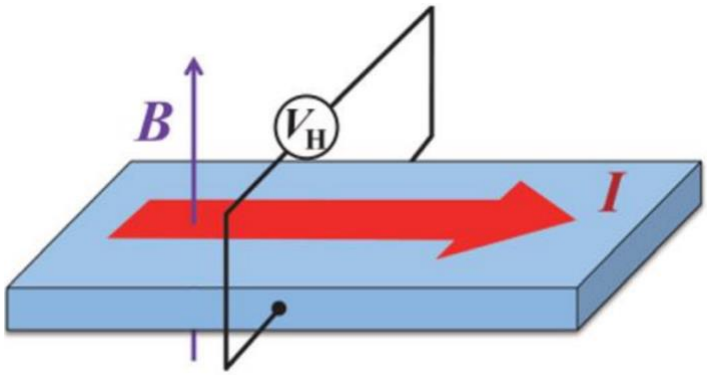

Figure 1. 4. Hall effect in conducting materials in presence of an external applied magnetic field [9].

The mechanism of this AHE is attributed to either intrinsic characteristics due to the presence of Berry curvatures or to extrinsic features such as skew- scattering of the spins due to magnetic impurities. AHE is used as evidence for the magnetic ordering in ferromagnetic materials and can be used as an indication of the chirality in the AFM compounds such as in some of the Mn_3X thin films. The measurement of transverse resistance in conducting materials can result in a linear curve as a function of the external applied magnetic field which implies the zero-resistance value at zero applied magnetic field, in this case the present voltage is the ordinary Hall voltage V_H as shown in the left panel of Fig. 1.5. However, if the transverse resistance in the Hall measurement shows a non-linear hysteretic loop behavior (squared shaped loop) as function of the applied field, this implies the non-zero value of transverse (Hall) resistance at zero Oe value of magnetic field (as shown in right panel in Fig.1.5). This means the existence of magnetization even in absence of any external magnetic field. This non-zero magnetization is due to the presence of an extra Hall voltage component in addition to the ordinary Hall voltage V_H, the extra transverse voltage is called the anomalous Hall voltage V_{AHE} and is proportional to the value of the internal magnetization due to the intrinsic properties of the conducting material.

The anomalous Hall resistivity ρ_{AHE} is proportional to the material's magnetization as the following:

(Eq. 1.3). $\rho_{AHE} = R_H.M.$ B, such that M, is the magnetization, and B is the external magnetic field, R_H is the Hall coefficient (depends on the carrier density and electric charge)

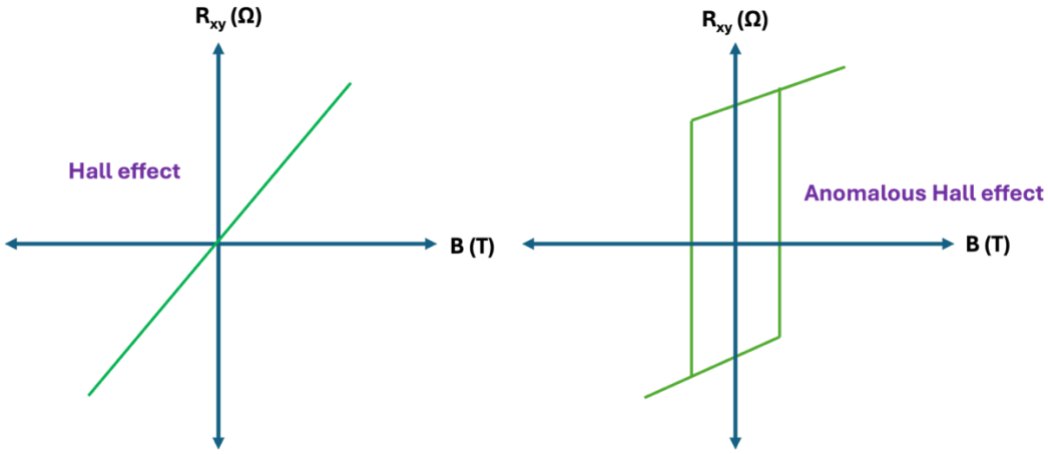

Figure 1. 5. Comparison between ordinary hall effect (OHE) and anomalous hall effect (AHE) in terms of the magnetic field dependence of the transverse hall resistance.

1.4. **Cooper pairs and conventional superconductivity**

Normally, electrons in a material are scattered by collisions with atoms, leading to thermal heating and a corresponding increase in electrical resistance, especially at higher temperatures. According to Coulomb's law, two electrons should repel each other due to their negative charges. However, this repulsion does not occur in superconducting materials. When a material becomes superconducting, its electrical resistance drastically decreases until it vanishes completely at a certain temperature. For many years, the mechanism behind this disappearance of electrical resistance remained a mystery.

Conventional superconductivity has been well explained by a microscopic theory formulated by Bardeen-Cooper-Schrieffer and is called (BCS) theory. BCS theory identified Cooper pairing as the key mechanism behind conventional superconductivity at low temperatures. A Cooper pair consists of two negatively charged electrons that pair up via an

interaction mediated by lattice vibrations, or phonons. This pairing occurs because the positive ionic cores of the lattice atoms, which vibrate due to electron scattering, create an attractive force between the electrons and the lattice ions, causing a local distortion in the lattice. This increased local positive charge can overcome the repulsive force between electrons, resulting in electron pairing at the long distances (See Fig. 1.6).

Similar pairing occurs for other electrons in different regions of the lattice, leading to the formation of multiple Cooper pairs. Once electrons form Cooper pairs, they no longer behave as fermions and do not follow the Pauli exclusion principle. This allows multiple Cooper pairs to occupy the same quantum state.

The energy required to form a Cooper pair is very small (around 10^{-3} eV), which explains why superconductivity in conventional superconductors occurs only at low temperatures (see Eq. 1.4). At higher temperatures, the increased thermal vibrations in the lattice generate thermal energy that can exceed the binding energy of Cooper pairs, breaking them apart and thus destroying the superconducting state.

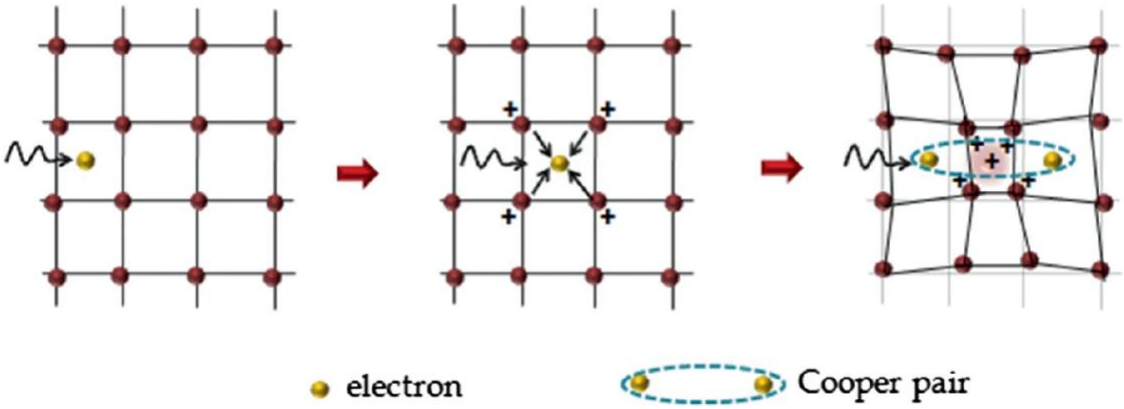

Figure 1. 6. A schematic representation of the Cooper pairing formation in conventional superconductors [10].

(Eq. 1.4). $K_B T_C = 1.134 E_D e^{\frac{-1}{N(0)V}}$,

Such that V is the electron-phonon coupling potential, E_D is the Debye cutoff energy, and K_B is the Boltzmann constant, N (0) is the density of states at Fermi level.

Finally, to claim that a material is superconducting it should show the following observations: (i) Vanishing of electrical resistance below certain transition temperature, (ii) expulsion of magnetic field; perfect diamagnetism and Meissner effect (iii) Cooper pairs formation (iv) long- range phase coherence (v) superconducting gap.

1.5. **Two-dimensional electron gas**

The emergence of a metallic layer through the growth of two adjacent insulating layers is a fascinating and exotic phenomenon observed at oxide interfaces in the last two decades [11]. Remarkably, when electrons in this conductive layer are confined to move within certain dimensions while remaining free to move in others, it results in two-dimensional conduction. This is the basis for the formation of two-dimensional electron gases (2DEGs). Fig 1.7 shows a schematic representation of the 2DEGs at oxide interfaces.

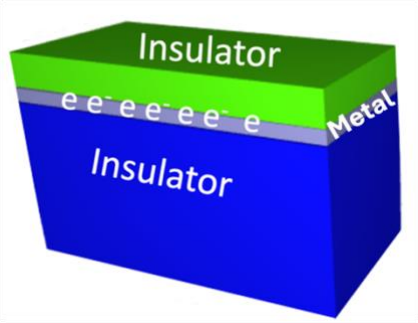

Figure 1. 7. A schematic sketch of the two-dimensional electron gas at insulating oxide interfaces.

In analogy to the 2DEGs in semiconductors, a high-electron mobility can be obtained in the 2DEGs formed at the insulating oxide interfaces. Interestingly in case of oxide 2DEGs the sheet carrier densities can reach high values up to 10^{14} cm^{-2} whereas the mobility can still be as high as 10^4 cm^2/ V.s. The first and most famous candidate of 2DEGs is found in $SrTiO_3$ /$LaAlO_3$ interfaces[11]. In the past decade, a new candidate for 2DEGs emerged with the use of $KTaO_3$ as the substrate. This is particularly intriguing due to the significant spin-orbit coupling provided by the tantalum (Ta) in $KTaO_3$. Notably, superconductivity has been

observed in 2DEGs formed in both $SrTiO_3$ and $KTaO_3$ systems, adding an exciting dimension to the study of these electronic systems [12-14]. Fig 1.8 elucidates the schematics of crystal structure at the interface of $SrTiO_3/LaAlO_3$ and illustrate the charge ordering as well as the layer termination as was reported by Ohtomo and Hwang[11].

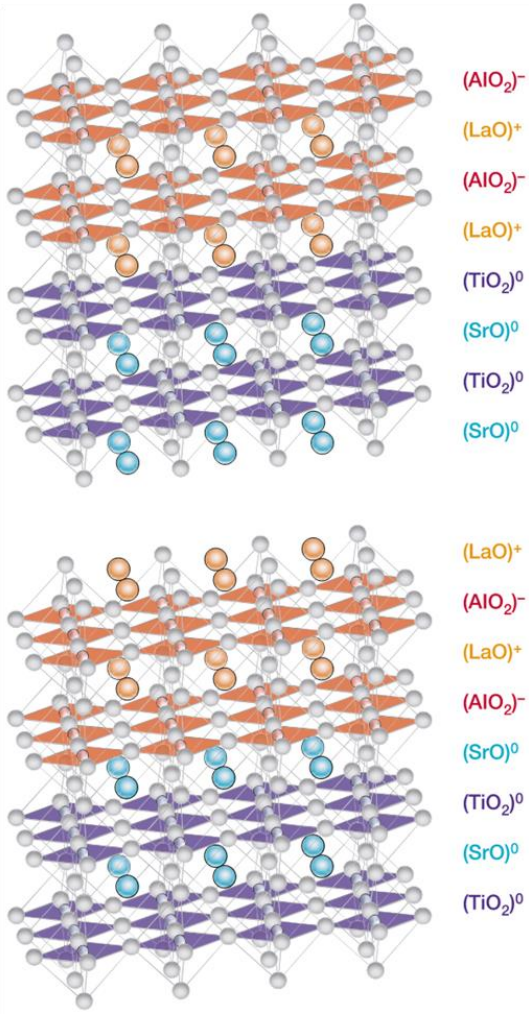

Figure 1. 8. The crystal structure of $SrTiO_3/LaAlO_3$ showing the ionic charge ordering in each adjacent layer at the interface [11].

To date, the formation of two-dimensional electron gases (2DEGs) at insulating oxide interfaces has been primarily attributed to surface reconstruction, polar catastrophe, charge state discontinuities, and ordering. Despite these insights, the mechanisms behind these 2DEGs remain an active area of research. Recently, it has been discovered that the surface of $SrTiO_3$

can generate 2DEGs without requiring an additional overlayer or interface. In these cases, the observed two-dimensional conduction is thought to be due to the formation of oxygen vacancies within the $SrTiO_3$ substrate.

1.6. **Disordered superconductivity**

Structural disorder and impurities or inhomogeneity in some candidates of superconductors can lead to peculiar properties which is not directly explained by the BCS theory. In other words, the pairing mechanism of Cooper pairs is different in these (disorder) superconductors. This category of superconductors exists mostly in the low-dimensional materials particularly thin films, and includes TiN, NbN or InO thin films. One of the peculiar characteristics of disorder superconductivity is the occurrence of pseudo gap, this indicates the formation of Cooper pairs above the superconducting transition temperature but without vanishing of the electrical resistance of the material. Additionally, if the disorder is very pronounced this might lead to an electronic changes and results in superconducting to insulating transition. Recently, in work reported by Bastiaans et al., using the scanning tunneling microscopy (STM) the direct evidence observation of Cooper pairing in disorder TiN thin films above the superconducting transition temperature (2.3 K) at temperatures up to 7.2 K as shown in Fig. 1.9. This observation was based on the measurement of effective charge of electrons below and above the superconducting transition temperature as well as by measuring the spectral gap at same temperatures.

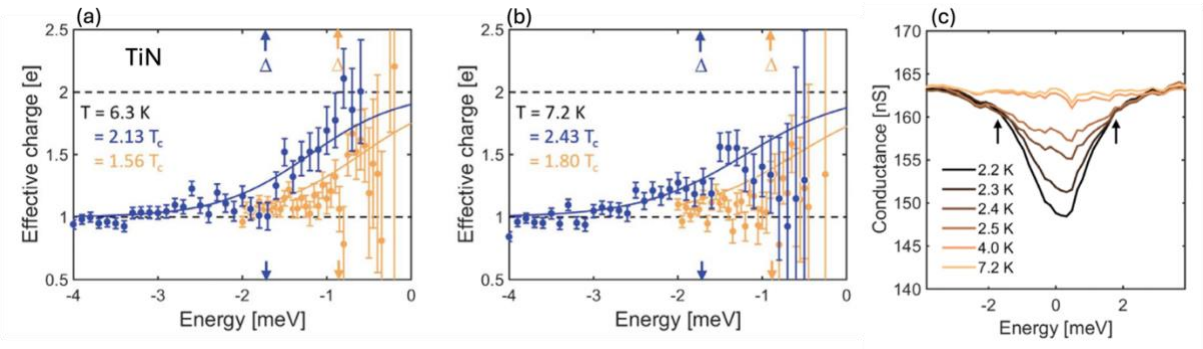

Figure 1. 9. Effective charge q*(V) of disorder superconducting TiN thin films grown by atomic layer deposition (blue) and by sputtering (orange) method measured at temperatures above the T_c (2.3 K) at (a) T= 6.3 K and (b) at T= 7.2 K. (c) Temperature dependence of the

spectral density gap measured by the differential tunneling conductance from 2.2 K to 7.2 K, credit to Bastiaans et al.,[15].

1.7. **Meissner effect**

The Meissner effect is a main feature of superconductors, it reflects the perfect diamagnetic behavior, and it is a tool that being used to distinguish the superconductivity from perfect conductors. Superconductivity does not mean only vanishing of electrical resistivity below the transition temperature, but also implies the expulsion of applied magnetic field due to the Cooper pair condensation. The magnetic susceptibility of perfect superconductors should reach a value of $\chi \approx -1$, which implies 100% of the superconducting volume fraction in the material, in other words this would reflect the homogenous superconductivity through all the volume of the material. The Meissner effect can be measured by performing magnetic field dependence of magnetization or magnetic susceptibility or temperature dependence of the magnetic susceptibility. However, each superconducting material can show the Meissner effect (perfect diamagnetism) up to certain value of the applied magnetic field, above this value the material can no longer expel the magnetic field and then it will allow the field to penetrate the superconducting state and become metallic. This value of magnetic field is called the critical field, and it has two values in the type II superconductors (lower H_{c1} and upper H_{c2} critical fields), see Fig.1.10.

The Meissner effect mechanism is explained using the London equations, particularly via the London penetration depth λ.

(Eq. 1.5). $\lambda = \sqrt{\frac{m}{n_s \mu_o e^2}}$

Such that m is the mass of electron, and e is the charge and μ_o is the free space permeability.

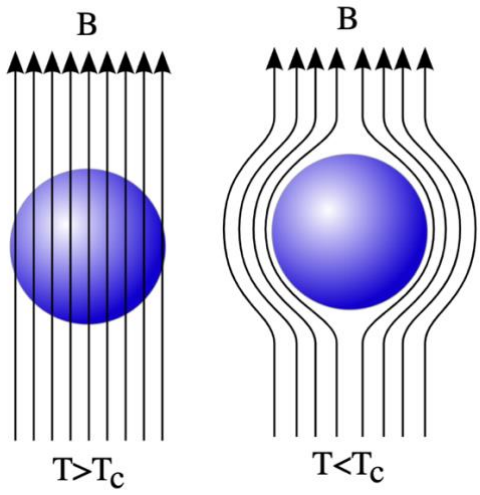

Figure 1. 10. The Meissner effect: magnetic field expulsion below superconducting transition T_c and penetration above T_c. Credit of image is to Wikipedia.com.

1.8. **Unconventional superconductivity**

The microscopic theory of superconductivity developed by Bardeen, Cooper, and Schrieffer (BCS) does not account for all classes of superconductors, particularly those discovered after its formulation. These superconductors are classified as unconventional or exotic. The most well-known examples include high-T_c cuprates superconductors, such as $YBa_2Cu_3O_{7-x}$, as well as materials like UTe2, where the superconducting pairing mechanism is triplet rather than singlet. In UTe_2, spin-triplet superconductivity is primarily observed in bulk crystals rather than thin films. Exotic superconductivity also encompasses two-dimensional superconductivity at the interfaces of insulating oxides, where two-dimensional electron gases (2DEGs) form, such as in $SrTiO_3/LaAlO_3$. In these systems, superconductivity can coexist with ferromagnetism, confined intriguingly to two dimensions. Fig.1.11 illustrates a schematic representation of two different mechanisms of superconducting pairing: spin-singlet and spin-triplet pairing. Those superconductors which does not obey the BCS theory are being partially explained by the Eliashberg theory of strong coupling, spin-fluctuations or still not explained at all, in both cases this still an ongoing work of active research. Fig. 1.12. shows the first observation of spin-triplet superconductivity in UTe_2 [16].

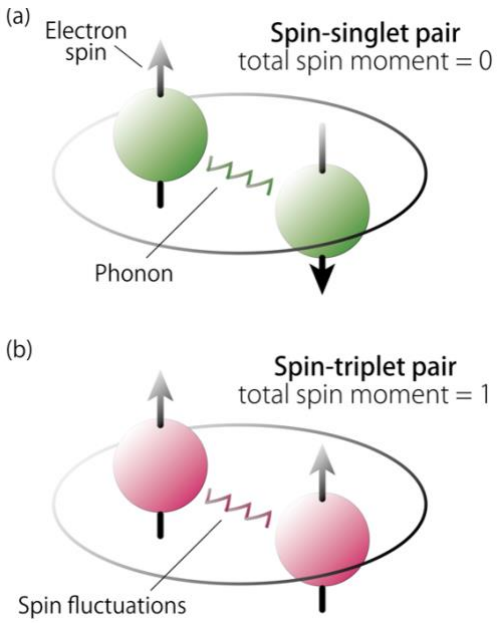

Figure 1.11. Two types of superconducting electron pairing, the first is spin-singlet (a) follows the BCS theory and, the second is spin-triplet (b) violates the BCS theory*[17,18]* .

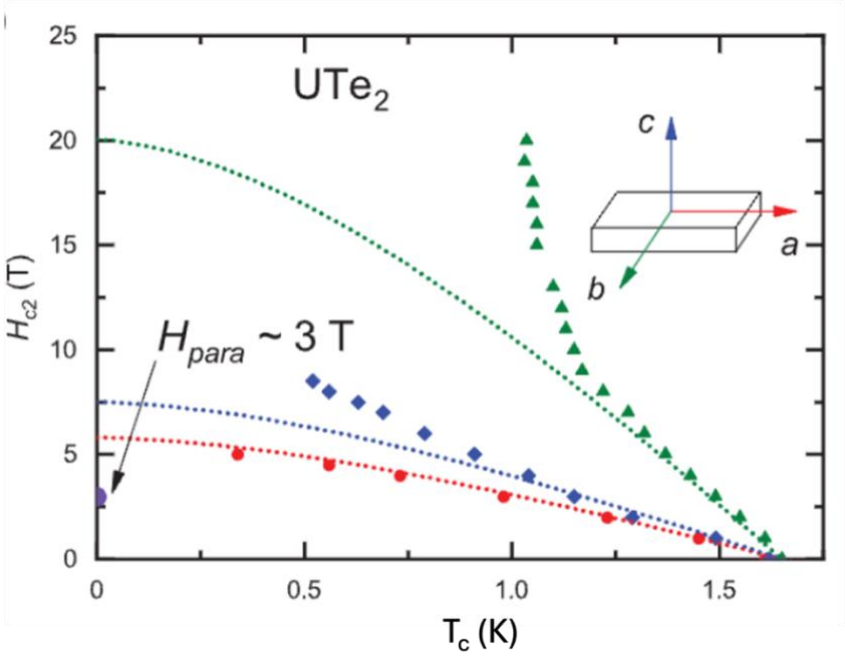

Figure 1. 12. The first observation of spin-triplet superconductor in UTe_2, the figure shoes the temperature dependence e of the upper critical field in three different directions with an anomaly in the b-direction [8].

1.9. **Why $LaTiO_3$**

This work primarily focuses on epitaxial heterointerfaces based on $LaTiO_3$. In its bulk form, $LaTiO_3$ is a Mott insulator with G-type antiferromagnetic ordering, exhibiting a Néel temperature in the range of 120 K to 146 K. The primary objective of this research is to explore novel interfacial superconducting candidates using the state-of- the art molecular beam epitaxy, with a particular emphasis on attempts towards achieving high-T_c or unconventional superconductivity in a new material system. It is well known that high-T_c superconductors typically emerge through the doping of a parent compound, which in the case of cuprates, is an antiferromagnetic Mott insulator of a bulk orthorhombic structure. Similarly in case of iron-based superconductors, the parent compound is antiferromagnetic. $LaTiO_3$ is also a bulk Mott insulator of an orthorhombic crystal structure, and it is a G-type antiferromagnet, which is very similar to the characteristics of the parent phase of cuprates oxide superconductors. This makes $LaTiO_3$ an ideal candidate for this exploration, and its selection is based on these motivating criteria as declared.

2. Experimental Methods

This chapter addresses the experimental facilities these have been used in this work, including sample growth, structural and surface characterization. Through it the main instrumentations relevant to this work and heavily used are highlighted.

2.1. **Molecular beam epitaxy**

Among the various physical deposition systems these operate in high or ultra-high vacuum environment, molecular beam epitaxy (MBE) has proven its effectiveness in producing high-quality (ultra) thin films for more than seven decades and continues to be in high demand. MBE allow the controlled growth of materials atom by atom. Originally, MBE was designed for the growth of materials used in semiconductor technology. The molecular beam epitaxy is equipped with several kinds of pumps such as turbo pumps, ion pump and cryopumps in addition to the pre-vacuum- roughing pumps for achieving the ultra-high vacuum. The working principle of molecular beam epitaxy relies on the Knudsen cell function which acts as a molecular beam accelerator by heating it in an ultra-high vacuum environment. The atoms of a specific element are ejected towards the substrate once it reaches the desired sublimation or melting temperature of the element. The materials of interest for deposition are toped up into crucibles made of specific materials whose melting point temperatures higher these that of the deposited elements to prevent the melting of crucible's material into the evaporated atoms. The formed gaseous beam of the sublimated atoms is then condensate on surface of the wafers and start to react with each other, in this case the mean free path of the atoms plays a role in preventing the interaction of these atoms with the carrier gases or with each other until they reach the substrate, this is very crucial for deposition quality.

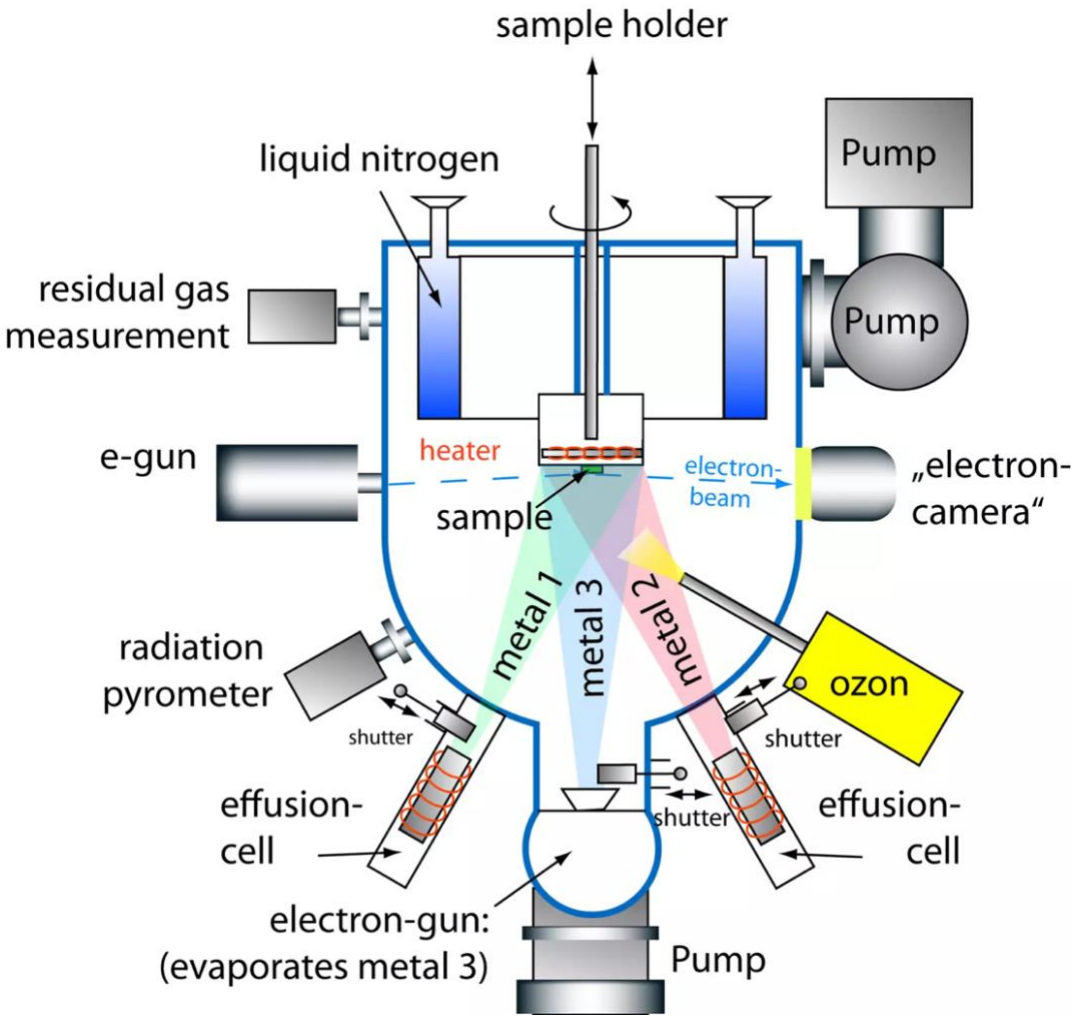

Figure 2. 1. Schematic diagram of Oxide Molecular Beam Epitaxy (MBE), courtesy of © Max Planck Institute for Solid State Research [19].

Certain materials, particularly perovskite oxides need elevated temperatures during the deposition to be formed in the proper structure, for this reason most of the MBE systems are equipped with a heater installed in the growth stage to provide the necessary temperatures into the wafers when is needed. In some of the MBE systems, the heaters are installed in a growth manipulator (rotating motor) to rotate the substrates or samples during or after the growth for several purposes which increases the possibility of getting homogenous and smooth surface of the grown films. A main advantage of the molecular beam epitaxy is the high quality of the grown films, which can be perfectly epitaxial, has very smooth surface of an excellent root

mean square roughness (RMS) value, uniform, crystalline and homogenous deposited films. The controlled deposition rate which can be tuned to be very low is one of the main factors in charge of the high-quality of the obtained films grown by the MBE. However, the low deposition rate may be considered as a double-edged sword as it will elongate the process of deposition duration as compared to other systems such as pulsed laser deposition (PLD) or sputtering. Nevertheless, the slow deposition rate can be increased or tuned based on the plans of the operating user of MBE, in general if the property that the researcher search for is not an interface effect, then the slow deposition rate will not play a significant role. This sheds the light on the main function of MBE, apart of the semiconductor technology, for nowadays, the interface- induced superconducting spintronics phenomena, the MBE is mainly used for the deposition of monolayers and films these can host interfacial induced phenomena. A schematic diagram representing the oxide-molecular beam epitaxy is shown in Fig. 2.1. The schematic of MBE shows the components of the system as indicated and labeled on the represented figure.

2.1.1. Knudsen cell (Effusion cell)

The Knudsen cell (K-cell), was developed by Martin Knudsen in the 1909 [20], it is also known as an effusion cell, is the primary functional component in molecular beam epitaxy (MBE) technology. The K-cell acts as an MBE furnace, heating the material until it evaporates. It consists of a crucible made from materials with high melting points, such as tantalum (Ta), pyrolytic boron nitride (PBN), or tungsten, and contains the material to be evaporated, in addition to a heating filament mostly made of Ta and water-cooling lines as well as a thermocouple. A schematic diagram shows the design of K-cell is depicted in Fig. 2.2. The K-cell allows for precise temperature control, which in turn controls the flux of the deposited material during growth. To prevent contamination or unwanted evaporation, the cell is equipped with a well-controlled shutter that is used during the ramping up of the cells to the desired deposition temperature. The beam flux density J of the evaporated material at a distance L from the source is analyzed by Knudsen and can be determined using the following equation, noting that r is the effusion aperture radius of the cell, p is the vapor pressure, M is the molecular weight of the material, and T is the temperature.

(Eq. 2.1). $J = 4.62 \times 10^{22} \mathbf{x} \frac{\mathbf{pr2}}{\mathbf{L^2 \sqrt{MT}}}$

A lot of progress has been achieved in the domain of effusion cells, one MBE can be equipped by a retractable sources or non-retractable source, usual source or cracker source for the group V elements. The advantage of the retractable source is one can retract the source to make maintenance of it to top up the materials when it is depleted without the need to vent the whole MBE system or growth chamber.

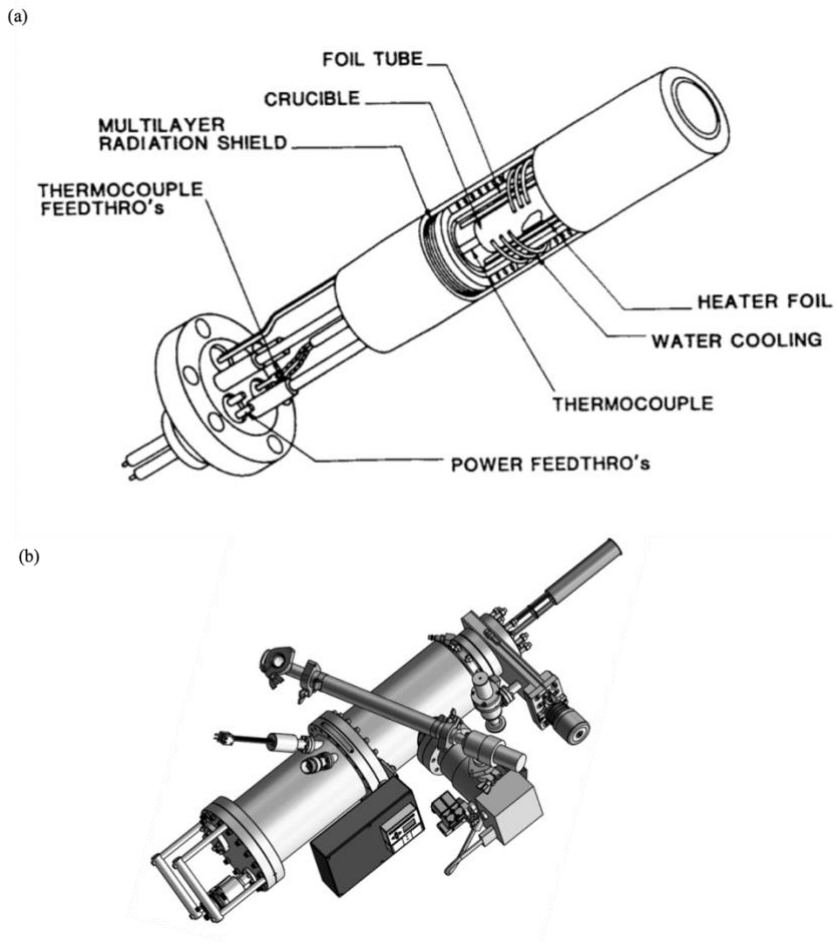

Figure 2. 2. Knudsen (effusion) cell used in molecular beam epitaxy to evaporate the material of interest; it can also be used to measure the vapor pressure (VG Semicon.). (b) A schematic of a retractable Knudsen cell (Veeco-GEN 10) used in the growth of films in this work.

2.1.2. Reflection high- energy electron diffraction (RHEED)

Reflection high-energy electron diffraction (RHEED) is a surface-sensitive imaging technique commonly used in molecular beam epitaxy (MBE) to analyze the structural

properties of crystalline thin films. RHEED operates by directing an electron beam at the surface atoms of the sample, where the interaction causes the atoms to scatter, forming a diffraction pattern. This pattern provides information about the crystallinity, surface smoothness, and structural symmetry of the grown material. A simple schematic of the RHEED setup is shown in Fig. 2.3.

RHEED's CCD camera captures multiple diffraction patterns, each corresponding to different surface features, which may include spots, streaks, modulated streaks, inclined streaks, or transmission spots, as illustrated in Fig. 2.4. In this study, a RHEED pattern of a sample grown using the Veeco oxide-MBE GEN10 system is shown in Fig. 2.5. The streak pattern observed here confirms the epitaxial growth of $LaTiO_3$ film on a $DyScO_3$ (110) single crystal substrate.

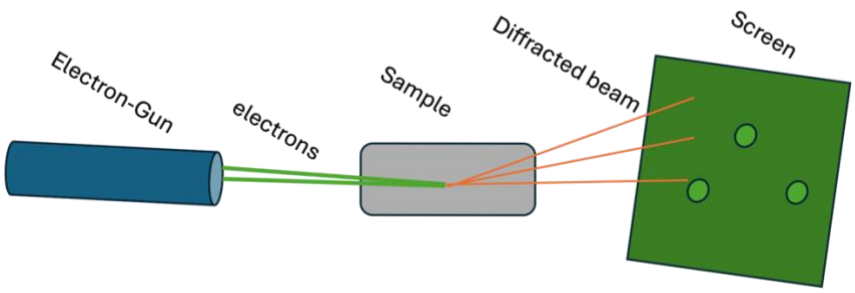

Figure 2. 3. Schematic representation of the reflection high-energy electron diffraction system.

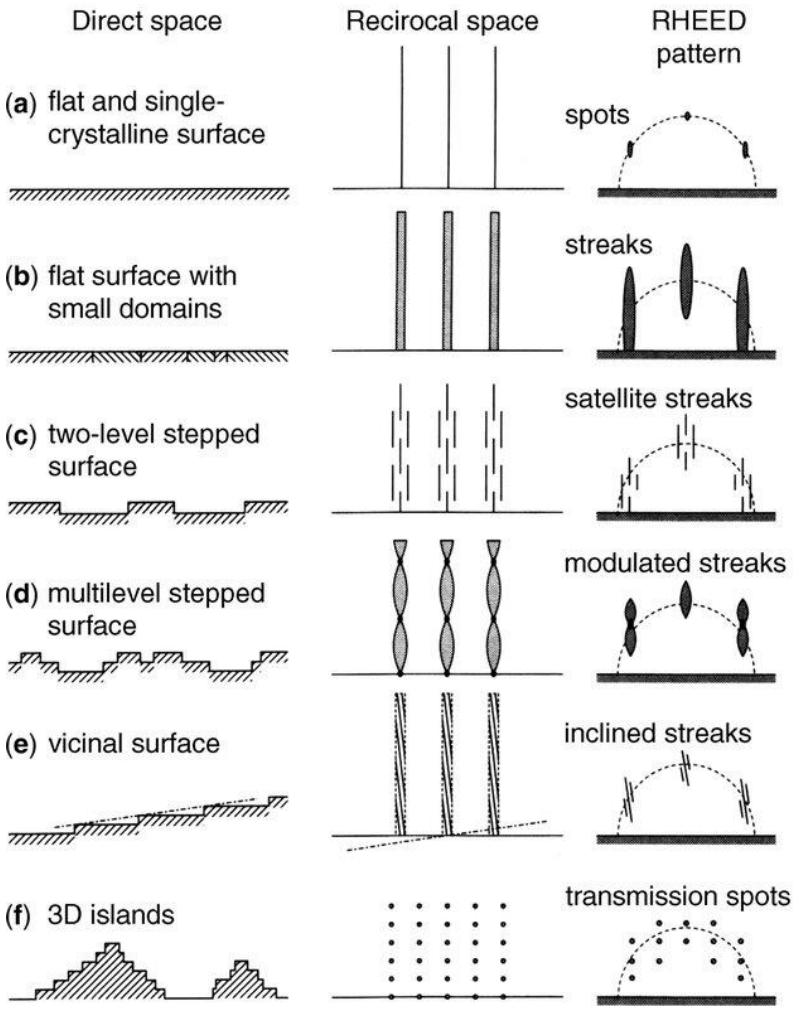

Figure 2. 4. RHEED patterns of various surfaces show the evolution of epitaxial flat surfaces, crystalline or 3-dimensional islands growth (Courtesy by Yoshimi Horio).

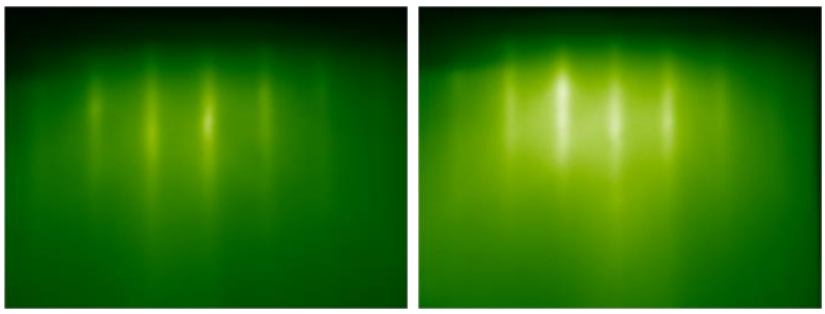

Figure 2. 5. RHEED image taken by KSA 400- RHEED CCD camera equipped into Veeco GEN 10 MBE system, shows streaks pattern of the grown $DyScO_3$ (110) /$LaTiO_3$ film.

2.1.3. Types (modes) of MBE- growth

In molecular beam epitaxy, growth can be precisely controlled to produce high-quality thin films with smooth surfaces and uniform epitaxial deposition. However, this level of quality is not guaranteed in all cases, as the outcome depends on the specific growth method used. Various growth techniques within MBE are available for thin film deposition, each affecting the results differently. Below we are addressing the various methods of the growth:

(a) Layer-by-layer (Frank-Van-der Merwe) growth

This method requires the substrate and deposited material to have matching lattice constants. Additionally, the substrate surface must be exceptionally clean and, ideally, exhibit a step-terraced structure. Achieving layer-by-layer growth also necessitates a low deposition rate during material growth, allowing the deposited atomic beam to adsorb uniformly across the substrate surface. This controlled deposition enables the material to diffuse and form a complete monolayer on the substrate before the next layer is deposited. The deposited materials form a homogenous film on the surface of substrate.

(b) Islands (Volmer- Weber) growth

In this method, atoms form isolated three-dimensional islands rather than stacking uniformly on the substrate surface. This typically occurs when there is a significant lattice mismatch between the substrate and the deposited material. In such cases, the deposited atoms (adatoms) tend to bond more strongly with each other than with the substrate surface, or the deposited material has a lower surface energy, leading to island formation.

(c) Layer + island growth (Stranski–Krastanov (SK))

In certain cases, the evaporated beam creates a hybrid growth pattern on the substrate surface, combining both layer and island growth. Initially, a two-dimensional layer forms on the substrate, followed by the development of isolated three-dimensional islands. This hybrid growth occurs when there is lattice mismatch; as the deposited monolayers reach a certain thickness, strain accumulates and can no longer be accommodated, leading to the transition from layer to island growth after a few monolayers.

(d) Step flow growth

In some cases, to achieve specific functional properties, the substrate is deliberately misaligned to direct the flow of evaporated adatoms in a particular direction during growth, promoting a step-like pattern. Under these conditions, adatoms follow a continuous layer growth across the substrate surface. This method requires a very high substrate temperature and a very low deposition rate.

(e) Hybrid (combined) growth

In some cases, growth parameters can be adjusted to incorporate multiple growth modes simultaneously. This approach is used to tailor specific properties of heterostructures. Achieving this hybrid mode involves manipulating the substrate temperature—raising or lowering it as needed—and/or adjusting the deposition rate accordingly.

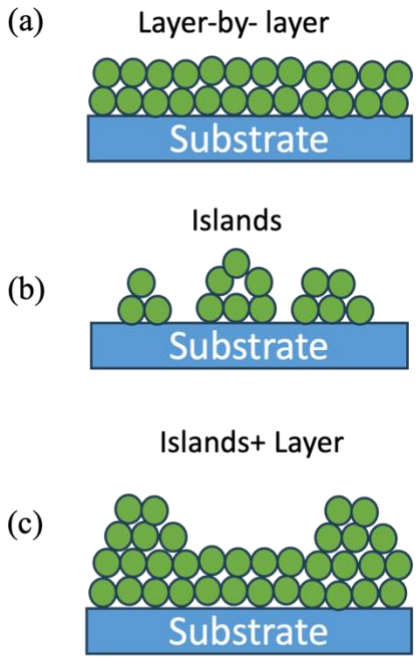

Figure 2. 6. Schematics of examples of the growth modes in molecular beam epitaxy (a) layer-by -layer 2-dimensional growth, (b) Islands (3D) growth, (c) Island+ layer growth.

A schematic representation of possible growth modes implemented in MBE growths is displayed in Fig. 2.6 (a, b, c) for the layer-by- layer, islands and layer combined with islands growth modes, respectively.

2.1.4. Ozone generation

In this study, oxide material growth via molecular beam epitaxy (MBE) is enhanced by introducing ozone gas as an oxidizing agent to supply oxygen during metal oxide deposition. The use of ozone supports precise stoichiometry control in complex oxide growth and ensures high film quality, which is essential for achieving functional interfaces. Ozone is generated by an advanced ozone generator system equipped with a compressor and heater, cooled by liquid nitrogen. This generator converts oxygen (O_2) into high-purity ozone (O_3) before introduction into the MBE growth chamber. A schematic diagram of the generation process is shown in Fig. 2.7.

The generator produces ozone at 99.99% purity by mixing oxygen and nitrogen gases in a 99.8% O_2 to 0.1-0.2% N_2 ratio, with purity calibrated before injection. Injection amount is precisely regulated using a linear leak valve and an ozone ring injector, which control both the positioning and volume of ozone introduced. A pressure controller continuously monitors the ozone flow just before it enters the growth chamber, ensuring stable and controlled conditions for oxide deposition.

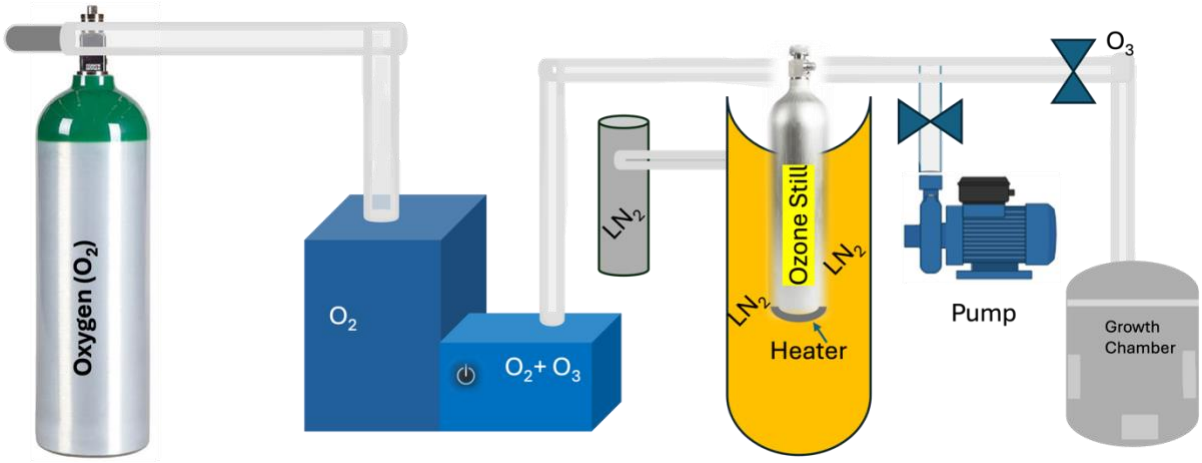

Figure 2. 7. Schematic representation diagram of Ozone generation process

2.1.5. Electron- beam evaporation

For the deposition of heavy metals, the needed power to sublimate or evaporate the atoms is very high which cannot be achieved using molecular beam epitaxy. Thereby, most of the molecular beam epitaxy are equipped with an electron beam evaporation system to deposit heavy metals. Electron beam evaporation is also a physical vapor deposition method which is operated in a high vacuum environment, however the growth rate in this method is relatively high which is good for the deposition of very thick films, on the other hand it does not achieve high quality as MBE growth. The working principle of E-beam is based on the sublimation of the anode (targe material) into gaseous phase via an electron beam ejected from the tungsten filament. The direction of the electron beam path is controlled and directed using a magnetic field, Fig. 2.8 shows schematic representation of the electron beam evaporation, its components

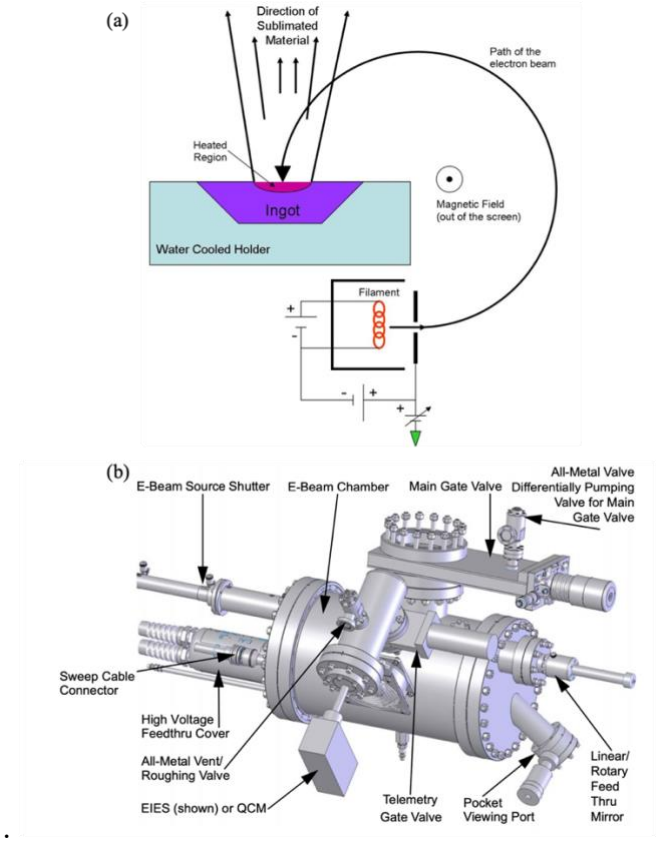

Figure 2. 8. Schematic representation of the electron beam evaporation method (a) (schematic, courtesy by wikipedia.com), (b) schematic of the Telemark type E-beam used in this study.

The molecular beam epitaxy (MBE) system used for growing all the films and samples in this work, shown in Fig. 2.9, is a GEN 10 dual chamber MBE system manufactured by Veeco. This system features a cluster module that links two MBE growth chambers through an intermediate storage chamber. One chamber is specifically designed for the growth of oxide materials, while the other is dedicated to nitride material growth. The base pressure is $5x10^{-10}$ Torr for the oxide-MBE system and $2x10^{-11}$ Torr for the nitride-MBE system. The oxide-MBE system is equipped with an ozone generator that supplies the pure ozone necessary for growing oxide thin films.

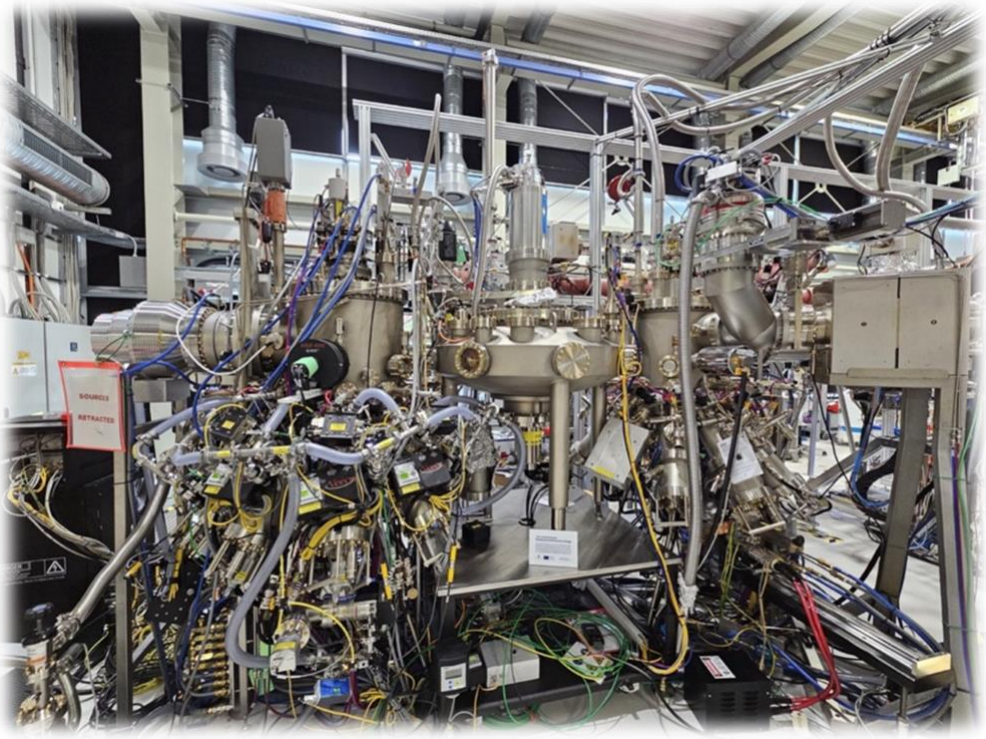

Figure 2. 9. Veeco molecular beam epitaxy system (Veeco GEN10- MBE) at Max- Planck institute of microstructure physics, at nano-systems from ions, spins and electrons (NISE) laboratory where all samples of this work were grown. The cluster module is consisted of dual chambers one (on the left hand side) is dedicated to growth of oxide materials and the other (on the right-hand side) is dedicated for the growth of nitrides materials, the oxide-MBE is

equipped with 11 turbo pumps in addition to an ion pump and a Ti-sublimation pump to maintain the necessary UHV environment in the oxide-MBE system which is equipped by an ozone generator.

2.1.6. Flux calibration

In molecular beam epitaxy (MBE) depositions, it is essential to have preliminary information about the flux of evaporated materials from either effusion cells or e-beam sources. This information significantly saves time on one of the most sophisticated and inherently slow deposition techniques. Estimating the flux rate is crucial for achieving the desired stoichiometry in grown films, whether they are binary, ternary, or doped ternary compounds. It also allows for an approximate determination of the growth rate, and thus the thickness, of the deposited layers. In MBE, flux estimation can be achieved using either a quartz crystal microbalance monitor (QCM) or a beam flux monitor (BFM). While neither method provides highly precise flux measurements, they are valuable for optimizing the stoichiometric balance of elements and for giving preliminary insights into the thickness and growth rate.

2.1.6.1. Quartz crystal microbalance monitor (QCM)

The QCM (Quartz Crystal Microbalance) consists of three main parts. The first part is the quartz crystal sensor, which is a thin circular crystal coated with a layer of gold or silver on both sides, allowing an alternating electric field to be applied across it. The second part is the oscillating circuit, which includes an oscillator that maintains the crystal's oscillation at its natural frequency, and a frequency counter that measures this oscillation frequency.

The QCM operates based on the principle of piezoelectric resonance. When an alternating electric field is applied across the two electrodes of the quartz crystal, it oscillates at its natural resonance frequency. When material is deposited on the crystal's electrode surface, the added mass causes a change in the oscillation frequency. This frequency shift enables precise measurements of the deposited material's thickness and the deposition rate.

So, the main key point is that the change in the frequency is converted to the change of the mass and accordingly results in the measurement of the deposition rate and thickness according to the following equation.

$\mathbf{\Delta f = \frac{2\Delta m f_o^2}{A\sqrt{P\mu}}}$. Such that, Δf is the frequency change, Δm is the mass change, f_o is the fundamental frequency of the crystal, A is the area of the crystal, ρ is the density of quartz, and μ is the shear modulus of quartz.

2.2. X- ray photoelectron spectroscopy

X-ray photoelectron spectroscopy (XPS) is a surface sensitive technique in the range of 1-5 nm which operates in ultra-high vacuum environment and is mostly used for the chemical composition analysis (a schematic of XPS is shown in Fig. 2.10). XPS is mainly based on the photoelectric effect, in which the electron's on a metal surface can be ejected if the energy of incident radiation on the surface is larger than the binding energy of the electron to the surface. The incident radiation interacts with the surface layers of the specimen of interest, every element has a characteristic peak at certain kinetic energy and intensity. The recorded energy peak position and the intensity due to the interaction between the incident radiation beam and the element in the specimen are used in the identification and quantitative analysis of the chemical composition. The emitted electron's energy versus the intensity is known as XPS spectra. It can be used to uncover the electronic and valence/oxidation states of the elements. XPS is very essential method in the optimization process of the growth of materials y molecular beam epitaxy. The physical principle depends on photoelectric effect as, since the incident x-ray has a known energy, and the kinetic energy of emitted electron is known which is measured by the detector, then the only unknown is the binding energy of the emitted electron. The binding energy of the emitted electron can be determined from the photoelectric effect equation as the following.

(Eq. 2.2) $E_{binding} = E_{Xray} - (E_{Kinetic} + \boldsymbol{\phi_o})$, whereas $\boldsymbol{\phi_o}$ is the work function of the material.

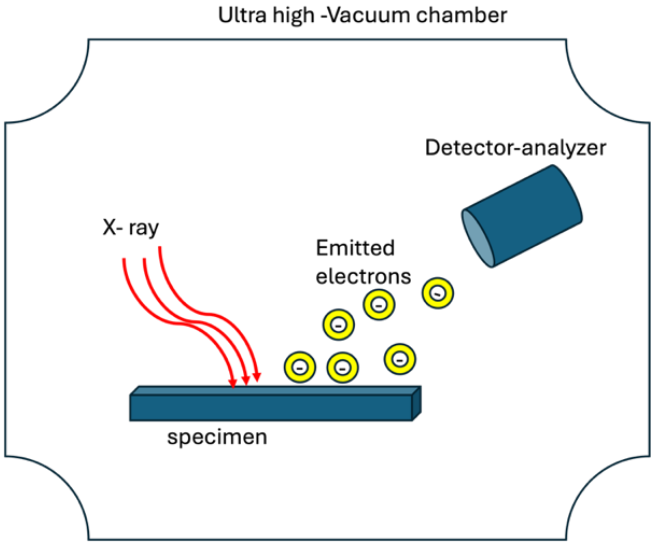

Figure 2. 10. Schematic representation of the x-ray photoemission spectroscopy technique (XPS).

2.3. X- ray diffraction

X-ray diffraction (XRD) technique is a method used to identify the phases of any material based on its diffraction pattern. It can be used to identify the phase of single crystal or thin films or powder materials and inspect if it is pure single phase or has multiple phases that can be quantitively estimated using the Rietveld refinement method. In thin films, XRD can tell us the information either it is epitaxial or not via performing φ- scans measurement and reciprocal space mapping measurement (RSM) relative to certain reflection peak. The thickness of thin films also can be measured using X-ray reflection method (XRR) via performing $2\boldsymbol{\theta} - \boldsymbol{\omega}$ scan at defined angle from the surface of the sample. The in-plane and out of plane lattice parameters can be accurately estimated using high resolution XRD and RSM scans. This provides a careful method of defining the crystal structure and the present strains in the grown heterostructure films. The XRD instrument is mainly consisted of an x-ray source (Cu, Be) to provide x-rays beam of certain wavelength, in addition to sample and sample holder and finally is the x-ray diffraction detector. The produced x-rays hit the sample surface with an incident angle, the x rays are diffracted by the sample phase and then reflected at similar angle towards the detector. By moving the sample and the detector this will changes the diffracted

angle; between the incident and diffracted beam (2θ) and the intensity of the diffracted beam is measured then the diffraction data can be recorded. The diffraction data are then used to give the diffraction pattern of the sample phases which is showing the diffraction angle 2θ versus intensity chart, which can be then compared to the x-ray diffraction patterns database to identify the phase of the sample. The physical principle behind the x-ray diffraction is based on the Bragg's diffraction law.

(Eq. 2.3) $n\lambda = 2d\sin(\boldsymbol{\theta})$, such that θ is the angle between the incident and diffracted x-ray beam at the sample's surface, λ is the wavelength of the x-ray beam, and d is the interlayer spacing distance between atoms. A schematic representation of the Bragg law is shown in Fig. 2.11.

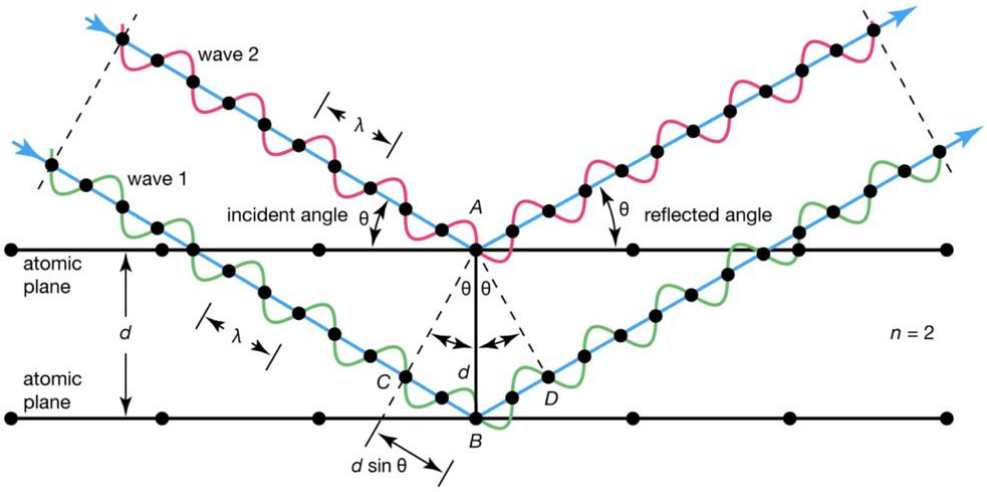

Figure 2. 11. Schematic representation of the Bragg's law of diffraction (courtesy by Britannica, inc.).

2.4. **Atomic force microscopy**

Atomic force microscopy (AFM) is a surface imaging technique used to scan the topography of thin film samples, providing information about the smoothness, homogeneity, and roughness of the grown sample. The AFM consists of a cantilever with a sharp silicon tip at its end, which acts as a probe. The cantilever is oscillated at a certain frequency by a

piezoelectric material. The system also includes a laser source, an XYZ drive and stage to move the sample and cantilever, and a detector to measure the deflection and motion of the cantilever. AFM can operate in several imaging modes, including contact mode, tapping mode, and non-contact mode. The principle of AFM operation is based on the interaction between the tip and the sample surface. The tip, with a nanometer-scale radius of curvature, generates mechanical or piezoelectric forces when it is near the sample surface, causing the cantilever to deflect. This deflection or feedback signal is measured by the AFM detector, depending on the imaging mode, either in constant force mode or constant height mode.

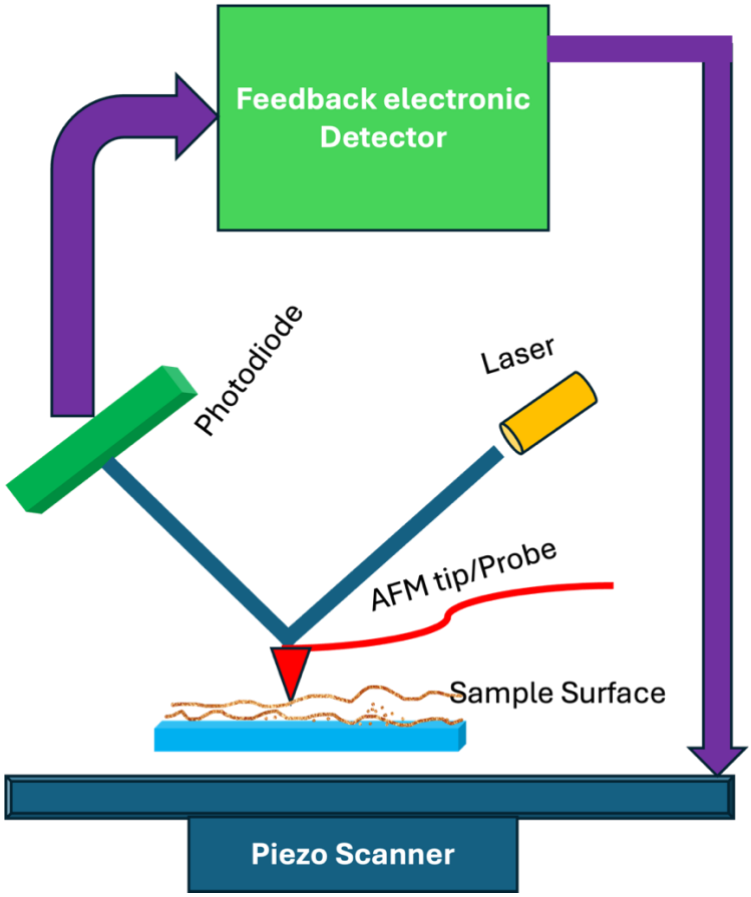

Figure. 2. 12. Schematic of the AFM in the contact imaging mode.

A schematic representation of the AFM is shown in Fig. 2.12. A real exemplary of the topography measurements were performed in this work on an MBE- grown samples of MgO (100)/ Fe_3O_4 (56 nm) and MgO (100)/ Fe_3O_4 (36 nm) samples using Bruker- AFM instrument

is shown in Fig. 2.13, it shows occurrence of step terraced surface which reflects the surface smoothness and high-quality of the grown films.

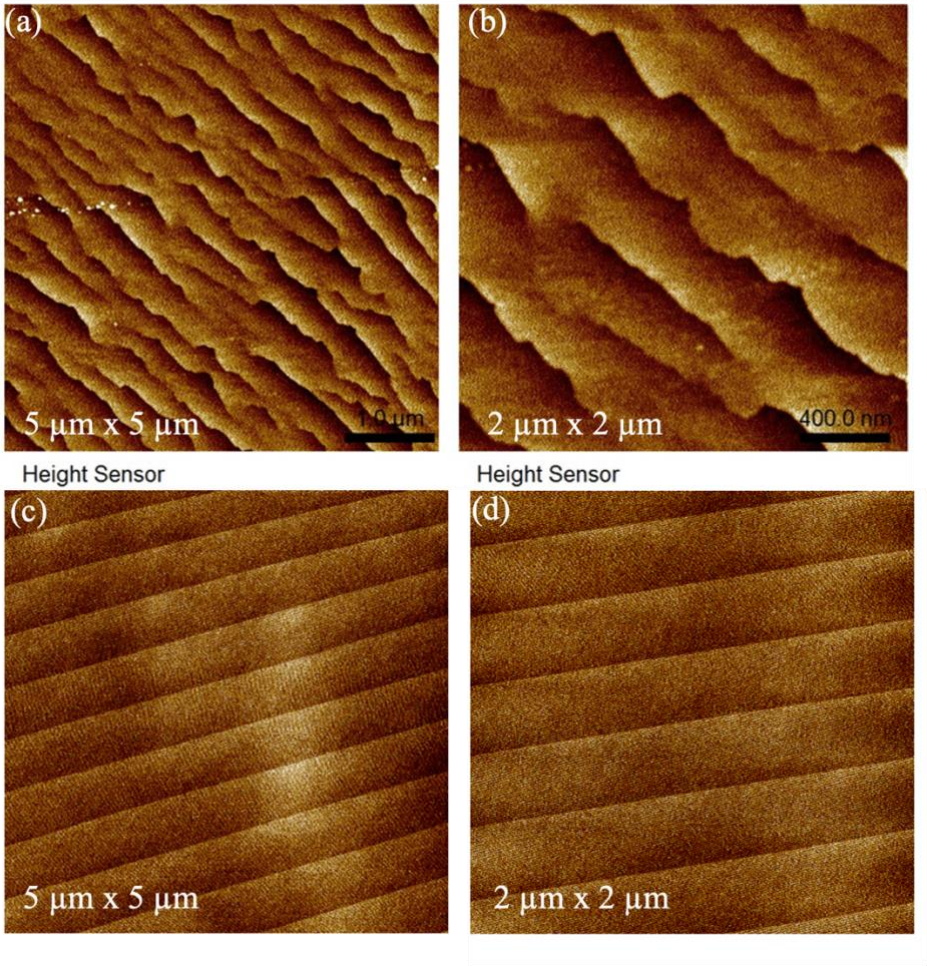

Figure 2. 13. Example of topography scan obtained by performing atomic force microscopy of: (a, b) MgO (100)/ Fe_3O_4 (56 nm) sample at scans area of 5µm x 5µm and 2µm x 2µm, respectively. (c, d) MgO (100)/ Fe_3O_4 (36 nm) sample at scans area of 5µm x 5µm and 2µm x 2µm, respectively; these two samples were grown by oxide- MBE as performed during the work of this thesis.

2.5. **Physical property measurement system**

Physical property measurement system (PPMS) is a low temperature technique which is mainly used for automated electrical transport measurements with/without an applied magnetic

field. The PPMS is equipped with a superconducting magnet (9-14 Tesla) and is consisted of heater, dewar and vacuum chamber, cryogenic free system supplied by a liquified helium thermocouple, sample puck to hold the sample and connections pins at the bottom of the dewar as well as mechanical linear motor and rotator at the top of the dewar and power supply. Additionally, the PPMS is provided with Keithley current sources and nanovoltmeters for DC measurements as well as lock-in amplifier for the necessary AC measurements. The system is pumped using scroll and turbo pump during the measurement. The measurements are automated with the help of PPMS interface software or Python or LabVIEW software codes. The magnetic field and temperature (1.6 K to 400 K) are full controlled and adjusted via the software interface. PPMS can be used for the electrical resistivity as function of temperature and field, heat capacity and AC and DC susceptibility measurements down to temperature of 1.6 K and up to magnetic fields of 14 T. The design scheme of PPMS instrument is shown in Fig. 2.14 which depicts the structure and components of PPMS. An exemplary measurement performed by using PPMS (Dynacol system) is shown in Fig. 2.15, showing the resistivity versus temperature measurement of MgO (100)/ Fe_3O_4 (56 nm) grown by Veeco-MBE system, in which the sample shows the metal to insulator transition as function of temperature which is atypical characteristic of the Verwey transition in magnetite.

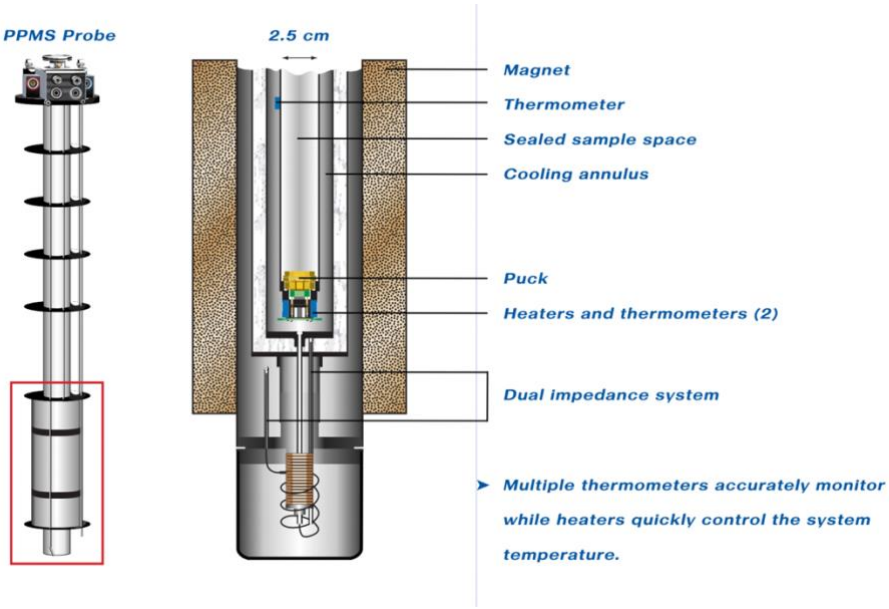

Figure. 2. 14. Schematic representation of the PPMS design (courtesy by Quantum Design).

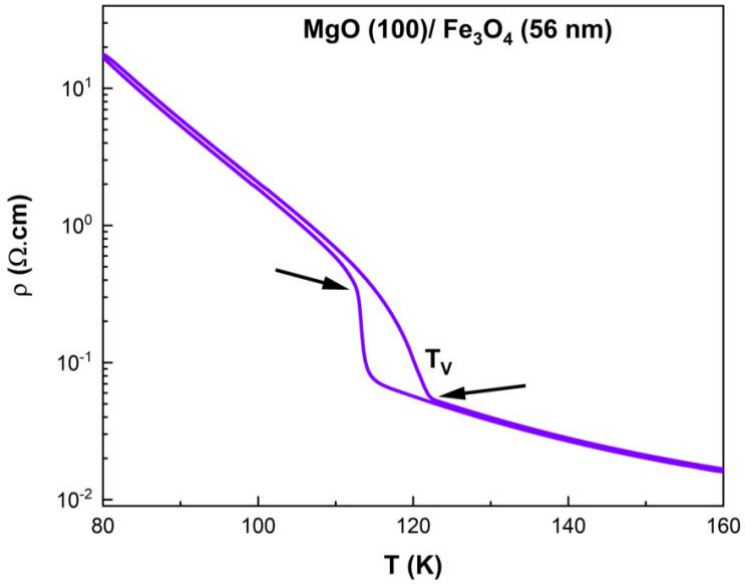

Figure. 2. 15. An exemplary result from this work obtained by using PPMS, shows the temperature dependence of electrical resistivity measurement of MgO (100)/ Fe_3O_4 (56 nm) sample grown by Veeco GEN10 oxide- MBE as part of results obtained in this work.

2.6. **Superconducting quantum interference device- VSM**

The superconducting quantum interference device- vibrating sample magnetometer (SQUID-VSM) is consisted of two superconductors separated by a thin insulating layer making two parallel Josephson junctions. This can be utilized to work as a magnetometer due to the extreme sensitivity of SQUIDs of measuring the magnetic flux that can be detected using the two Josephson junctions. The change of magnetic flux is usually measured via moving the sample via mechanical linear motors through the pick-up coils of the superconducting magnet. The flux change measured of the SQUID is converted into voltage which can be used to estimate the magnetic moment values.

(Eq. 2.4) $\Phi = \int \mathbf{B} \,.\, \mathbf{dA}$, where A is the area of the SQUID loop

The pick-up coil works as a second order gradiometer. The sample is positioned at position x which is parallel to the external applied magnetic field B_x. The voltage can be plotted versus the position, the magnetic moment value of each voltage is then plotted versus magnetic field to record the hysteresis loop of the measured sample. The SQUID-VSM can be used to determine the magnetic properties of thin films, powder or single crystals via measuring the magnetic field dependence of magnetic moment M (H) loops or temperature dependence of magnetic moment M (T) and AC susceptibility or Meissner effect in case of superconducting samples. The sketch in Fig. 2.16 illustrates the representation of SQUID-VSM system [21]. An exemplary figure of a measurement performed in this work by using SQUID-VSM MPMS3 system is shown in Fig. 2.17, in which the magnetic field and temperature dependence of magnetic moment are displayed.

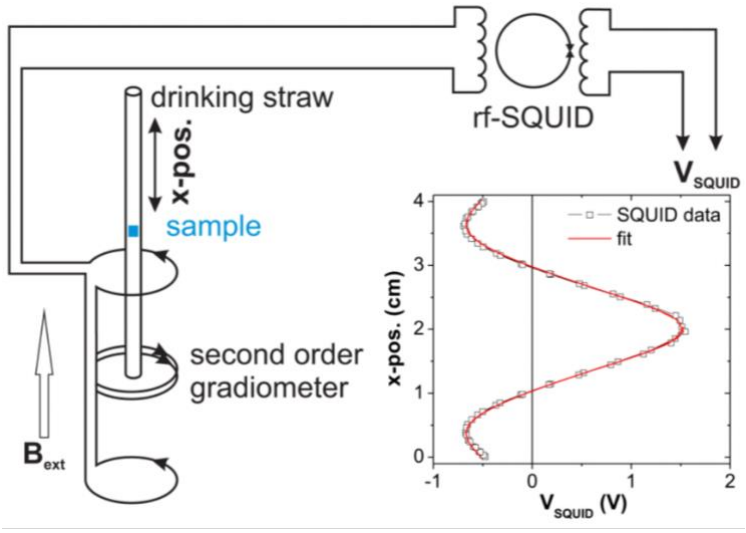

Figure. 2. 16. Sketch of the superconducting quantum interference device (SQUID) [21].

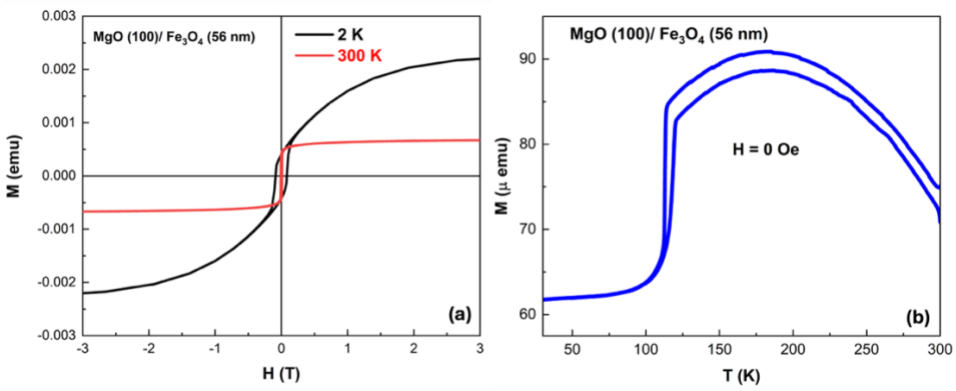

Figure. 2. 17. Exemplary result from this work shows the magnetic field and temperature dependence of magnetic moment measurement performed by SQUID-VSM MPMS3 magnetometer on MgO (100)/Fe_3O_4 (56 nm) sample grown by Veeco- GEN 10, MBE. The magnetic moment from the paramagnetic and diamagnetic contribution from the MgO substrate is not subtracted.

2.7. **X-ray magnetic circular dichroism**

X-ray magnetic circular dichroism (XMCD) is an element-specific technique used to examine the magnetism in magnetic (ferro/ferri) materials, including thin films, and two-dimensional materials [22]. XMCD primarily relies on the x-ray absorption spectra (XAS) of

two circularly polarized lights. The first XAS spectrum is obtained using left circularly polarized light, and the second with right circularly polarized light. The difference between these circularly polarized XAS spectra is used to calculate the XMCD spectrum of any magnetic material. The spin and orbital magnetic moments can be estimated from the highly sensitive XMCD spectra based on the line intensity and selection rules. XMCD can be performed with either in-plane or out-of-plane magnetic field configurations, under various applied magnetic fields, to provide comprehensive information about the sample's magnetization. Both XAS and XMCD spectra are measured at specific edges of the magnetic atom, resulting in a plot of photon energy versus intensity. XMCD can also generate a magnetic hysteresis loop of samples at different temperatures, similar to SQUID measurements. However, unlike SQUID, XMCD is an element-specific technique that depends on the magnetic atom itself. Fig. 2.18 depicts a schematic of the XMCD setup [23].

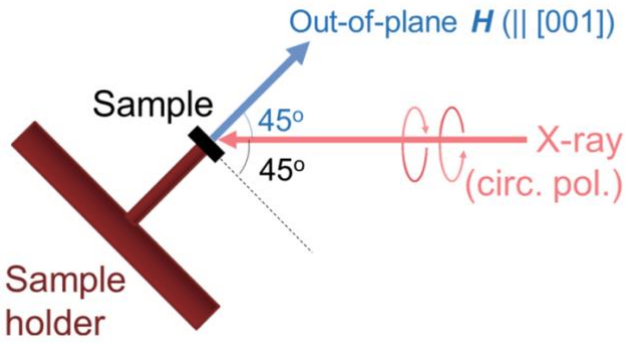

Figure. 2. 18. A schematic representation shows the experimental setup of x-ray magnetic circular dichroism system [23].

2.8. **Summary**

This chapter provided a detailed explanation of the working principles behind the experimental methods, techniques, and instruments utilized during this work in a brief way. For each piece of equipment or instrument described, an example of an experimental result obtained during this work is included to offer a practical illustration of the real outcomes generated using the respective instrument throughout this thesis.

3. Two -dimensional electron gases

Atomic sharp interfaces of two distinct materials represent a vital platform for hosting exotic physical phenomena. This includes two-dimensional electron gases (2DEGs), quantum and spin Hall effects or Berry phase curvatures, moreover the superconductivity which play crucial role in superconducting spintronics devices. This chapter delves into the detailed characterization of epitaxially grown perovskite thin-film interfaces, with a particular focus on inspecting the formation 2DEGs) at these interfaces, via the transport measurements. Our study primarily centers on the $LaTiO_3$ oxide, which was grown on various non-magnetic insulating single-crystal substrates, including $SrTiO_3$, $LaAlO_3$, $KTaO_3$, and MgO. We observed the formation of 2DEG at the interface of a nonmagnetic polar band insulator $KTaO_3$ and very thin layer of an antiferromagnetic Mott insulator $LaTiO_3$. The 2DEG emerged for two crystal orientation of $KTaO_3$ (110) and (111) showing a high electron mobility $\mu \approx 240$ cm^2/Vs at ~ 2 K and ≈20 cm^2/Vs at 300 K that is two factor larger than that of STO/LAO interface. The critical thicknesses at which the 2DEGs vanished in KTO (110) and KTO (111) interfaces is determined, similarly for the change from a bulk 3D nature to 2D. An initial indication of superconductivity at $KTaO_3/LaTiO_3$ interfaces is evidenced by the onset of a resistivity drop below 4 K.

3.1. Introduction

$SrTiO_3$ (STO)- interfaces have been reported to host various oxide two-dimensional electron gases (2DEGs) of high electron mobilities values (~ 10^4 $cm^2/V.$ s)[24], at low temperatures (<5 K)[11,24,25]. However, these 2DEGs produced small value of electron mobilities at 300 K (< 11 cm^2/Vs)[26]. Few years later following 2DEGs, two dimensional superconductivity (2DS) was found below 1 K in in STO/$LaAlO_3$ (STO/LAO) interfaces[27-32].The electric filed modulation at the oxide interfaces of 2DEG is introduced via applying gate voltage, which leads to tuning of the electron mobilities and sheet carrier densities n_s especially through ionic liquid gating [33]. Such electric field tuning of 2DEGs was also found to contribute in either inducing or enhancing the 2DS in LAO/STO oxide interfaces [34,35]. A significant correlation between the variation of superconducting transition temperature T_c and

the spin fluctuations behavior was observed by Caviglia et al. suggesting the realization of unconventional superconductivity in LAO/STO [36]. Singh et al. observed gate tunned unconventional superconductivity in the LAO/STO interfaces [37]. Interestingly, an observation of 2DS and ferromagnetism was reported in the 2DEG STO/LAO interface [38-40].

Recently a 2DEG was observed in $KTaO_3$ (KTO)- based interfaces with EuO and perovskite oxides such as $LaAlO_3$ and $LaTiO_3$ [41-44]. Similar to STO, shortly after the observation of 2DEG in KTO interfaces with EuO and $LaAlO_3$, a 2DS was discovered in KTO/ EuO and KTO/ $LaAlO_3$ oxide interfaces as well[13,45]. In addition, KTO interfaces with non-oxide materials were also investigated by sputtering of a thin Al metallic layer on KTO (100) and KTO (111)[46]. Ren et al. investigated the dependence of crystal orientation on superconductivity in KTO surfaces using ionic liquid gating, where they observed enhancement of T_c up to 2 K [47]. An electron mobility values of m» 2150, 111, and 285 $cm^2/V.$ s in KTO (100) interfaces with amorphous $LaAlO_3$, epitaxial EuO and $LaTiO_3$ respectively was observed at low temperature[41,42,48]. However, the observed 2DEGs formed on KTO (111) interfaces are very limited. One of such 2DEG systems is KTO (111)/EuO with a high mobility value of 279 cm^2/Vs among all the reported KTO (111)/ oxide interfaces exhibited 2DS[13]. As a 5d metal based oxide, KTO- based 2DEGs are very unique due to the strong spin-orbit coupling (SOC)[49], which is stronger than that of 3d- STO based 2DEGs [36]. Vicente-Arch et al. observed Successful interconversion of spin to charge and charge to spin of high efficiency and Rashba coefficient larger than that of STO-2DEGs[46]. Interestingly, KTO (100)/ $LaTiO_3$ (LTO) 2DEG showed a large mobility value at 300 K (» 21 cm^2/Vs) which is 2 times larger than that of STO- 2DEGs [41]. Moreover, a high-mobility spin- polarized 2DEG (μ » 111 cm^2/Vs at 2 K) was observed in KTO (001)/ EuO interface, and the origin of spin-polarization was attributed to the ferromagnetic nature of EuO. As van Ostaay et al. demonstrated the possibility of generating spin-triplet supercurrent carried by a 2DEG sandwiched by two singlet superconductors [50]. The large spin-orbit coupling ~ one order of magnitude larger than that of STO- based 2DEGs[51], and the higher transition temperature (~ 2.2 K) which is also much higher than that of STO 2DEGs in addition to its

higher mobility at room temperature (~ 21 cm^2/V. s) endorse KTO- 2DEGs to be the right candidate for the new superconducting spintronic generation.

3.2. **Experimental methods**

Epitaxial $SrTiO_3$ (100)/$LaTiO_3$, $LaAlO_3$ (100)/$LaTiO_3$, $KTaO_3$ (100) / $LaTiO_3$, $KTaO_3$ (111) / $LaTiO_3$ and $KTaO_3$ (110)/ $LaTiO_3$ samples were grown by using (VEECO GEN10) molecular- beam epitaxy (MBE). The KTO substrates were firstly chemically pre-cleaned using acetone, methanol and iso-propanol each for 5 mins and dried with nitrogen. The substrates are then cleaned via the outgassing process in the load lock chamber at 4 x 10^{-8} Torr at 200 ^oC in advance to insertion into the growth chamber. Then followed by heating up at 820 ^oC in presence of ozone for 10 mins. The base pressure of the MBE- growth chamber is less than 1 x 10^{-10} Torr before the growth. The $LaTiO_3$ layers are grown at substrate temperature of 800 ^oC and in ozone pressure of 8 x 10^{-8} Torr. The samples are then cooled to 700 ^oC in ozone and consequently cooled down to room temperature. The $KTaO_3$/ $LaTiO_3$ samples prepared at different ozone pressures were studied as well. Elemental composition analysis and depth profile of the samples were inspected using Rutherford backscattering spectroscopy (RBS) and (Thermo-Avantage) x-ray photoelectron spectroscopy. Reflection high-energy electron diffraction (RHEED- KSA) was used to in-situ inspect the growth quality of the thin film layer on the $KTaO_3$ substrates. The surface topography and roughness of the samples is scanned by the atomic force microscopy (Bruker) instrument. The crystal structure was investigated using a high-resolution x-ray diffractometer (HR-XRD, D8- Bruker). The magnetic properties are studied by using Quantum Design MPMS3- (SQUID) magnetometry. The electrical Hall effect measurements were performed by using the Quantum Design Dynacol physical property measurement system (PPMS) using Van-der Pauw geometry method.

3.3. **Results**

Figure 3.1 provides a schematic illustration of the crystal structures for both the single crystal substrates and the $LaTiO_3$ (LTO) thin film overlayer. The two different structures of $LaTiO_3$ are shown in Fig. 3.1 (a) and (b), while the $SrTiO_3$ (STO) and $KTaO_3$ (KTO) substrates are depicted in Fig. 3.1 (c) and (d), respectively. Single crystals of $KTaO_3$, $SrTiO_3$ (at 300 K), are classified as a cubic perovskite structure. While bulk single crystals of $LaAlO_3$ possesses a

distorted rhombohedral perovskite structure, it can be stabilized in a pseudo cubic unit cell during thin-film growth with a lattice constant ≈ 3.87Å. On the other hand, bulk $LaTiO_3$ adopts an orthorhombic structure (Space group: Pnma)[52]. Although the orthorhombic structure of bulk LTO, however, our high-resolution x-ray diffraction (HR-XRD) experiments proved the single phase and epitaxial growth of LTO along various substrates (STO, KTO, LAO, MgO).

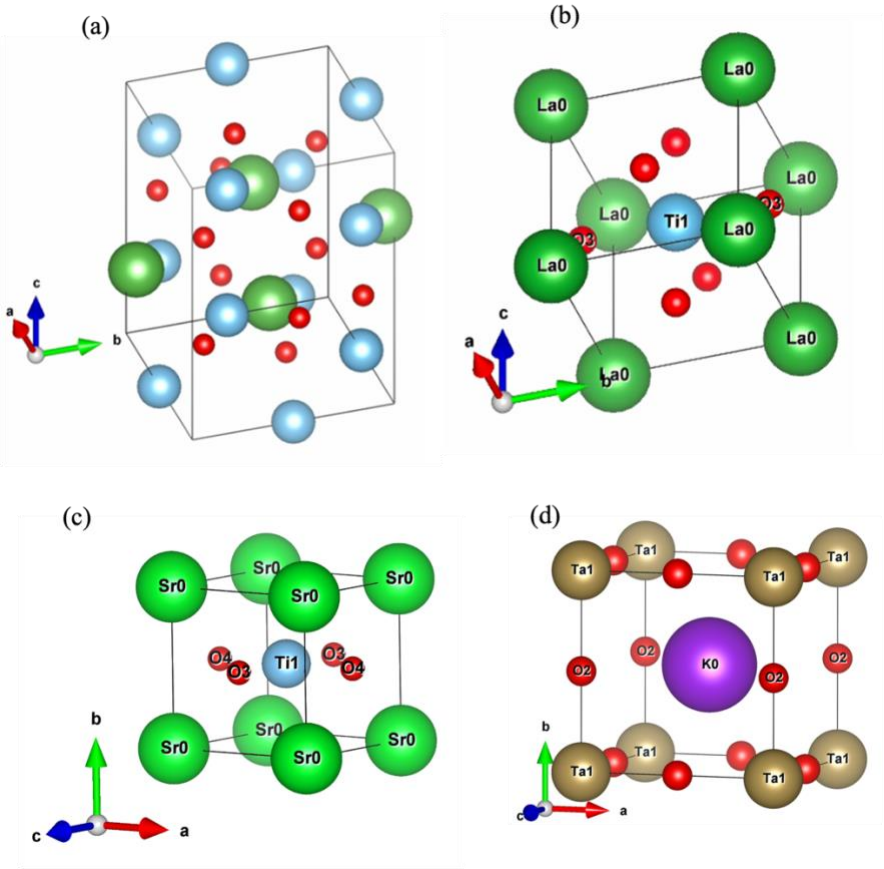

Figure 3.1. Schematic representation of the crystal structure of single crystals: (a) Orthorhombic $LaTiO_3$ phase, (b) Cubic $LaTiO_3$ phase, (c) Cubic $SrTiO_3$ phase and (d) Cubic $KTaO_3$.

In order to inspect the structure and epitaxial growth of the deposited thin films, we performed XRD scan measurements. XRD diffractograms patterns of $LaTiO_3$ thin film grown along both LAO (100) and STO (100) are shown in Fig. 3.2 (a, c), respectively, these diffraction

patterns indicate the single-phase growth and are preliminary indications of the epitaxial growth. The reflection high-energy electron diffraction (RHEED) patterns for both samples are shown in Fig. 3.2 (b) and inset of Fig. 3.2. (c) both are depicting streaks RHED patterns which reflects the epitaxial growth of LTO along LAO (100) and STO (100), respectively. The topography scan of the STO (100)/LTO grown sample we inspected using atomic force microscopy (AFM) as shown in Fig.3.2 (d), in which a step-terraced surface of STO/LTO film was obtained, this indicates the perfect surface quality of the grown LTO film with a minimum root-mean square (RMS) roughness value of less than 0.185 nm.

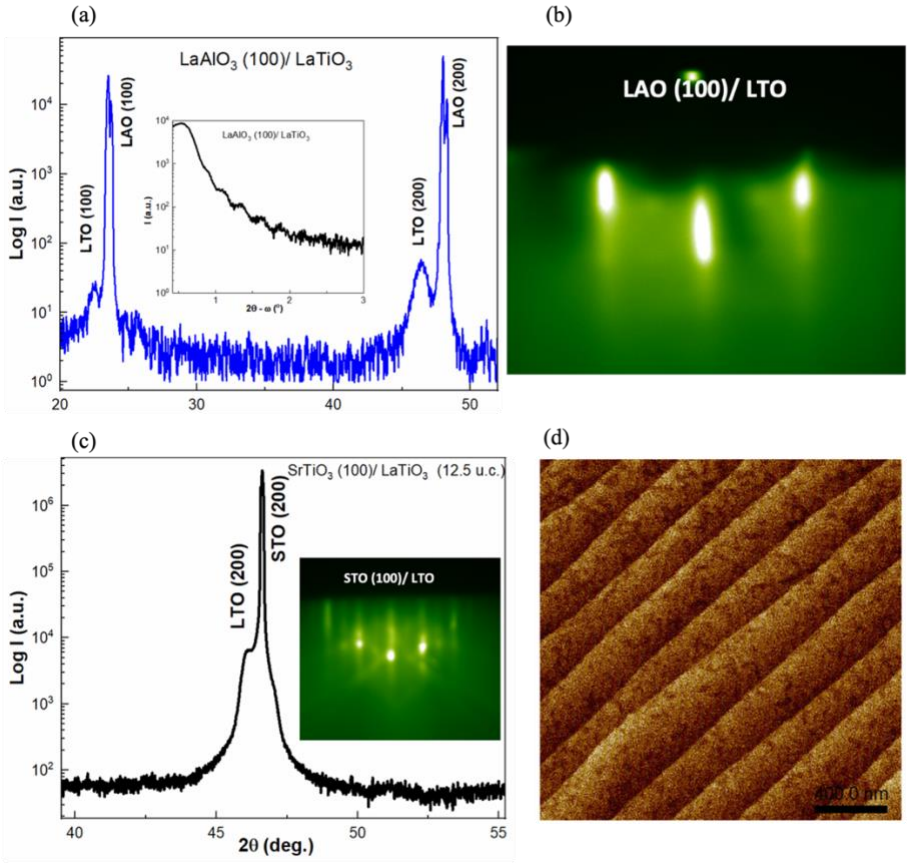

Figure 3.2. Structure and surface characterization of LTO film. (a) XRD pattern of the LTO film along $LaAlO_3$ (100), the inset shows the x-ray reflectivity oscillations of the same film indicating the surface homogeneity of the grown film, (b) Reflection high-energy electron diffraction pattern of the LAO (100)/LTO film which shows a streak RHEED pattern, (c) the XRD diffraction pattern of STO (100)/LTO (12.5 u.c.), the inset illustrates the RHEED pattern

of same sample. (d) Atomic force microscopy topography scan of the STO (100)/LTO (12.5 u.c.) sample shows step-terraced surface after the growth of LTO film.

One of the main questions of this thesis, is there an exotic property we can see at the interface? Such as superconductivity or ferromagnetism. Thereby, we performed electrical transport measurement to inspect this motivation. Temperature dependence of electrical resistivity of STO (100)/LTO (21 nm) sample is shown in Fig. 3.3. Interestingly a superconductivity at transition temperature below T ~ 1.5 K was observed in this interface sample, However, the reproducibility of the superconductivity in these interfaces was proven

to be very challenging, this seems to be mostly because STO is a plenty source of oxygen vacancies which is impossible to control.

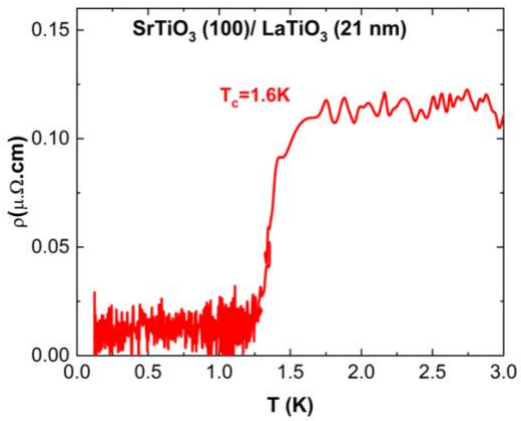

Figure 3.3. Temperature dependence of electrical resistivity of STO (100)/LTO (21 nm) sample.

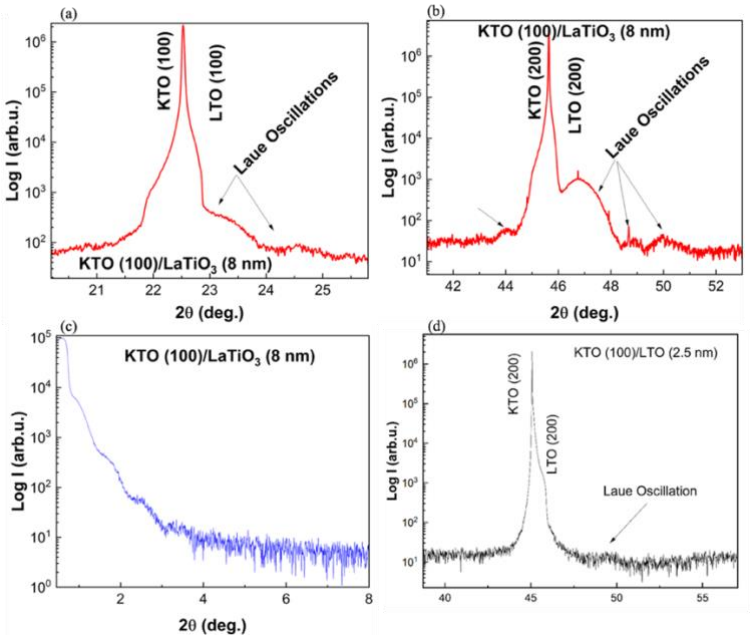

Figure 3.4. X-ray diffraction patterns of $KTaO_3$ (100)/ $LaTiO_3$ thin interfaces. (a) XRD of KTO (100)/ LTO (8 nm) at the first peak (100), (b) XRD pattern of KTO (200)/LTO (8nm) along the second peak (200), (c) x-ray reflectivity of same sample shows the oscillations used to determine the film thickness, (d) XRD pattern of KTO (100)/LTO (2.5 nm) sample.

Due to the challenges in reproducing superconductivity at $SrTiO_3/LaTiO_3$ interfaces, primarily caused by oxygen vacancies, we shifted our focus to an alternative substrate: $KTaO_3$ (KTO). KTO offers a lattice constant (3.989 Å) that closely matches the pseudo-cubic phase of $LaTiO_3$ [53],and exhibits a strong spin-orbit coupling strength an order of magnitude greater than that of STO [51]. The X-ray diffractograms ($\boldsymbol{\theta - 2\theta}$) scans of KTO (100)/ LTO (8nm) sample at (100) and (200) peaks are shown in Figure 3.4 (a-b) which shows the single-phase growth of LTO thin film on KTO (100) substrate with a presence of Laue oscillations. Figure 3.4(c) shows the x-ray reflectivity (XRR) of the same sample, that was used for thickness determination, the XRR shows that the KTO (100)/LTO has a smooth surface which matches with the high-quality growth as indicated in the XRD patterns in Figure 3.4(a-b). The XRD of another sample KTO (100)/LTO (2.5 nm) was shown in Figure 3.4(d) at LTO thickness of 2.5 nm. To inspect the growth of LTO on various crystallographic orientations of $KTaO_3$ substrates, x-ray diffractograms of KTO (110)/ LTO and KTO (111) /LTO at different thickness of LTO (t_{LTO}) are shown in Figure 3.5 (a, b) and Figure 3.5 (c) respectively. The diffraction patterns illustrate the presence of Laue fringes in KTO (110) system and shows epitaxial crystalline peaks of LTO in the KTO (111) system which reflects the high-quality and the epitaxial growth of LTO along (110) and (111) crystal planes. The inset to Fig. 3.5 (c) displays the RHEED pattern of KTO (111)/LTO sample, indicating the epitaxial growth. The measured lattice parameter of the grown LTO layer was found to be ($a_{LTO\,(110)} \approx 3.955$ Å) when $t_{LTO\,(110)} \approx 5$ nm, whereas in case of KTO (111)/ LTO at ($t_{LTO} \approx 19$ nm) the lattice constant ($a_{LTO\,(111)} \approx 3.951$ Å) which is very close to that of KTO substrate. The lattice mismatch in KTO (111)/ LTO was found to be varied from 0.54 % up to 2.9 % based on the value of $t_{LTO\,(111)}$. The specular x-ray reflectivity (XRR) of the KTO (111)/LTO (8 nm) sample is shown in Fig. 3.5 (d), the observed oscillations reveal the smooth surface and homogeneity of the grown film.

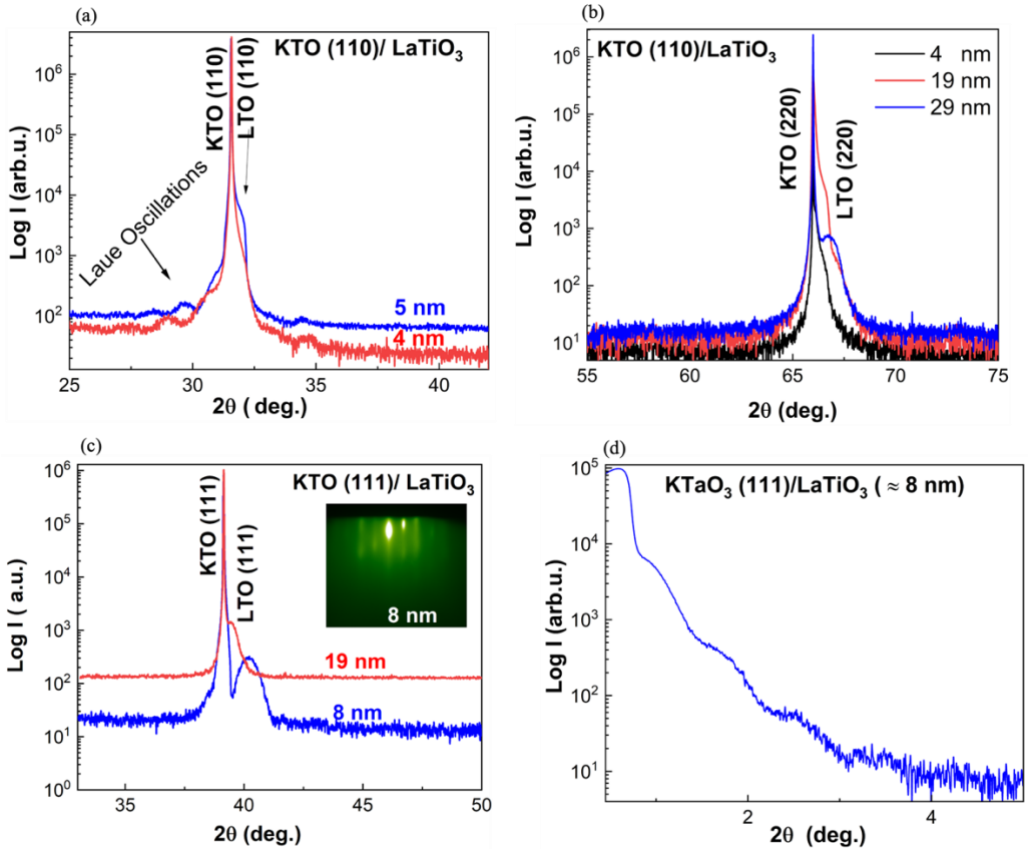

Figure 3.5. crystal structure of (110) and (111)- oriented KTO/$LaTiO_3$ interface. (a) XRD pattern of KTO (110)/LTO at 5nm and 4 nm thick LTO along the first peak (110) showing the Laue oscillations, (b) XRD patterns of KTO (110)/LTO along the second peak (220) at various thickness of LTO (4 nm, 19 nm and 29 nm). (c) XRD patterns of KTO (111)/LTO interfaces at various thickness of LTO layer, the inset shows the RHEED pattern of the KTO (111)/LTO (8nm) interface.

The XRD pattern of our fabricated KTO (110)/LTO (4 nm) sample exhibits Laue oscillations, indicating high crystal quality (Fig. 3.6 (a)). This result is compared with the reported XRD pattern of KTO (110)/LTO by Maryenko et al., shown in Fig. 3.6 (b), where our sample demonstrates comparable or even superior quality[53].

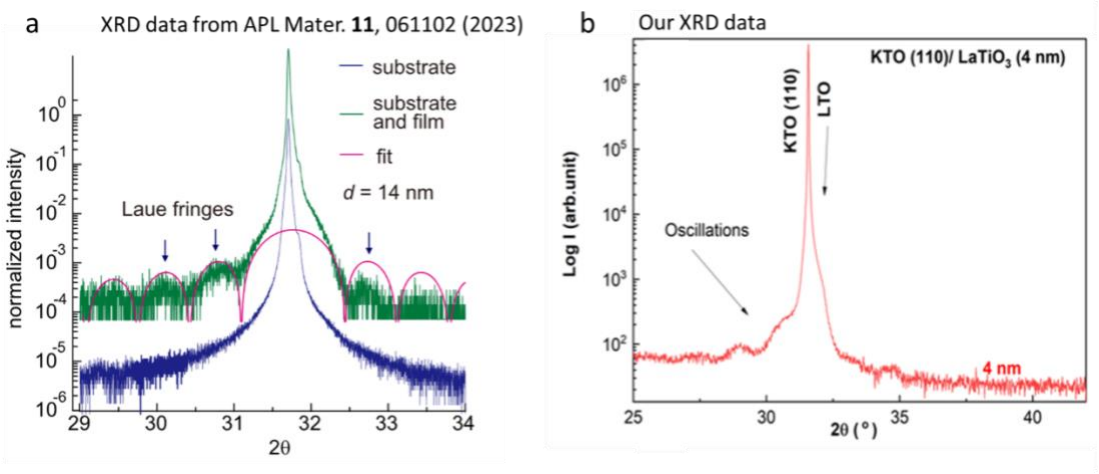

Figure 3.6. A comparison shows the XRD- Laue oscillation in the KTO (110)/LTO (4 nm) sample of this work and in sample shown in Maryenko, et al. work [53].

We checked the surface quality of the heterostructure via RHEED which showed streaks pattern for KTO (110) and KTO (111) interfaces. The RHEED patterns of KTO (110)/LTO at various thickness values of the grown LTO overlayers as well as for KTO (111)/LTO (8 nm) interfaces are shown in Fig. 3.7 (a), the images show a clear streaky RHEED patterns which is a direct indication of the epitaxial growth of LTO along KTO single crystals along (110) and (111)- orientations. The layer-by-layer growth of LTO films along KTO crystals is confirmed by the real time RHEED oscillations as shown in Fig. 3. 7 (b). The low energy-electron diffraction patterns show the excellent crystallinity of the KTO (110)/LTO interfaces as illustrated in Fig. 3.7 (c-d).

The surface topography is very crucial parameter in controlling the interfacial properties of MBE-grown heterostructures, our grown KTO/ LTO samples showed root mean square roughness RMS less than 0.2 nm which confirms the smooth and sharp surface of the grown structures as shown in Fig. 3.8.

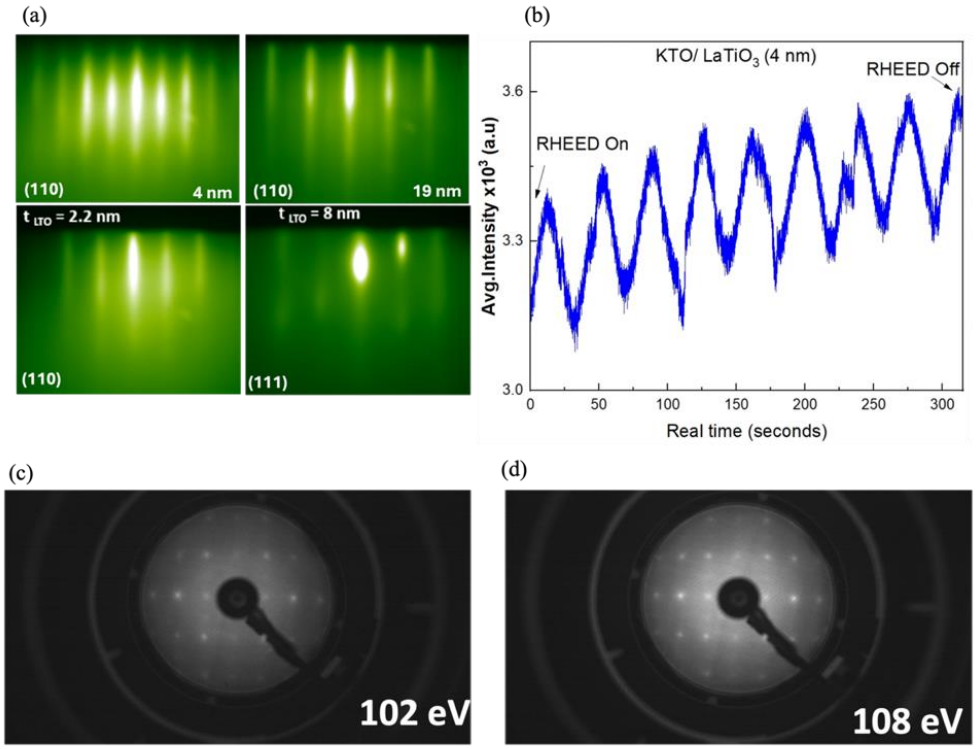

Figure 3.7. (a) High energy- electron diffraction (RHEED) patterns of (110)- and (111)-oriented KTO/LTO interfaces at various thickness of LTO layer. (b) RHEED oscillations of the KTO/ LTO (4nm) sample shows the layer-by layer growth of LTO along KTO substrates. (c-d) In- situ low energy -electron diffraction (LEED) pattern was performed inside the angle resolved photoelectron emission spectroscopy (ARPES) chamber for the KTO (110)/LTO (2 nm) sample at 102 eV and 108 eV energies.

The atomic force microscopy (AFM) scans of KTO (110)/ LTO sample illustrate the existence of terraced steps shape whereas it was found to be absent in the KTO (111)/ LTO interfaces which may explain the existence of the Laue oscillations in case of KTO (110)/LTO as provided by the XRD patterns shown in Fig. 3.5.

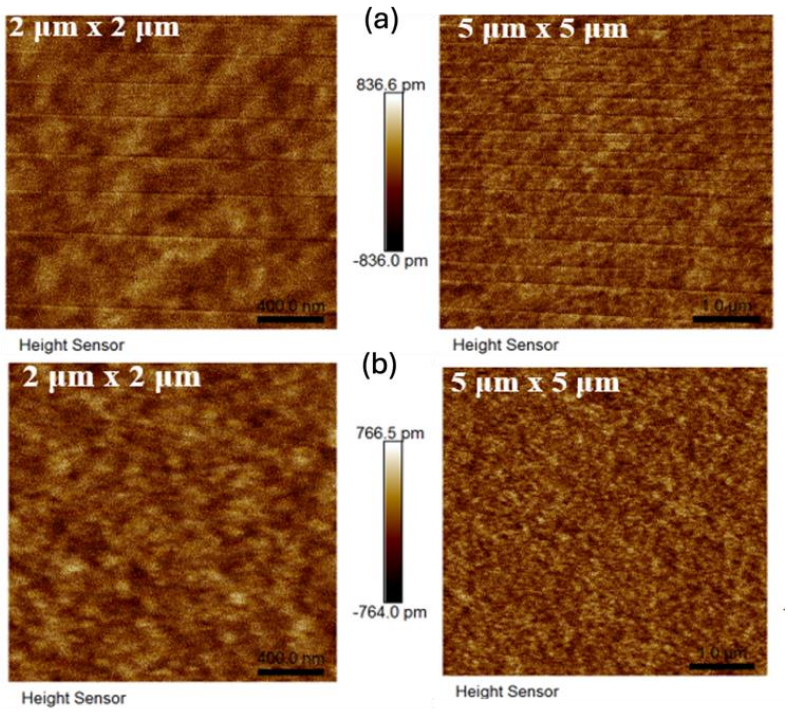

Figure 3.8. Atomic force microscopy (AFM) topography scans of (a) KTO (110)/LTO at 2 µm x 2 µm and 5 µm x 5 µm scan area, (b) KTO (111)/LTO interfaces. The RMS roughness value is ~ 0.21 nm for both interfaces.

Although it is well known that growth of LTO is very challenging particularly along KTO (111) orientations, however, our experimental results proved the high-quality of the grown films. To further confirm the epitaxial growth of LTO films along (110)- and (111) - oriented interface we have performed **ϕ**- scan measurements using HR-XRD as shown in Fig. 3. 9. The scans along [210] and [211] reflections for (111)- and (110)- oriented interfaces, respectively show the alignment of the LTO film peaks with the KTO substrate peaks at same angles, the measurement was performed for several samples of various LTO thickness. Thereby, our experimental results perfectly confirm the excellent epitaxial growth of LTO films along KTO (110) and KTO (111) oriented interfaces. The model used for performing the **ϕ**- scans is based on cubic KTO and LTO model, which also is another way to confirm that our LTO films are of a pseudo cubic structure [53,54].

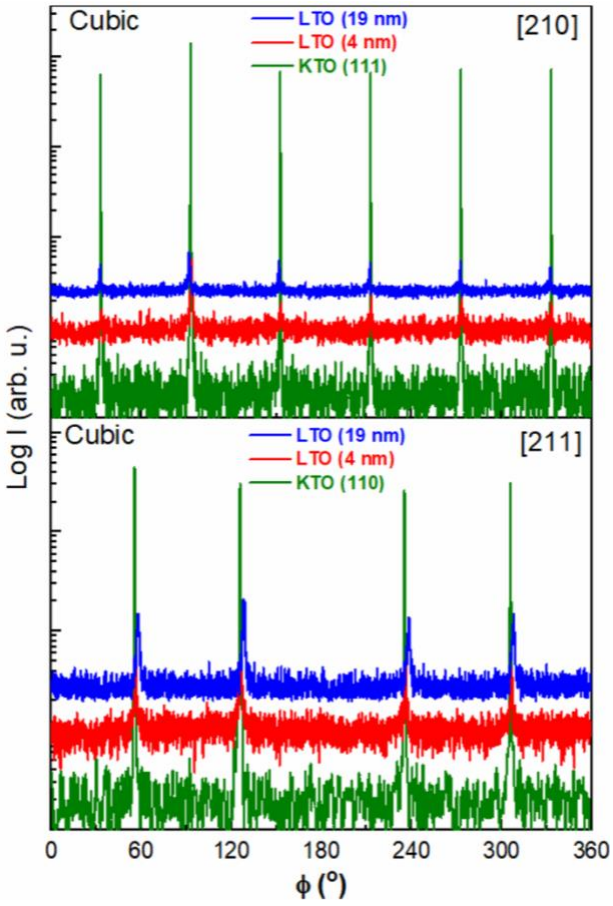

Figure 3.9. $\boldsymbol{\phi}$- scans measurement of (110)- and (111)- oriented KTO/LTO interfaces at various thickness of LTO layer; the scans were performed at [210] peak for KTO (111) oriented interfaces and at [211] for KTO (110) oriented interfaces.

A detailed truncation rods measurement and analysis at (H K L) planes of KTO (110)/LTO (4 nm) interface were performed using Ga-jet HR-XRD, in which the intensity and resolution is comparable to the synchrotron radiation. The analysis showed the occurrence of Laue oscillations at various truncations including (1 1 L) and (2 0 L) as shown in Fig. 3.10 (a, b). Although through this measurement we saw a well-defined interface with almost no chemical roughness, overall disorder of the order of rms = 0.2- 0.3 angstroms are seen in the interface which may suggest the presence of TiO_6 titling. This titling in TiO_6 is very crucial in tuning the crystal structure at the interface which may lead to exotic phenomena.

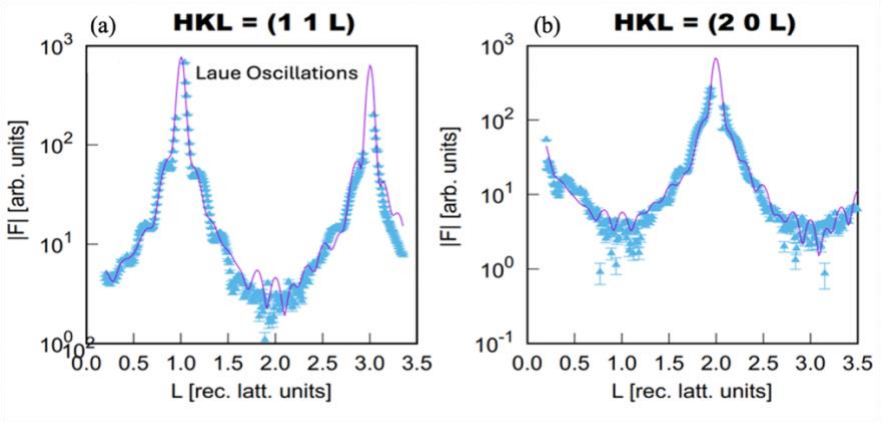

Figure 3.10. Truncation rods analysis of KTO (110)/LTO (4 nm) sample at (a) H K L= (1 1 L) and (b) at H K L = (2 0 L).

The strain which was observed in the KTO (111)/LTO thin films as provided in the shift of the peak's positions in XRD ($\boldsymbol{\theta - 2\theta}$) diffractograms as shown in Fig. 3.5 is supported by the reciprocal space mapping (RSM) measurement. The RSM maps were performed at the asymmetric (111) peaks of the KTO (111)/LTO at two various LTO thickness (t_{LTO}) = 8 nm and 11.2 nm as shown in Fig. 3.11 (a) and Fig. 3.11 (b), respectively. The RSM maps indicate that the LTO films are strained along the KTO substrates, with this strain being more pronounced in the thinner (8 nm) LTO film. This strain is likely due to the TiO_6 octahedral tilting predicted from the truncation rod analysis.

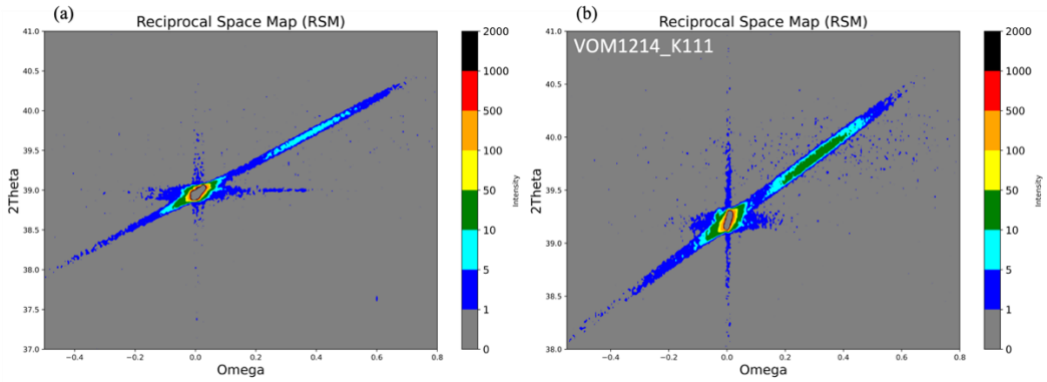

Figure 3.11. Reciprocal space mapping measurement for: (a) KTO (111)/LTO (8 nm and (b) KTO (111)/LTO (11.2 nm) interfaces performed at asymmetric peak (111) indicates the epitaxial strain of the $LaTiO_3$ film on $KTaO_3$ (111) substrate.

Although growing $LaTiO_3$ is challenging since Titanium's valence state in case of LTO is 3+, however, Titanium is well known to be typically more stable in the 4+ valence state. However, we successfully obtained a well-defined interface in KTO/LTO sample. Fig. 3.12 (a) depicts the high- resolution image taken by the scanning transmission electron microscopy (STEM) of KTO (110) /LTO (8.4 nm) which shows a well-defined interface. The fast Fourier transform FFT of the LTO thin film at three various areas of the sample is shown in red, green and blue labeled squares as illustrated in Fig. 3.12 (b-d) indicating that although the well-defined interface of KTO/LTO, a disorder is present. FFT of the $KTaO_3$ (110) substrate is shown in

Fig. 3.12 (e). Overall, the FFT and STEM images show the excellent growth of LTO and KTO with a well-defined interface.

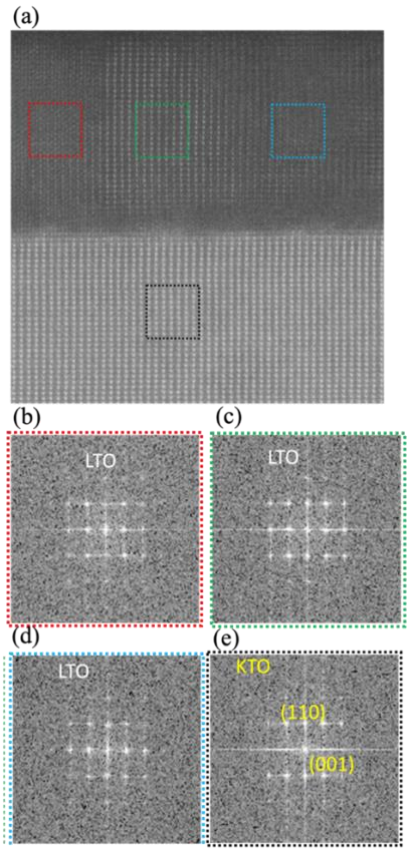

Figure 3.12. (a) STEM of KTO (110)/LTO (8.4 nm) sample, the fast Fourier transform (FFT) of the LTO film taken at various regions of the film represented by the red, green and blue colored squares on the STEM image shown in b, c, d, respectively, (e) shows the FFT of the KTO (110) substrate.

Additionally, we grew another sample in which we capped KTO/LTO with an amorphous layer of LTO [KTO (110)/LTO (4 nm) / LTO (amorphous)] to protect the LTO overlayer during the lamella preparation as shown in Fig. 3.13. The STEM image of the capped KTO (110)/LTO (4nm) is shown in Fig. 3.13 (a), and the corresponding FFT patterns are shown in Fig. 3.13 (c-d) for the LTO film and KTO substrate, respectively. The STEM experimental results show the formation of a sharp KTO (110) /LTO interface with a presence of a structural disorder in

the $LaTiO_3$ layer at the interface, interestingly this matches with the disorder observed in the truncation rods analysis given by the HR-XRD which was calculated to be in the order of rms = 0.2- 0.3 angstroms. Nevertheless, the HR-XRD, RHEED, LEED, phi-scans, AFM and RSM measurements all confirm the high-quality of the grown KTO/LTO interfaces along (100), (110) and (111)- oriented KTO substrates. The obtained disorder at the interface is co-observed with the high-quality epitaxial growth of LTO along KTO could indicate the presence of structural modulation as function of the TiO_6 octahedral in $LaTiO_3$ layer at the interface.

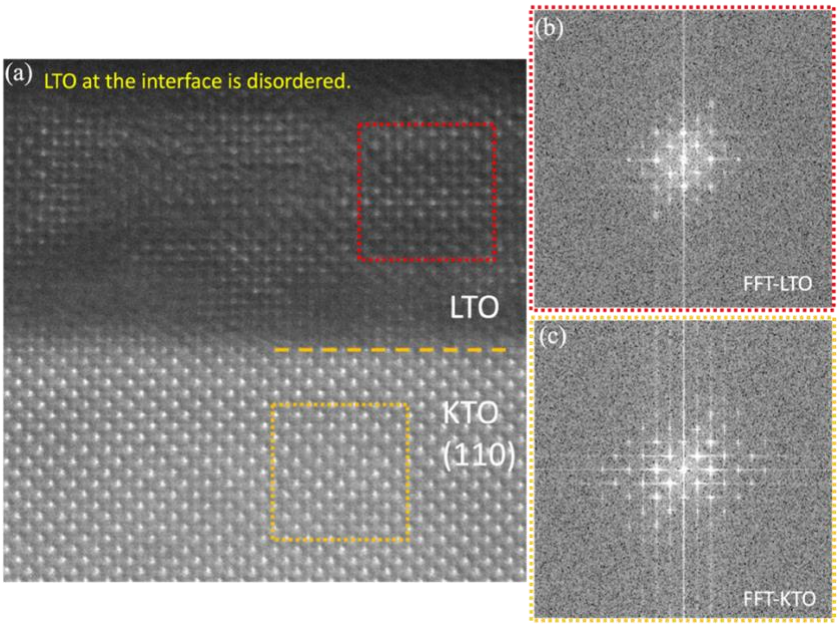

Figure 3. 13. Scanning transmission electron microscopy (STEM) of the capped sample; KTO (110)/ LTO (4 nm)/ LTO (amorphous). (a) High resolution ADF image. (b) FFT of the LTO (4 nm) thin film layer. (c) FFT of the KTO (110) substrate.

Furthermore, the strain is investigated using the geometrical phase analysis algorithms (GPA) [55],based on the processing by strain ++ code of the ADF (STEM) images obtained from our experimental results as shown in Fig. 3.14 (a, b). The GPA analysis shows the presence of strain gradient in the KTO/LTO sample which supports the presence of distortion (tilting) of the TiO_6 octahedral at the well-defined interface. This TiO_6 is pronounced particularly at the ε_{xx} and ε_{yy} strain tensor's components. The Bragg reflection planes clearly indicate the presence of tilting at (001) and (110) filtered planes as shown in Fig. 3.14 (b) in the Brag images.

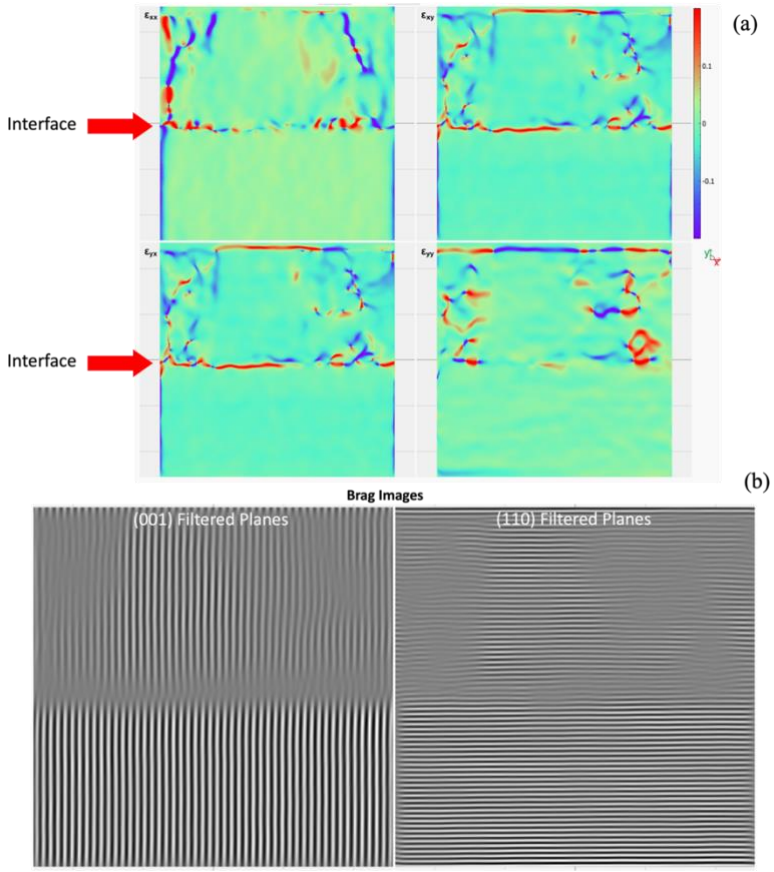

Figure 3. 14. Geometrical phase analysis of strain components of (a) KTO (110)/LTO interface, (b) Brag images of (001) and (110) filtered planes.

The substrate temperature during the growth of $LaTiO_3$ plays a crucial role in the optimization of the $LaTiO_3$ phase of the deposited film. Although the grown LTO film at substrate temperature of 600 ^{o} C showed better metallic behavior of a higher residual resistivity ratio (RRR) better than the other substrate temperatures as shown in Fig. 3.14 (a), however, we selected the substrate temperature at 800 ^{o}C to be the optimum temperature for the LTO deposition. The LTO growth is very challenging especially considering the valence state of titanium which is more stable in the Ti^{4+} state, however when growing LTO, we are pushing Ti to take the Ti^{3+} state which is very tricky to control. However, through a careful growth optimization process, we found that at high Ozone pressure (> 3 x10^{-7} Torr) the titanium prefers the Ti^{4+} state, while at lower growth ozone pressure, it prefers the Ti^{3+} state especially at 8 x

10^{-8} Torr, which we selected to be the optimum ozone pressure for the growth as shown in Fig. 3.15 (b). The reason is because at 800 ºC a better structure and surface topography of the deposited $LaTiO_3$ thin films along KTO substrates are obtained.

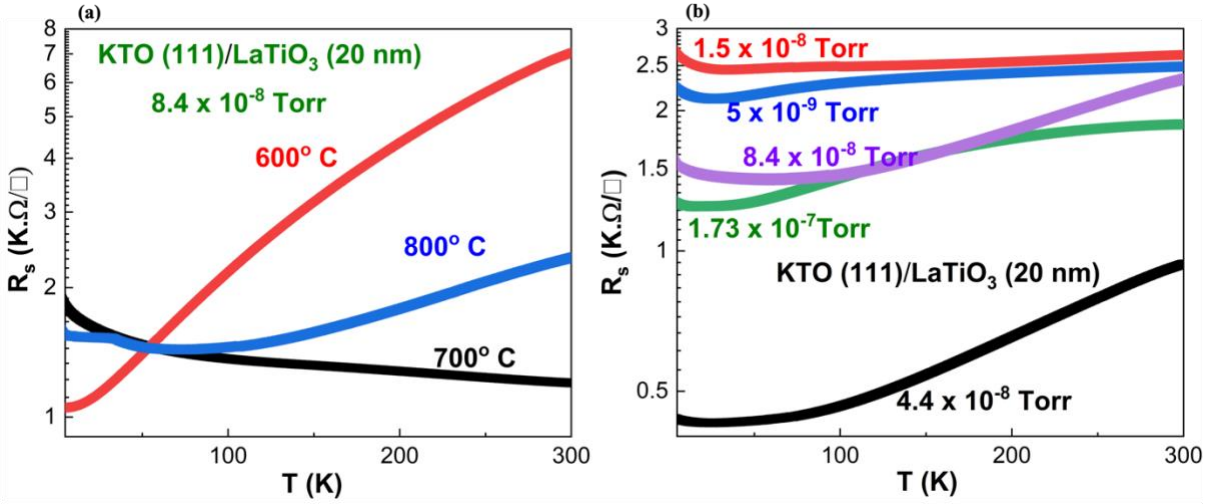

Figure 3. 15. Optimization conditions for KTO/ $LaTiO_3$ thin film heterostructure grown by the molecular beam epitaxy (MBE): (a) The KTO/ LTO at various substrate temperature of the growth at Ozone pressure of 8.4 x10^{-8} Torr, (b) The KTO/LTO at various Ozone pressure of the growth, all the films here were grown are of (20 nm) thick.

We studied the transport behavior particularly the sheet resistance of the grown LTO film as function of temperature for KTO (111)/LTO interfaces by variation the LTO thickness. We noticed that when LTO overlayer thickness is thick (> 20 nm) the metalic behavior (RRR) drastically drops and shows a resistance minimum , in which the sheet resistance increases by decreasing the temperature as shwon in Fig. 3.16. This provides indirect evidence of two-dimensional (interface) conduction at our KTO/LTO interfaces. Specifically, it indicates that thinner LTO layers exhibit metallic behavior, while thicker LTO layers show a reduction in metallicity at low temperatures. This trend supports the interfacial conduction feature, attributed to the formation of a two-dimensional electron gas (2DEG) layer.

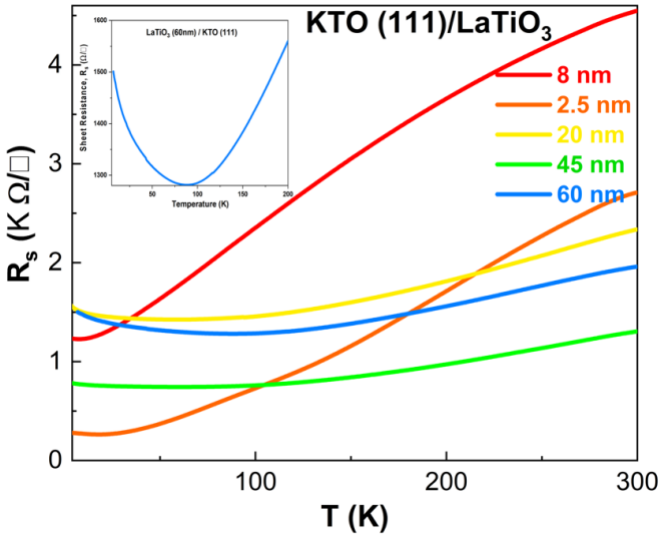

Figure 3. 16. Temperature dependence of KTO (111)/LTO as a function of the $LaTiO_3$ thickness, the inset shows the resistance minimum for thicker LTO samples.

The electrical transport properties of the KTO/LTO heterointerfaces have been investigated for both (110)- and (111) – optimized KTO/LTO interfaces as shown in Fig. 3. 16. The sheet resistance as function of temperature for KTO (111)/LTO interfaces shows very good metallic behavior with an RRR value exceeding 90 at certain thickness of LTO layer (t_{LTO}), similarly for the KTO (110)/LTO interfaces as shown in Fig. 3.17 (a) and Fig. 3.17 (b), respectively. The sheet resistance as function of temperature, R_s (T) shows another indication of the two-dimensional (2D) conduction in our KTO/LTO interfaces at both orientations at various thickness of LTO as shown in Fig. 3.17. Please note that the two dimensional electron gases (2DEGs) along KTO (100)/LTO, was reported before this work by Zou et al. [41], then we did no focus on investigating the 2DEGs along KTO (100) orientations.

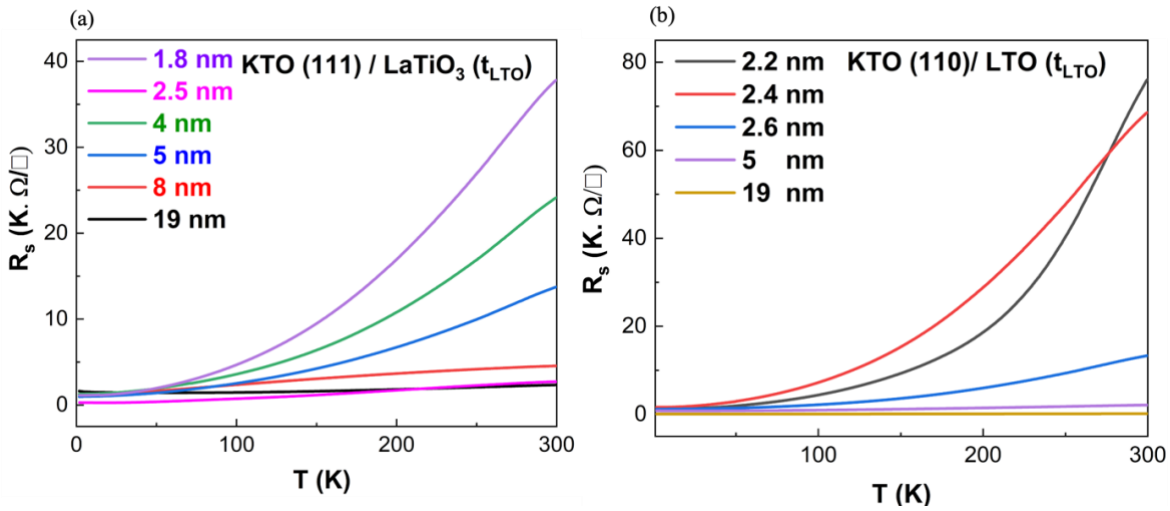

Figure 3. 17. Temperature dependence of sheet resistance for the optimized KTO/LTO heterostructure as function of the LTO layer thickness, for both (a) KTO (111)/LTO and (b) KTO (110) LTO interfaces.

The electron mobility and sheet carrier densities extracted from the Hall effect measurement reach an electron mobility value up to 250 $cm^2/V.\ s$ in KTO/LTO 2DEGs as shown in Fig. 3.18 (a, b). A sheet carrier density up to 1 x 10^{14} $/cm^2$ and 5 x 10^{14} $/cm^2$ at low and room temperature, respectively was found in case of KTO (111)/LTO (2.5 nm) interface as shown in Fig. 3.18 (a), the electron mobility and sheet carrier density behave differently in case of KTO (111)/LTO in which electron mobility increases by decreasing the temperature. On the other hand, a lower sheet carrier density of up to 1 x 10^{13} / cm^2 at room temperature was observed in case of KTO (110)/LTO (2.2 nm) 2DEGs, the electron mobility and sheet carrier density are behaving similarly as a function of temperature in this case as shown in Fig. 3.18 (b). It is noticed that n_s increases with increasing temperature for the case of KTO (110)/LTO system, this behavior could be attributed to the absence of external perturbations on the quantum paraelectric behavior of KTO at higher temperatures [56,57].

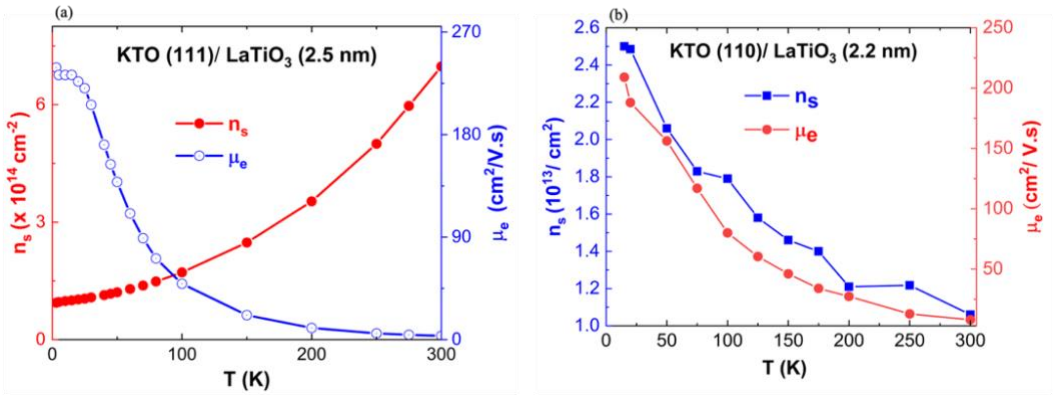

Figure 3. 18. Temperature dependence of electron mobility and sheet carrier density in (a) KTO (111)/LTO (2.5 nm) and (b) KTO (110)/LTO (2.2 nm).

Two- dimensional electron gases were formed at various thickness of LTO overlayer and resulted in high electron mobility in case of KTO (111)/LTO and KTO (110)/LTO interfaces at various temperatures (20 K, 150 K, and 300 K) as shown in Fig. 3.19 (a, b), the electron mobility shows the peaked value at low temperatures, the thinner the t_{LTO} is the higher the electron mobility is obtained.

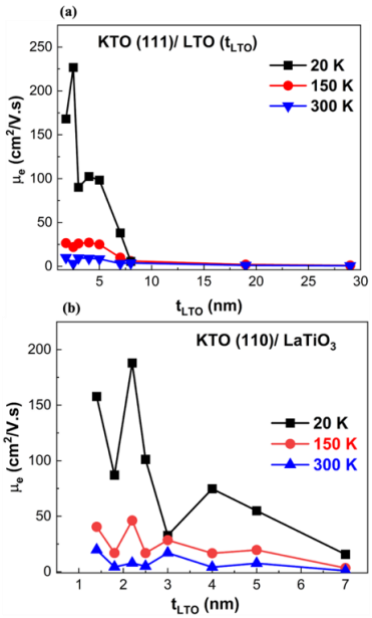

Figure 3. 19. Electron mobility as function of LTO thickness at various (20 K, 150 K, 300 K) temperatures for (a) KTO (111)/LTO 2DEGs, and (b) KTO (110)/LTO 2DEGs.

To determine whether the observed conduction is two-dimensional in nature or arises from surface conduction caused by defects or vacancies, we conducted a series of experiments to confirm or rule out 2D conduction in KTO/LTO interfaces. The evidence of two -dimensional conduction observed at our interfaces is supported by the non-monotonic behavior of the sheet resistance as function of t_{LTO} for both KTO (111)/LTO and KTO (110)/LTO interfaces as shown in Fig. 3.20 (a) and (b), respectively. At various temperatures (3 K, 20 K, 50 K, 150 K, 30 K) the thickness dependence of sheet resistance shows non-monotonic behavior which confirms the 2D conduction and provides evidence that these interfaces host 2DEGs [41].

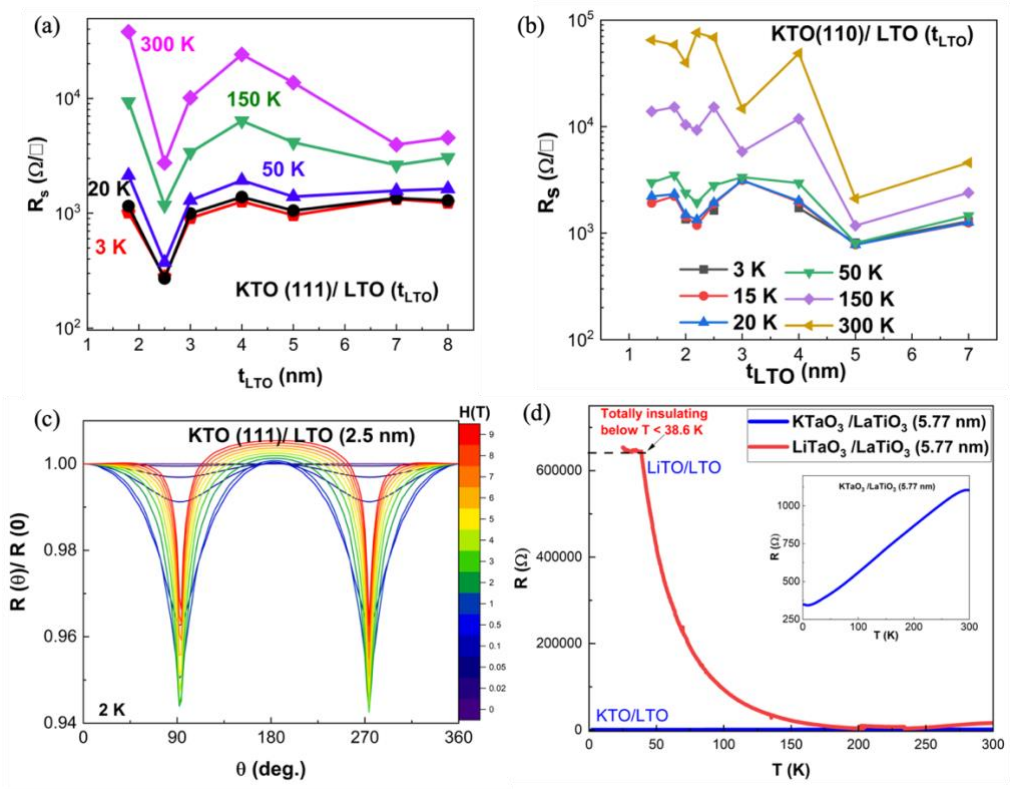

Figure 3. 20. Evidence of two- dimensional conduction in $KTaO_3$/ $LaTiO_3$ interfaces. (a) Sheet resistance as function of LTO later thickness for KTO (111)/LTO and (b) KTO (110)/LTO at 3K, 20 K, 50 K, 150 K and 300 K. (c) Angular dependence of magneto resistance (AMR) at various applied magnetic fields shows a 2-folded shape for an exemplary KTO (111)/LTO (2.5 nm) sample. (d) Temperature dependence of electrical resistance for $KTaO_3$ (111)/ $LTiO_3$ (5.77 nm) and $LiTaO_3$ (11-10)/$LaTiO_3$ (5.77 nm) samples, shows the insulating behavior when LTO

is grown on different substrate. The inset to Fig.3. 20(d) displays the metallic behavior of the KTO (111)/$LaTiO_3$ sample.

Additionally, the anisotropic magnetoresistance (AMR) as function of the applied magnetic field as shown in Fig. 3.20 (c) reveals a 2- folded shaped AMR which shows two-sharp dips at 90^o and 270^o. This reflects the planar symmetry and the electron motion confinement in a plane, which provides additional confirmation the 2D conduction of our KTO/LTO interfaces [42]. Furthermore, we have performed several control experiments in which we grew $LaTiO_3$ along various single crystal substrates such as LAO, MgO, Al_2O_3 and $LiTaO_3$, in all these cases we did not observe any metallic behavior such that was observed in case of growing $LaTiO_3$ along $KTaO_3$ substrates. For example, in case of MgO (100) / $LaTiO_3$ thin films showed completely insulating behavior at room temperature. Additionally, we grew $LaTiO_3$ along another oxide substrate ($LiTaO_3$) which has strong spin-orbit coupling similar to $KTaO_3$, in Fig. 3.20(d) we show a comparison between the growth of $LaTiO_3$ on top of $LiTaO_3$ and on top of $KTaO_3$.

The $LiTaO_3$/$LaTiO_3$ (5. 77 nm) interface showed an insulating behavior and becomes completely insulating below 50 K, but in case of $KTaO_3$/ $LaTiO_3$ (5. 77nm) it shows a pure metallic behavior of high RRR value, indeed when the $LaTiO_3$ thickness is below 5 nm the $LiTaO_3$/ $LaTiO_3$ interface is even completely insulating at room temperature. This control experiment as shown in Fig. 3.20 (d) clearly confirms the 2D conduction and conclude that the conduction in KTO/$LaTiO_3$ interfaces is not due to the $LaTiO_3$ overlayer but is purely due to the interface.

The phase diagram of KTO (111)/LTO samples is illustrated in Fig. 3.21, where electron mobility and the residual resistance ratio (RRR) are plotted as function of the LTO layer thickness ,t_{LTO}. This diagram reveals the impact of thickness on 2D and 3D conduction characteristics, as well as on the ferromagnetic and antiferromagnetic behaviors at the KTO/LTO interface. Both the electron mobility at 3K and 150K, along with the RRR, are shown as functions of the LTO thickness.

Our experiments indicate that the formation of two-dimensional electron gases (2DEGs) in KTO/LTO interfaces, oriented along both (110) and (111), emerges only beyond specific thickness thresholds. For KTO (111)/LTO 2DEGs, this critical thickness is 4.5 unit cells—below which the interface is insulating—whereas, for KTO (110)/LTO, it is 3.5 unit cells. The phase diagram in Fig. 3.21 identifies these critical thickness values: below this threshold, the interface is insulating, while beyond it, conduction is no longer purely two-dimensional. The formation of 2DEGs is observed within this range of thicknesses.

Notably, as we will explore in the next chapter, we observe the emergence of ferromagnetism within the 2DEGs at the interfacial layer near the KTO substrate, which then diminishes above the thickness limit for 2D conduction (as illustrated in Fig. 3.21). The electron mobility in the 2DEGs is significantly reduced with increasing LTO thickness, as is the RRR. This suggests that as the LTO layer thickens increases, its bulk properties start to dominate, suppressing the two-dimensional conduction, reducing electron mobility, and decreasing the metallicity of the interface, as also reflected in the RRR values.

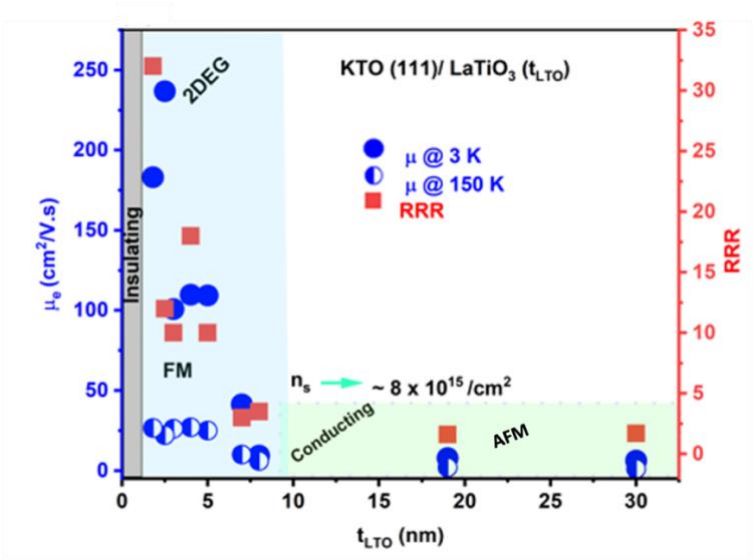

Figure 3. 21. Phase diagram of KTO (111)/$LaTiO_3$ two-dimensional electron gases.

Interestingly, the temperature dependence of electrical resistivity of $KTaO_3$ (111)/$LaTiO_3$ (7 nm) sample showed a drop of the resistivity at an onset temperature below 4K as shown in Fig. 3. 22. Despite this drop of the electrical resistivity is not ending by a zero

resistivity, however, this is a clear and strong indication of the superconductivity signatures expected below 2K in this interface. This remarkably means that our 2DEGs seem superconducting at lower temperature. The zero resistivity of the interface could not be observed due to the limitation of the transport instrument, i.e. the temperature range limit of the PPMS cryostat (minimum T = 1.65 K in best case). We have confirmed the reproducibility of the observed superconducting onset transition below 4 K in multiple KTO/LTO interface samples. Further investigation into the superconductivity of our 2DEGs is essential. Therefore, we plan to re-measure this sample, grow additional samples, and perform measurements using an alternative instrument capable of operating in the milli-Kelvin temperature range, specifically the Bluefors system.

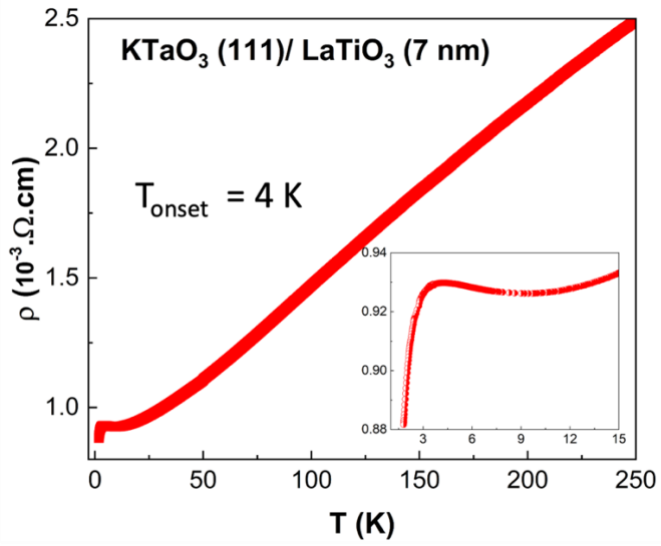

Figure 3. 22. Temperature dependence of electrical resistivity of KTO (111)/$LaTiO_3$ sample.

3.4. **Conclusions**

In this chapter we thoroughly discussed and provided the experimental procedures and growth conditions of the $LaTiO_3$ thin films along various single crystal substrates. Using the state- of – art molecular beam epitaxy we demonstrated the optimum substrate temperature, Ozone pressure and thickness for the growth of KTO/LTO with highest possible quality. XRD, AFM, Phi-scans, XRR, RHEED, LEED STEM showed the growth of very high-quality

KTO/LTO interfaces and provided clear evidence for the layer by layer, single phase epitaxial growth of $LaTiO_3$ along $KTaO_3$ single crystal substrates. Electrical transport measurements were used to elucidate the electronic properties of the grown KTO/LTO heterointerfaces, using the Hall effect and Van Der Pauw geometry, we measured the temperature and magnetic field dependence of longitudinal and transverse electrical resistance of the ultra- thin films. We used these results to calculate the sheet carrier density and electron mobility of our interfaces. The electrical transport measurements provided clear evidence of the formation of two-dimensional electron gases at the (110) and (111)- oriented KTO/LTO interfaces. The structural correlations showed the presence of epitaxial strain and interface disorder which most probably is an indication of the TiO_6 titling at the KTO/LTO interface. Remarkably, our KTO (111)/LTO (7 nm) sample showed a drop of the resistivity at an onset transition temperature of ~ 4 K, this is a very significant indication of the high possibility of the formation of a superconducting 2DEGs below 2 K, with a high electron mobility.

4. Coexistence of superconductivity and ferromagnetism in two dimensions

The coexistence of ferromagnetism and conventional superconductivity is rare due to the conflict between the anti-parallel spin arrangement within a Cooper pair and the parallel spin alignment in typical ferromagnets. Here we show that both superconductivity and ferromagnetism exist within high mobility, two-dimensional electron gases (2DEG) formed at the interface between (110) and (111) oriented surfaces of the nonmagnetic band insulator $KTaO_3$ (KTO) and thin overlayers of the antiferromagnetic Mott insulator $LaTiO_3$ (LTO). For the thinnest LTO overlayers strong evidence for ferromagnetism is found from square hysteresis loops of anomalous Hall effect (AHE) and out of plane magnetization with similar coercive fields. The magnitude of the AHE and a butterfly shaped magnetoresistance decreases with increasing LTO thickness and gives rise to superconductivity. For KTO (111)/LTO the superconducting transition temperature reaches as high as ~1 K for intermediate LTO thicknesses (~7 nm) and then decreases to zero for thicker layers. The competition between ferromagnetism and superconductivity may indicate unconventional superconductivity in 2DEGs formed at (110) and (111) KTO/LTO interfaces.

4.1. Introduction

Over the past two decades, there has been extensive research on 2DEGs that are formed at the interfaces between $SrTiO_3$ (STO) and several insulating oxide overlayers such as $LaAlO_3$ (LAO) [11,25] and $GdTiO_3$ [24]. The origin of the 2DEG is considered to be either intrinsic, from charge transfer, or extrinsic, from oxygen or other defects. These 2DEGs exhibit many interesting properties including ferromagnetism [58-63], superconductivity at transition temperatures (T_c) of up to 250 mK [27,30,64,65], and, more interestingly, the coexistence of superconductivity and ferromagnetism below 120 mK [39,40,66]. However, the ferromagnetic 2DEGs in STO/LAO have low electron mobilities (~1 $cm^2/V.s$ below 3 K) [59], and the superconductivity is limited to very low temperatures ~ 80-120 mK when the ferromagnetic order is present [39]. Recently, 2DEGs formed at the KTO (100) [41,67,68] surface, using EuO, $EuTiO_3$ and $LaTiO_3$ (LTO) overlayers, show high-mobility, as well as ferromagnetism [69,70]. Moreover, superconductivity up to temperatures as high as ~2.2 K has been observed in KTO (110) and KTO (111) based 2DEGs [43,45,47,53,71]. Thereby, KTO (110) and KTO (111) 2DEGs host superconductivity but lack ferromagnetism, whereas KTO (100) exhibits the opposite behavior [45,53,71]. Bulk $KTaO_3$ is a non-magnetic, band insulator, polar material with a cubic structure [72,73], while bulk $LaTiO_3$ is a Mott insulator characterized by a G-type antiferromagnetic order with a Néel temperature (T_N) ~120-146 K [74-78]. KTO has notably been reported to exhibit exceptionally strong spin-orbit coupling, exceeding that of $SrTiO_3$-based 2DEGs by more than an order of magnitude [51].

4.2. Experimental methods (Growth details)

$KTaO_3$ (111) / $LaTiO_3$ and $KTaO_3$ (110)/ $LaTiO_3$ heterostructures were grown by oxide molecular beam epitaxy (MBE) using a VEECO GEN-10 advanced deposition system. The $KTaO_3$ (KTO) substrates (5x5 mm^2) (purchased from MTI) are chemically pre-cleaned using a sequence of acetone, methanol, and iso-propanol, each for 5 mins and dried with nitrogen. Then the substrates are outgassed in the load lock chamber at ~ 4 x 10^{-8} Torr at 200 °C before inserting them into the main growth chamber, where they are heated at 820 °C in the presence of ozone for 10 mins. The base pressure of the MBE chamber is below ~1 x 10^{-10} Torr before

growth. The $LaTiO_3$ (LTO) layers are grown at a substrate temperature of 800 °C, in an ozone pressure of 8 x 10^{-8} Torr using La and Ti Knudsen-cells that are held at temperatures of 1305 °C and 1260 °C, respectively. The deposition rate and preliminary estimation of the elements ratio of the La and Ti sources was determined using an in-situ quartz crystal monitor (QCM). The growth rate of LTO is estimated to be ~ 0.2 nm/min. After the growth, the samples are then cooled to 700 °C in the presence of ozone gas (8 x 10^{-8} Torr) and subsequently cooled down to room temperature in vacuum.

4.3. **Results**

Here we present the first observation of ferromagnetism in 2DEGs formed at (110) and (111) oriented KTO/LTO interfaces. Remarkably, we find evidence for ferromagnetism and superconductivity in both cases and, in one case, at a temperature one order of magnitude higher than in STO/LAO interfaces. Interestingly, we find that the ferromagnetic order is observed for the thinnest LTO layers but that this order gives way to superconductivity at higher LTO thicknesses and then is suppressed for even higher LTO thicknesses.

LTO layers were grown epitaxially on (110) and (111) oriented KTO single crystalline substrate using molecular beam epitaxy (MBE) (see supplemental materials for details). Schematic models of the (110) and (111) KTO/LTO interfaces are shown in Fig. 4.1(a). In previous work it was shown that the LTO thin layers have a pseudo-cubic structure [53]. In our case, indeed, the LTO layers have lattice constants that are very close to that of the KTO substrate (3.989 Å) [79]. X-ray diffraction (XRD) $\boldsymbol{\theta - 2\theta}$ scans and reflection high energy electron diffraction (RHEED) for various thicknesses of the LTO layers grown on KTO (111) and (110) indicate their single-phase and epitaxial crystalline growth (see Fig. 4.1(b)). The LTO films exhibit an in-plane tensile strain which decreases with increasing t_{LTO}. The epitaxial growth of the LTO is confirmed by $\boldsymbol{\phi}$-scan measurements (see Fig. 3. 8(a, b)).

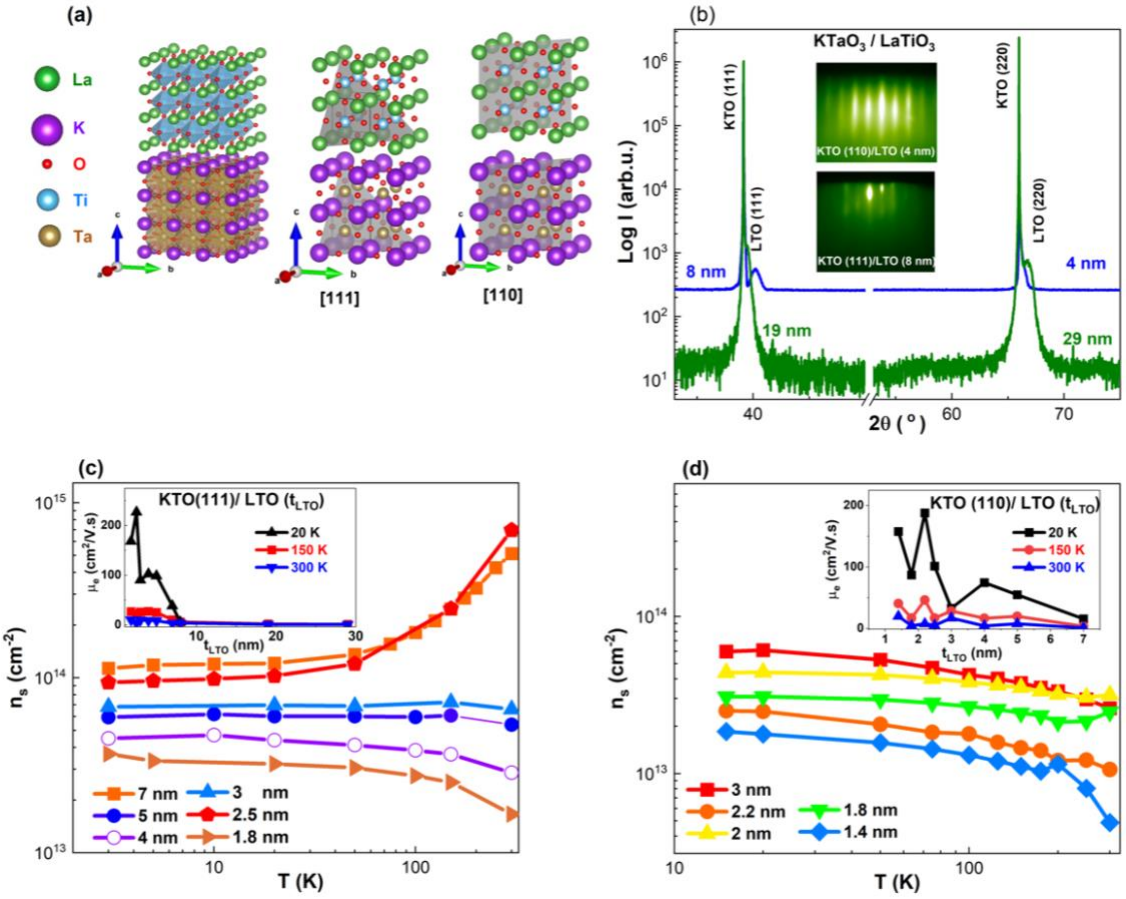

Figure 4. 1. Crystal structure and two-dimensional transport of $KTaO_3$/ $LaTiO_3$ interfaces. (a) Model of the crystal structure of the $KTaO_3$/ $LaTiO_3$ heterostructure grown along (001), (111)- and (110). (b) Symmetric θ-2θ x-ray diffraction patterns of LTO films grown on (111) and (110) oriented KTO. The inset shows the reflection high energy electron diffraction (RHEED) of the grown layers. Sheet carrier density as a function of temperature for the 2DEGs at the (c) $KTaO_3$ (111)/$LaTiO_3$, and (d) $KTaO_3$ (110)/$LaTiO_3$ interfaces, for various thicknesses of $LaTiO_3$. The insets show the electron mobility as function of $LaTiO_3$ layer thickness at different temperatures.

The temperature dependence of the sheet resistance (R_s) for both the (111)- and (110)-oriented 2DEGs indicates a metallic behavior for all t_{LTO} (Fig. 3. 16). At a given temperature R_s shows a non-monotonic dependence on t_{LTO} (Fig. 3. 19 (a, b)). The dependence of R_s on an external magnetic field whose direction is varied from out of plane (OOP) to in-plane (IP)

shows a characteristic two-fold pattern reflecting the 2D nature of the 2DEG for both (111)- and (110)- 2DEGs [69] (Fig. 3. 19 (c)). The sheet carrier density n_s is extracted from Hall measurements (Fig. 4. 1c, Fig. 4. 1d), thereby allowing the mobility to be determined. Electron mobilities at 2K as high as $\mu \sim 240$ and ~ 210 $cm^2/V.s$ are found for the (111) and (110) interfaces, respectively (see Fig. 3.17 and Fig. 3. 18). These results are similar to those reported for KTO (100)/LTO [41]. Exemplary in-plane longitudinal magnetoresistance (MR) curves for (111)- and (110) KTO/LTO for t_{LTO} =3 nm at 2K display a butterfly hysteretic behavior (see Fig. 4. 2a) which is generally understood to be indicative of magnetic ordering in other 2DEGs [39,58,59]. The magnitude of the MR for KTO (111)/LTO is significantly larger than for KTO (110)/LTO. Fig. 4. 2b illustrates butterfly shaped MR curves for thicker (111) LTO films grown on KTO (111): for which the MR is smaller.

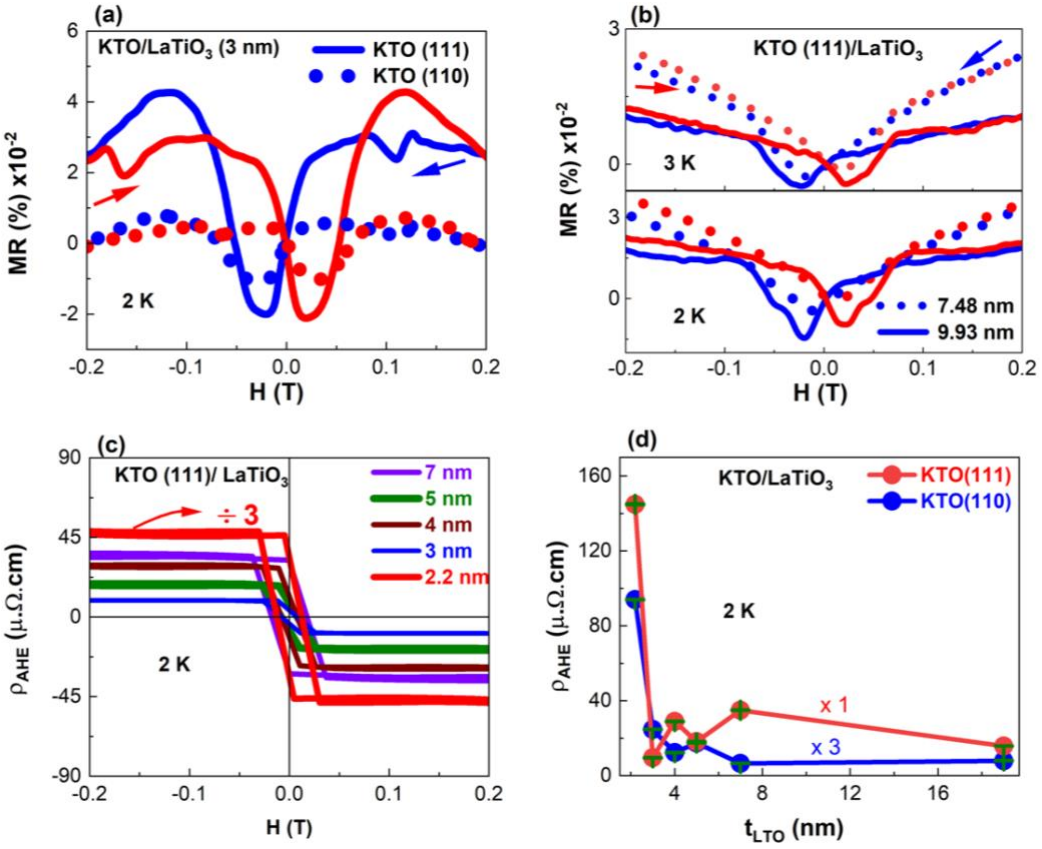

Figure 4. 2. Ferromagnetism of 2DEGs at KTO/LTO interfaces. Longitudinal magnetoresistance of KTO (111) /LTO and KTO (110)/LTO interfaces as a function of magnetic field applied parallel to the sample plane at 2K for (a) KTO/ LTO (3nm), (b) KTO

(111)/LTO with t_{LTO} = 7.48 nm and 9.93 nm, the magnetic field sweeping directions are colored blue for down sweep and red for up sweep. (c) Transverse Hall resistivity as a function of out of plane magnetic field at 2 K showing an anomalous Hall effect for KTO (111)/LTO at various t_{LTO}. The data for t_{LTO} = 2.2 nm is divided by 3 for better visualization. (d) Saturation anomalous Hall resistivity of KTO (111)/LTO and KTO (110)/LTO extracted from the hysteresis loops in (c). Note that a $KTaO_3/LaFeO_3/LaTiO_3$ control sample shows no anomalous hall effect (see Fig. 4.9).

The Hall resistance as a function of OOP magnetic field shows a hysteretic behavior consistent with an anomalous Hall effect (AHE) (see Fig. 4.2(c)) for data at 2K for KTO (111)/LTO for different t_{LTO}). In particular, the anomalous Hall resistivity, $\boldsymbol{\rho}_{AHE,}$ is finite in zero field and, moreover, switches sign depending on the sweep direction of the magnetic field. By subtracting a linear background and symmetrizing the curves (see SM, Fig. S4.7 and Fig.S4.8 for details) [80], the magnitude of the saturation value of ρ_{AHE} is plotted in Fig. 4. 2d, as a function of t_{LTO}. Note that ρ_{AHE} is significantly larger for KTO (111)/LTO than for KTO (110)/LTO which also matches the magnitude of the MR data for the two orientations (Fig. 4.2(a)). $\boldsymbol{\rho_{AHE}}$ exhibits the largest value for the smallest value of t_{LTO} and then generally decreases with increasing t_{LTO} (Fig. 4.2(d)), although non-monotonically. These data clearly suggest the presence of magnetic ordering of the 2DEG for both 111 and 110 orientations for thin LTO layers.

To determine the Curie temperature of the ferromagnetic transition of the KTO/LTO 2DEGs, we performed a set of various temperature dependence measurements. Fig. 4.3(a) shows the transverse hall resistance as a function of magnetic field of 0.5 T, at an out -of -plane applied magnetic field geometry. The Curie temperature is estimated to be at temperature below 45 K as shown in Fig. 4. 3a. The temperature dependence of the normalized magnetization as extracted from the M (H) hysteresis loops shows a similar transition temperature of the ferromagnetic order as shown in Fig. 4. 3b.

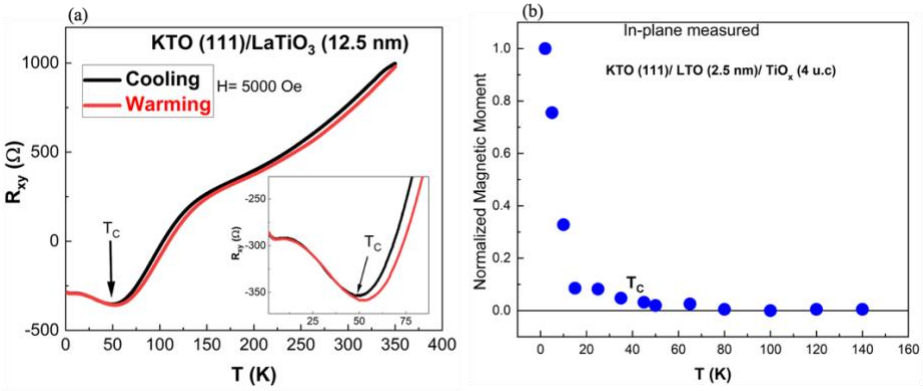

Figure 4. 3. Temperature dependence of the transverse electrical resistance, R_{xy} as function of temperature for KTO (111)/$LaTiO_3$ (12 .5 nm) sample measured within an out- of -plane magnetic field configuration. (b) Temperature dependence of the normalized magnetic moment for KTO (111)/$LaTiO_3$ (2.5 nm) sample.

The behavior of hysteresis loops of anomalous hall effect for KTO (111)/LTO (2. 2nm) sample is shown in Fig. 4. 4(a), while the temperature dependence of the anomalous hall resistivity $\boldsymbol{\rho_{AHE}}$ is shown in Fig. 4.4(b). Interestingly, the temperature dependence of the anomalous hall effect hysteresis loops shows a similar Curie transition temperature which matches with the measurement performed in Fig. 4. 3(a, b).

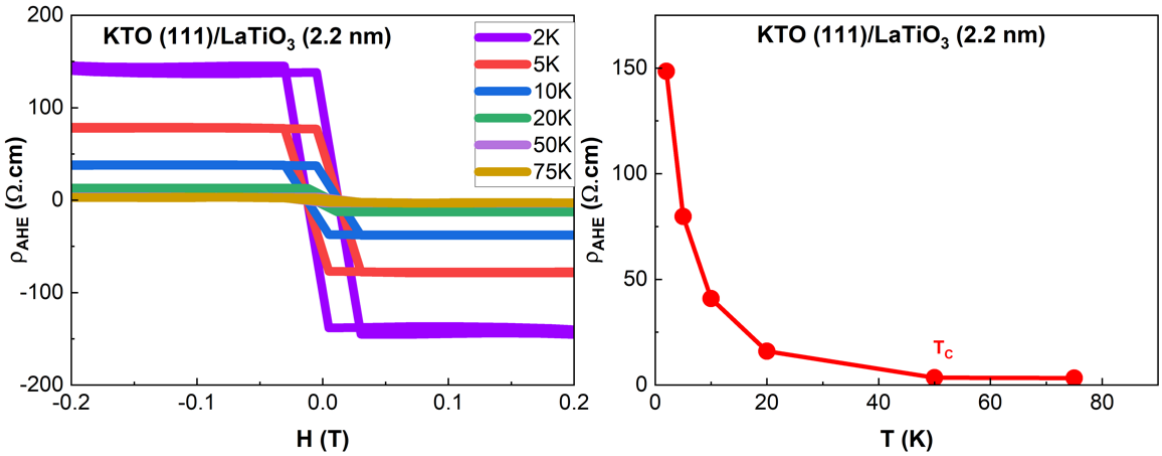

Figure 4. 4. (a) Magnetic field dependence of the anomalous hall resistivity hysteresis loops for KTO (111)/$LaTiO_3$ (2.2 nm) sample measured at various temperatures from 2 K to 75 K. (b) Temperature dependence of the anomalous hall resistivity for the same sample.

Clear evidence for superconductivity is found from resistance versus temperature measurements. Fig. 4. 5(a) shows the temperature dependence of the electrical resistance R(T) of two samples (KTO (111)/LTO (7 nm) and KTO (111)/LTO (5.77 nm)). Both samples show drops in resistance to zero at superconducting transition temperatures (T_c) of ~ 1 K and ~ 0.7 K, respectively. This same sample (7 nm) exhibits evidence for magnetism as evidenced by a butterfly hysteretic MR loop (see inset to Fig. 4. 5(a)) at temperatures just above T_c.

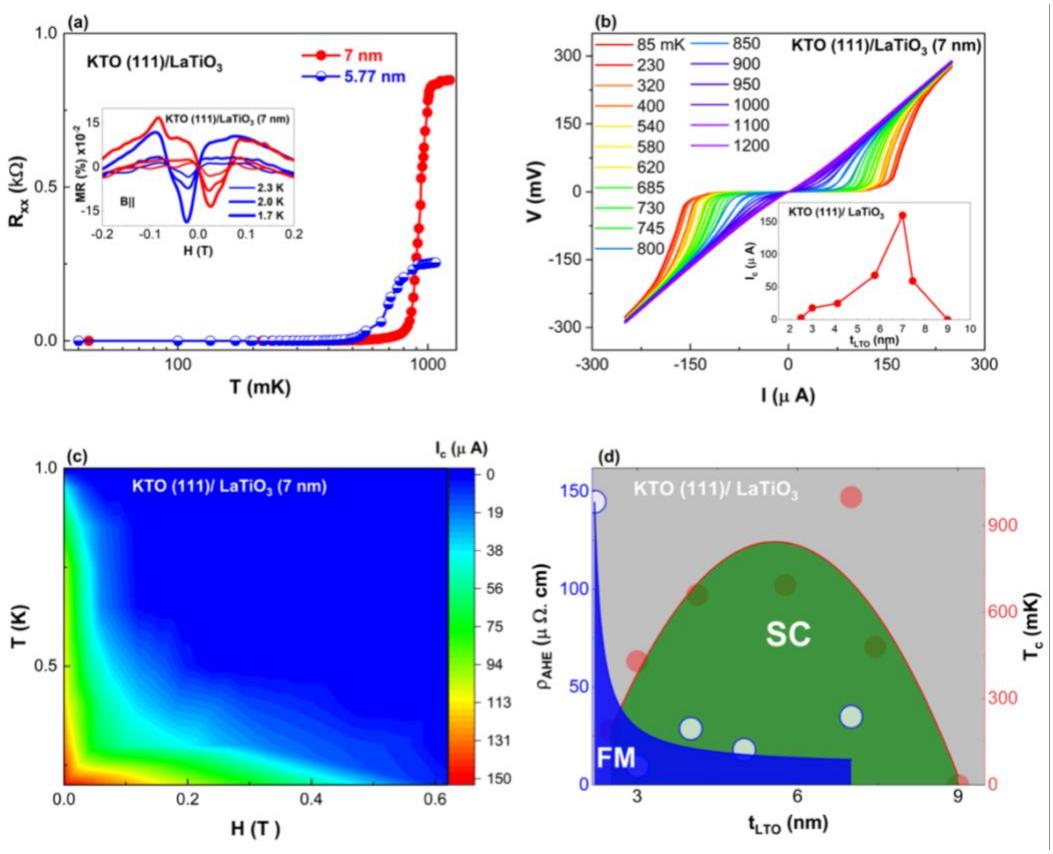

Figure 4. 5. Superconductivity at KTO (111)/LTO (t_{LTO}) interfaces. (a) Temperature dependence of resistance for t_{LTO} = 5.77 nm and 7 nm. The inset depicts the butterfly longitudinal magnetoresistance as function of magnetic field applied parallel to the sample plane at various temperatures for the t_{LTO} = 7 nm sample. Blue and red colors correspond to the sweeping direction of the magnetic field. (b) V(I) curves at various temperatures below and above Tc for t_{LTO} = 7 nm in zero applied field. The inset shows the variation of I_c as function

of t_{LTO}. (c) T-H phase diagram of I_c for t_{LTO} =7 nm. (d) Variation of T_c (I =25 μA) and $\boldsymbol{\rho_{AHE}}$ (at 2 K) as a function of t_{LTO}.

The magnitude of the critical current above which superconductivity is suppressed (I_c) was not reported in previous work on related samples [53]. The voltage vs current curves V(I) as a function of temperature are illustrated in Fig. 4.5(b) for the exemplary case of KTO (111)/LTO (t_{LTO} = 7 nm). The supercurrent, I_c, reaches a value of 150 μA at 70 mK for a sample 2.2 mm wide. Above 1 K the V (I) curves are linear (see Fig. 4. (5b)) indicating a metallic behavior consistent with the R (T) data (measured with I= 25 μA). The superconductivity is suppressed above a critical OOP magnetic field of ~ 0.60 T at 200 mK (I = 25 μA) which is one order of magnitude larger than that of STO-based 2DEGs (~0.06 T at 20 mK)[39]. The H-T phase diagram for I_c for ferromagnetic KTO (111)/LTO (7 nm) sample is depicted in Fig. 4. 5c. Note that these measurements were limited to T>200 mK, in which the current was swept up to 200 μA in the presence of an applied magnetic field. The variation of T_c and I_c with t_{LTO} reveals that there is a critical value of t_{LTO} at which T_c takes a maximum value and beyond which it rapidly decreases showing a non-monotonic behavior, as shown in the inset to Fig. 4. 5b and in Fig. 4. 5(d). The T_c phase diagram as a function of t_{LTO} exhibits a superconducting dome-like structure, reminiscent of the dome-shaped structure observed in cuprates superconductors as a function of hole doping (Fig. 3(d)). Interestingly, all the 2DEGs that show superconductivity also display evidence for magnetic order (see Fig. 4. 2 and Fig. 4. 5(d)). The x-ray absorption spectra (XAS) performed at the Ti- $L_{2,3}$ edge of (110) – and (111) – oriented KTO/ LTO (2.5 nm) is shown in Fig. 4. 6(a), measured at temperature of 2 K and at an in - plane applied magnetic field of 6 T.

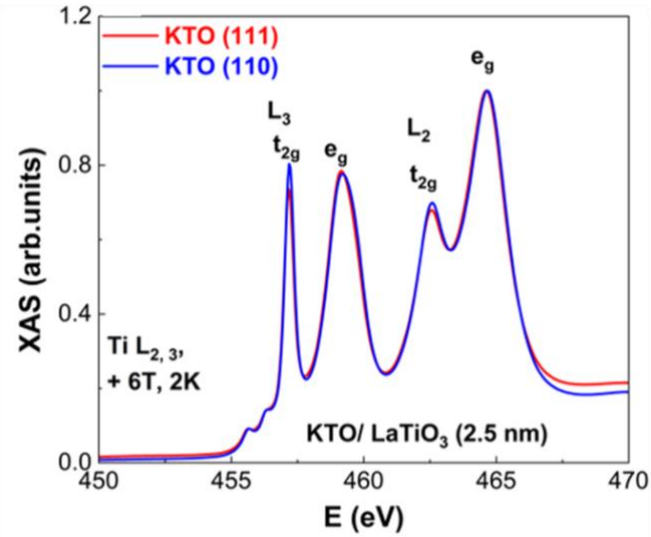

Figure 4.6. X-ray spectra at Ti- $L_{2,3}$ edge for KTO (111)/$LaTiO_3$ and KTO (110)/$LaTiO_3$ (2.5 nm) samples.

The out-of-plane magnetic field dependence of the magnetic moment M (H) in a KTO (111)/LTO (2.5 nm) sample was measured at 2K using SQUID magnetometry as shown in Fig. 4. 7(a). After a linear background subtraction (the substrate shows a diamagnetic contribution, as shown in Fig. S4.3) the M(H) loop shows a distinctive square shaped loop with a low coercive field of ~0.02 T which matches the anomalous Hall hysteresis loop. This feature is observed at temperatures up to 10 K (see Fig. S4.5). In addition, there is a larger magnetic contribution to the M(H) loop that varies little with temperature up to 80 K, suggesting that there are two sources of ferromagnetism in our KTO/LTO 2DEGs. The fact that the AHE signal only reflects the distinctive square shaped loop in the M(H) curves indicates that the second source of ferromagnetism arises from the insulating part of the LTO layers or the KTO substrate [80].

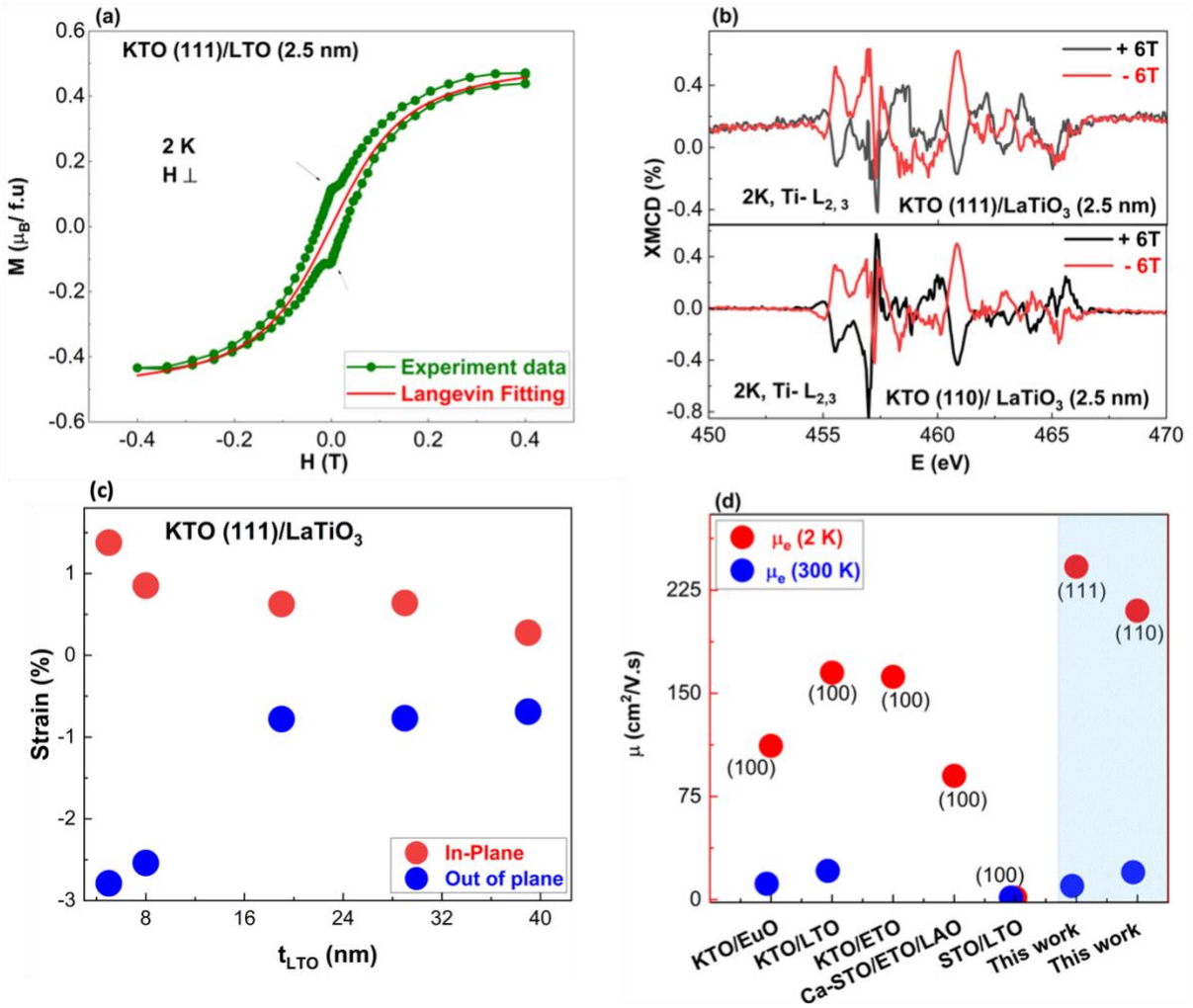

Figure 4. 7. Evidence for magnetism at KTO/LTO interfaces. (a) Magnetization versus out of plane magnetic field hysteresis loop for KTO (111)/$LaTiO_3$ (2.5 nm) at 2 K. (b) Ti-$L_{2,3}$ XMCD signal of (top) $KTaO_3$ (111)/$LaTiO_3$ (2.5 nm) and (bottom) $KTaO_3$ (110)/$LaTiO_3$ (2.5 nm) obtained from XAS spectra measured at in-plane fields of +6 T and –6 T, as shown in Fig. 4. 6). (c) In-plane and out-of-plane strain, expressed as the lattice mismatch percentage $(\frac{a_{film} - a_{substrate}}{a_{substrate}})\ \boldsymbol{x}\ \mathbf{100}$, for KTO (111)/LTO as a function of LTO thickness. (d) Comparison of the electron mobility measured here (right side highlighted in blue) with previous measurements for ferromagnetic 2DEGs (left side)[59,60,69,70].

In order to investigate the origin of the magnetism emerging at the KTO/LTO interfaces, we carried out x-ray magnetic circular dichroism (XMCD) measurements [81] (see

SM for methods details). XMCD measurements were performed at the Ti-$L_{2,3}$ edges since Ti have been reported to be the origin of magnetism in other oxide 2DEGs [60-62]. X-ray absorption spectroscopy (XAS) data were collected for both left- and right-handed circular polarization of the incident x-ray beam in in-plane magnetic fields of +6T and -6T for two samples with the same LTO thickness (2.5 nm) on KTO (111) and KTO (110) as shown in Fig. 4.6. The peaks in the XAS spectra correspond to the Ti L_3 and L_2 edges (see Fig. 4.6) and are in good agreement with those reported for STO/$LaTiO_3$ [82]. The resulting XMCD signals obtained from the XAS spectra at +6 T and -6T are nearly mirror images of one another (Fig. 4.7(b)), consistent with a field induced magnetic signal. However, it is well known that it is very difficult to extract a reliable value of the Ti magnetic moment from these data due to the small spin-orbit splitting [23,60]. Nevertheless, the XMCD data provides very good evidence of ferromagnetism in KTO/LTO from Ti moments.

Previously it has been reported that epitaxial strain induces a ferromagnetic signal in thin films of the bulk antiferromagnetic $LuMnO_3$ [83,84]. Thus, we examined possible structural origins of the magnetism in our KTO/LTO samples, focusing on the epitaxial strain of the LTO layer. Both in-plane and out-of-plane strains were observed, with a large out-of-plane compressive strain of (~ -3%) for t_{LTO} below ~ 10 nm, whereas the in-plane strain is tensile and much smaller (see Fig. 4. 7(c)). Whilst this strain may play a role in inducing the ferromagnetic order at the interface there is only a weak correlation with the thickness dependence of the magnitude of $\boldsymbol{\rho_{AHE}}$ (Fig. 4.2(d)). We do note that, given the close matching of the KTO and LTO lattice constants in the bulk, the origin of the strain we observe in the LTO overlayers likely derives from the significant tilting of the TiO_6 octahedra observed in bulk LTO (~26 degrees) and the absence of such tilting in KTO. This mismatch in tilting likely accounts for the significant strain in thin LTO layers.

Fig. 4.7(d) compares the electron mobility values of our ferromagnetic 2DEGs with those previous reported for other ferromagnetic 2DEGs. This comparison shows that the mobility (~ 240 cm^2/ V.s) of the ferromagnetic 2DEGs we observe at the KTO (110)/LTO interfaces and in the superconducting ferromagnetic KTO (111)/LTO interfaces are higher than those reported earlier for ferromagnetic STO and KTO 2DEGs.

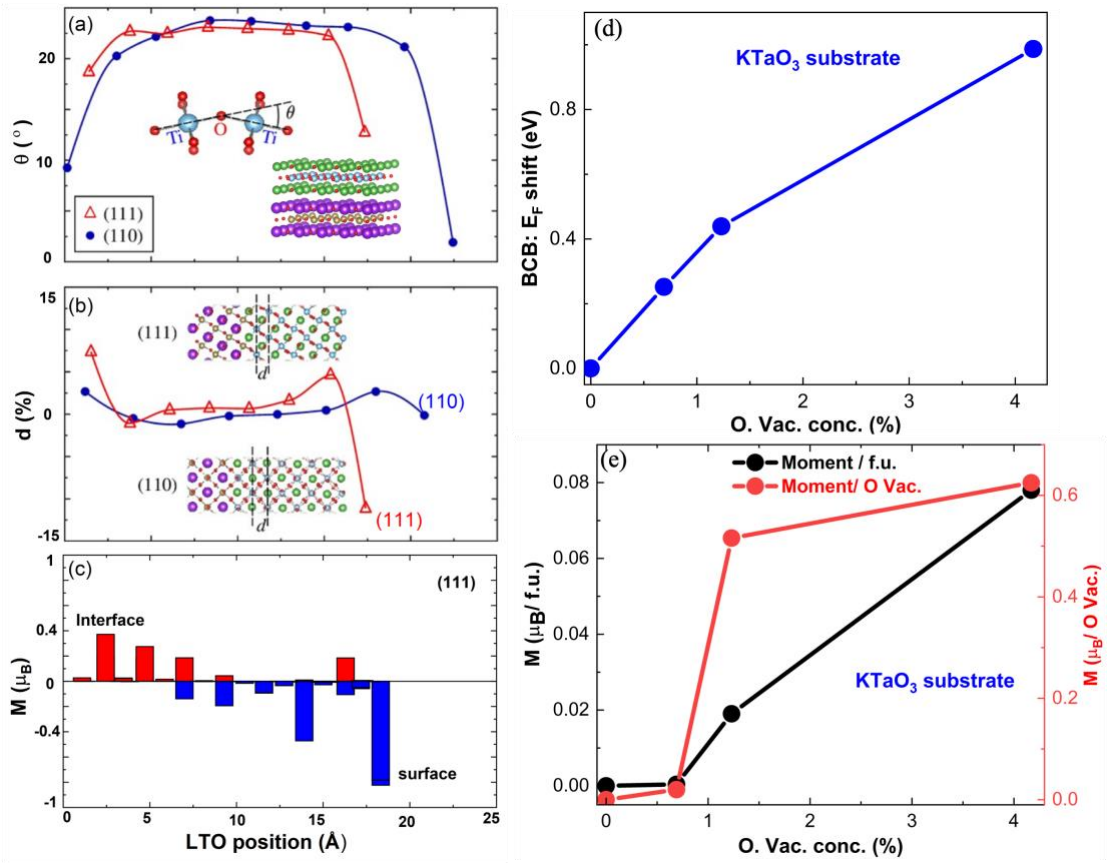

Figure 4. 8. Density functional theory calculations of (111) and (110) KTO/LTO (20 Ang.). Variation of (a) TiO_6-tilting angle, (b) interlayer relative distance, and (c) magnetic moment per Ti- atom, as a function of position within the LTO layer: zero corresponds to the KTO/LTO interface. Red and blue refer to the direction of the magnetic moment. Magnetic moment based on oxygen vacancy model at various vacancies concentrations created in $KTaO_3$ substrate (d) The bottom of conduction band shift relative to the Fermi level of $KTaO_3$ as function of oxygen vacancies at different concentrations (e) shows the calculated magnetic moment value per oxygen vacancy (in red) and per formula unit (in black) as a function of the oxygen vacancies.

To further understand the origin of the magnetism, density functional theory (DFT) calculations were carried out for KTO/LTO interfaces (see SM for details). In bulk LTO the TiO_6 octahedra are significantly tilted by an angle $\theta_{tilt} = 26°$. Previous DFT calculations have shown that when the tilting angle $\theta_{tilt} < 20°$ an insulator-to-metal transition takes place, and LTO becomes metallic, and, at an KTO/LTO interface, the tilt angle varies significantly with

distance from the interface, thereby, determining the thickness of the 2DEG [85]. In Fig. 4. 8(a), the calculated θ_{tilt} in an 8 f.u. (formula unit) thick LTO layer on KTO (111) and KTO (110) is plotted through the thickness of the LTO layer. The variation of the interlayer spacing within the LTO layers is shown in Fig. 4. 8(b). The tilting at the interface and surface of the LTO layer is significantly lower than in the interior, where the tilting angle is constant at ~24°, and, thus, both surfaces of the LTO layer are calculated to be metallic. In addition, the Ti magnetic moments at the interface are predicted to be ferromagnetically ordered with Ti moments of ~0.4 μ_B, (transitioning to a G- type antiferromagnetic ordering away from the interface), as shown in Fig. 4. 8(c) for KTO (111)/LTO. The LTO (111) surface layer also is calculated to exhibit ferromagnetism with Ti moments of ~0.8 μ_B, although these are oppositely aligned to those of the interfacial Ti moments.

These results give one possible explanation as to how ferromagnetism might evolve at the KTO/LTO interfaces from strain induced TiO_6-tilting. This behavior could indeed be consistent with the initial formation of a ferromagnetic interface layer with the subsequent compensation by a surface ferromagnetic layer. Then slight imbalances in these respective magnetic layer moments could account for the subsequent evolution of ρ_{AHE}. XRD investigations of the structure of the LTO layer could not resolve the TiO_6 tilting but rather showed very large Debye-Waller factors that could be consistent with tilting that could vary within the LTO layer (see Fig.3.10). Another possible explanation is that an interface ferromagnetic state arises from an interface induced canting of the antiferromagnetically ordered Ti moments, for example, through an interface Dzyaloshinskii-Moriya exchange interaction arising from the large spin-orbit coupling from Ta.

The interface magnetism was further explored in other structures, in which a thin $LaFeO_3$ (LFO) layer was inserted between a KTO (111) substrate and an LTO overlayer as shown in Fig. 4. 9. LFO and LTO have similar pseudo-cubic lattice constants and both exhibit G type AF, although the Néel temperature of LFO is much higher. We found evidence for a 2DEG in such structures but no evidence for an AHE. Thus, the AHE observed in KTO/LTO samples appears to be derived from an interface interaction.

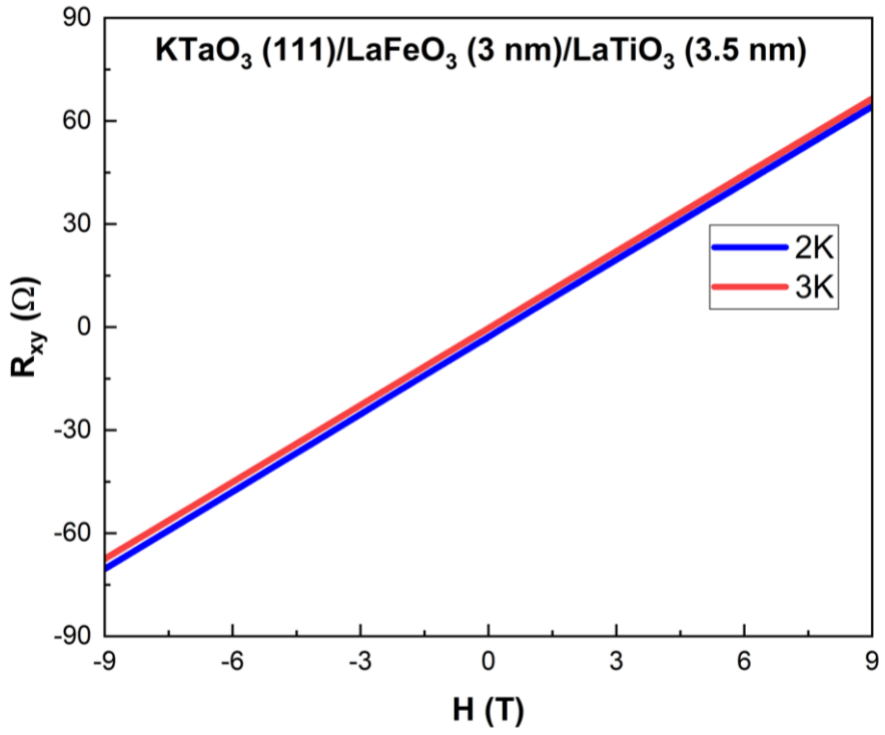

Figure 4. 9. Magnetic field dependence of the transverse resistance of $KTaO_3$ (111)/ $LaFeO_3$ (3 nm) $LaTiO_3$ (3.5 nm) sample measured at 2K and 3K, the absence of anomalous hall resistance confirms the interfacial induced ferromagnetism in KTO/LTO interfaces.

The second source of magnetism persists to much higher temperatures, as evidenced by out-of-plane M (H) hysteresis loops measured up to 80 K (Fig. S4.5). One possible explanation is from oxygen vacancies. Indeed, DFT calculations show that oxygen vacancies in KTO can give rise to magnetic moments of up to 0.06 μ_B per O vacancy (see Fig. 4. 8(d, e)) and it is well known that O vacancies in KTO can exhibit magnetic moments [80]. Tilting of the TiO_6 octahedra, mentioned above, (Fig. 4. 8 (a-c)), could also account for these moments.

The existence of both ferromagnetism and superconductivity at KTO/LTO interfaces in this study suggests one of two scenarios: either the two phenomena coexist, or they are in competition. Our results indicate that this behavior depends on the thickness of t_{LTO}; at certain t_{LTO} thicknesses, the two phenomena appear to weakly coexist, while at other thicknesses, they seem to compete.

The coexistence of superconductivity and ferromagnetism in KTO/LTO 2DEGs is highly interesting but we can only speculate on its origin. Firstly, it could be attributed to two distinct sets of electrons each responsible for one phenomenon, in the 2DEGs [39]. However, this scenario are unlikely, as we would expect similar observations in KTO (100)/LTO, where superconductivity is absent [53]. The second scenario, driven by interfacial induced ferromagnetism mediated by strong spin-orbit coupling at the interface at low temperature controlled by t_{LTO}, in addition to the O-titling and strain (see Fig. 4.8 and Fig. 4.7(c)). This scenario appears more plausible, especially given our findings. We observed that as the thickness of t_{LTO} decreases, strain increases, potentially correlating with the observed trend of enhanced ferromagnetism (AHE resistivity) as a function of t_{LTO}, as shown in Fig. 4.2, and superconductivity peaks at certain t_{LTO} while suppressed when $\boldsymbol{\rho_{AHE}}$is peaked at thinner t_{LTO} at the interface. This strain increase may also contribute to the suppression of superconductivity as the material nears the KTO interface, where a ferromagnetic ground state tends to dominate [69,83].

Finally, we should stress that superconductivity in this work seem to be strongly depending on the thickness of LTO layer. At very low LTO thickness, ferromagnetism and superconductivity appear to compete ferromagnetism reaches its maximum at the interface, while superconductivity is suppressed as shown form the phase diagram of KTO (111)/ LTO interfaces (Fig. 4.5). As the LTO thickness increases, ferromagnetism begins to minimze, and the superconducting transition temperature rises, peaking around a thickness of ~7 nm. In this thickness range, both phenomena appear to coexist weakly.

4.4. **Conclusions**

In summary, we observe ferromagnetism and superconductivity in 2DEGs formed at both (111) and (110) oriented $KTaO_3/LaTiO_3$ interfaces. In both cases we clearly show that a well-defined square magnetic hysteresis loop in the AHE for thin LTO layers matches a similar hysteresis loop in the out of plane magnetization curve and that, as the thickness of the LTO layer is increased, this magnetic component vanishes. Thus, we conclude that thin LTO layers give rise to a 2DEG that is ferromagnetic. For thicker LTO layers, the 2DEGs become

superconducting. We have carried out extensive measurements for the KTO (111)/LTO case. For this case, the T_c increases gradually from zero for the thinnest LTO layers to a maximum value of ~1 K for t_{LTO} ~ 7 nm and then decreases. Thus, the ferromagnetic and superconducting states appear to compete with one another. We note that a second source of ferromagnetism that persists to high temperatures is likely derived from the insulating components of the device structure likely from defects or from strain induced structural changes in the LTO layer. The competition between superconductivity and magnetism in the 2DEGS formed in KTO (111)/ and KTO (110)/LTO 2DEGs is novel and may indicate unconventional superconductivity.

4.5. Supporting materials (SM- 4)

4.5.1. Structural, magnetic and transport properties:

The elemental composition of the samples was probed using Rutherford Backscattering Spectroscopy (RBS) and x-ray photoelectron spectroscopy (XPS) measurements. Reflection high-energy electron diffraction (RHEED) was used to check the in-situ growth of the thin film layers. The surface topography and roughness of the samples was measured using atomic force microscopy (Bruker-Dimension AFM). The crystal structure of the sample was investigated by carrying out ($\boldsymbol{\theta - 2\theta}$) scans, XRR (X-ray reflectivity) and $\boldsymbol{\phi}$-scans using a high-resolution X-ray diffractometer (HR-XRD, D8-Bruker) equipped with a Cu- K alpha source ($\boldsymbol{\lambda}$= 1.5418 Å) and 2D detector.

4.5.2. Strain measurement

We have measured the strain via performing high-resolution x-ray diffraction measurement (HR-XRD) using Bruker-D8 diffractometer at symmetric reflection peaks as well as asymmetric reflection peaks of the KTO substrate to determine the out of plan and in-plane lattice mismatch, respectively. Additionally, the reciprocal space mapping (RSM) measurement using HR-XRD is also performed at (1 1 1) peak of the KTO (111)/LTO and at (110) peak for the KTO (110)/LTO interfaces.

The usual alignment procedures of the samples were performed (including, z-scan, rocking curve measurement, $\boldsymbol{\psi}$- scan at the strongest peak of the film followed by a $\boldsymbol{\phi}$- scan measurement). We select the highest intensity $\boldsymbol{\phi}$ - peak and we align the film accordingly for better resolution. Then, a ($2\boldsymbol{\theta - \omega}$) scan is performed on every sample, via which we determine the peak position of the $2\boldsymbol{\theta}$ angle from the diffraction pattern of the film. The mentioned steps are performed out-of-plane and in-plane to determine the lattice constants of the film at different thickness by selecting the appropriate symmetric and asymmetric reflection. This is achieved by selection of (h k l) peak reflections which are located in (out) - plane of the film/substrate depending on the substrate orientation either (110) or (111) oriented surfaces. In case of KTO (111)/$LaTiO_3$ interfaces, we performed the above-mentioned measurement steps at the (1 1 1) peak reflection of all samples for the determination of the out of plane (OOP)

lattice constants (or d-spacing) of the films at various thickness. For the determination of the in-plane lattice constants of $LaTiO_3$ films in KTO (111)/$LaTiO_3$, we performed the same alignments steps procedures then we transmitted the derive position values of the motors which correspond to the peak reflection of an asymmetric reflection peak (2 0 0) followed by ($\boldsymbol{2\theta - \omega}$) scan. The in -plan and OOP lattice constants of each film are then compared with the lattice constant (d-spacing) of the KTO substrate, which is fixed, then used for the calculation of lattice mismatch (difference between lattice constants of the film and substrate))

$$\text{Strain \%} = \frac{\mathbf{a_{film} - a_{substrate}}}{\mathbf{a_{susbtrate}}} \mathbf{x\ 100}$$

to determine the lattice mismatch ratio and strain percentage which is used as a direct indication of the present epitaxial strain at the KTO/$LaTiO_3$ samples.

The strain behaves in different directions in (111) and (110) oriented $KTaO_3$ interfaces due to the different polarity terminations, in $KTaO_3$ (111) the polarity termination is KO_3 and Ta [6], so the interface planes becomes (KO_3- Ta- LaO- TiO_2) [4], while as in case of $KTaO_3$ (110), the polarity termination is along KTaO and O_2 plane so the interface plane becomes (KTaO- O_2- LaO- TiO_2) [6]. This results in change of the bond length along different directions a or b or c in each orientation according to the termination type.

The magnetic properties were studied with a magnetic property measurement system (MPMS) Quantum Design SQUID magnetometer. Resistance and Hall effect measurements were performed in a Quantum Design Dynacol physical property measurement system (PPMS) using the van der Pauw method [86]. Contacts were bonded at the 4 corners of the 5x5 mm^2 samples using Al wire bonding. The sheet carrier densities were determined from the Hall data (from the slope of the high field data) and used to determine the carrier mobility using the measured sheet resistance.

The ultra-low temperature transport measurements were performed in a Bluefors dilution refrigerator with a base temperature of 20 mK and equipped with high frequency electronic filters. Direct current-voltage characteristics of the samples were measured using a Keithley 6221 current source and a Keithley 2182A nanovoltmeter. The samples measured in the BluFors were also bonded by Al-wire in a van-der Pauw geometry.

4.5.3. X-ray Absorption Spectroscopy (XAS) and X-ray Magnetic Circular Dichroism (XMCD) Measurements

The samples were measured at the BOREAS beamline (BL 29) at the ALBA synchrotron in Barcelona, Spain. All samples were measured in the total electron yield (TEY) mode under grazing incidence geometry of the x-ray beam (the angle between the x-ray beam and the sample's surface is set at 20 deg) at the Ti-$L_{2,3}$ edge with opposite beam helicities (left and right circular polarized) at a temperature of 2 K. The spectra were collected under an in-plane applied magnetic field of + 6 T and – 6 T, separately. The TEY spectra were recorded several times for both left and right-handed polarization in order to achieve good statistics by averaging. The value of the TEY just prior to the absorption edge is subtracted and the edge jump normalized to 1 after the edge. Finally, the XMCD is obtained from the difference between the normalized TEY intensity for left and right-circular polarized x-rays.

4.5.4. Structural characterization

The specular x-ray reflectivity (XRR) scan of KTO (111)/LTO (8 nm) and thick KTO (110)/LTO (29 nm) samples are shown in Fig. S4.1(a) and Fig. S4.1(b), respectively. These scans elucidate clear oscillations which indicates the flatness and uniformity of the film.

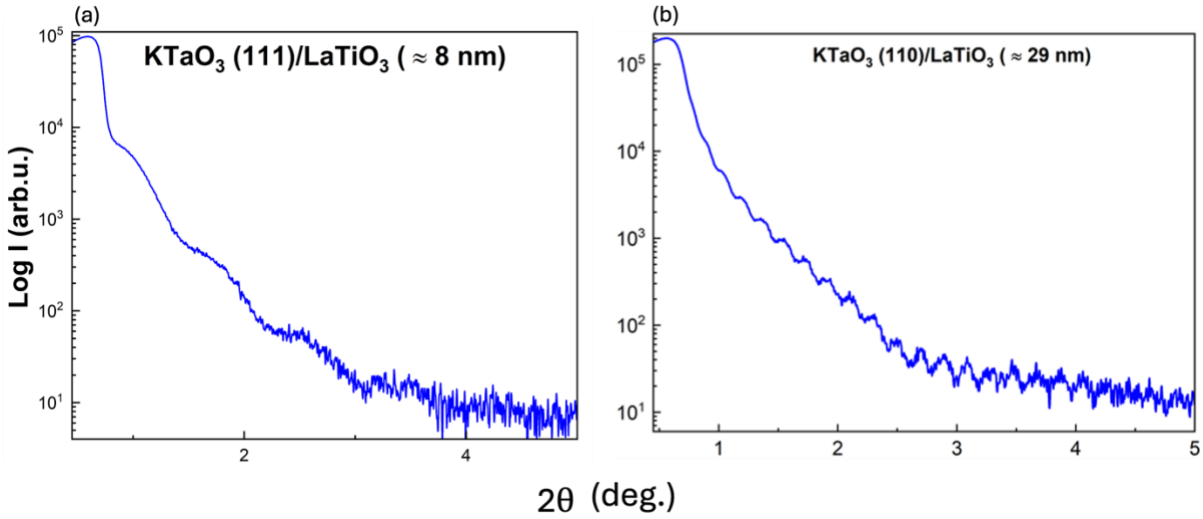

Figure S4. 1. X-ray reflectivity of: (a) KTO (111)/LTO (8 nm) sample, (b) KTO (110)/ LTO (29 nm) sample.

Electrical and magnetic transport data

To confirm the two-dimensional conductivity of the interfaces we made a measurement of the angular dependence of sheet resistance for various applied magnetic fields (AMR), as shown in Fig. S4.2. The AMR curves show a two-dip folded pattern which is consistent with the 2D conduction properties of the KTO/LTO interfaces.

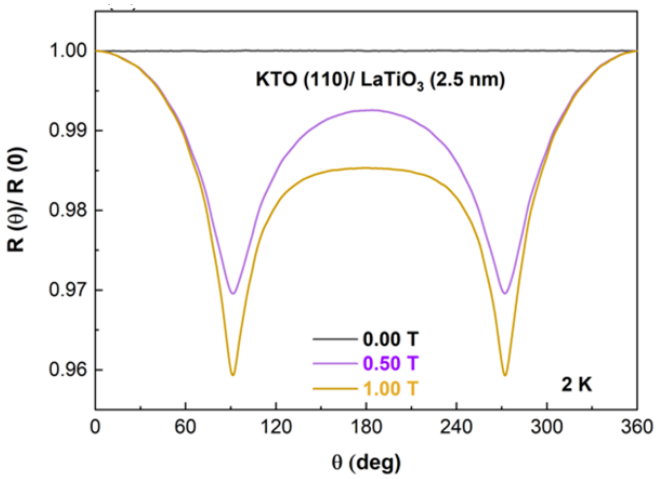

Figure S4. 2. Angular dependence of the normalized electrical resistance of KTO (110)/LTO (2.5 nm).

The magnetic field dependence of the magnetization of a KTO (111)/LTO (2.5 nm) sample, measured for an out- of plane magnetic field, is showed in Fig. S4.3. A ferromagnetic hysteresis loop at 2 K with a coercive field of ~ 0.05 T is found. It is worth noting that the square kink in the M (H) hysteresis loop in KTO (111)/LTO samples that occur at low field near 0.03 T, disappears above 10 K. The in-plane magnetic field dependence of magnetic moment for KTO (111)/$LaTiO_3$ samples is shown in Fig. S4.4, measured at 2 K for various thickness of LTO layers.

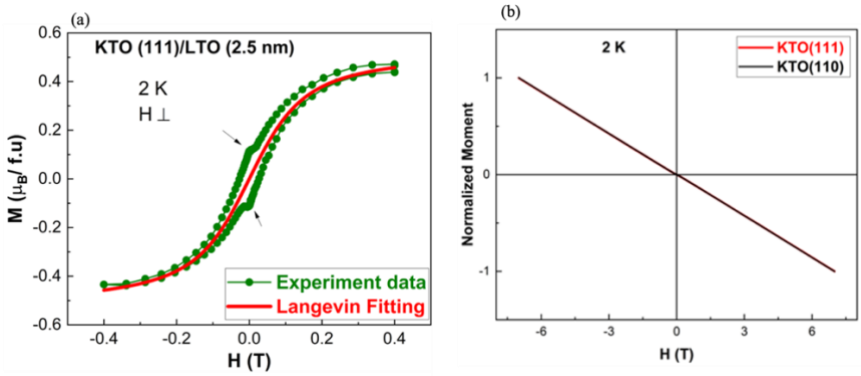

Figure S4. 3. Magnetization hysteresis loop as a function of out of plane magnetic field at 2 K for (a) KTO (111)/LTO (2.5 nm) sample, the linear interpolation of the as measured loop (in green) and the Langevin fitting of the same loop (red) to subtract the paramagnetic signals at high fields. (b) Out-of- plane normalized magnetic moment as function of magnetic field for $KTaO_3$ (110) and $KTaO_3$ (111) substrates at 2 K.

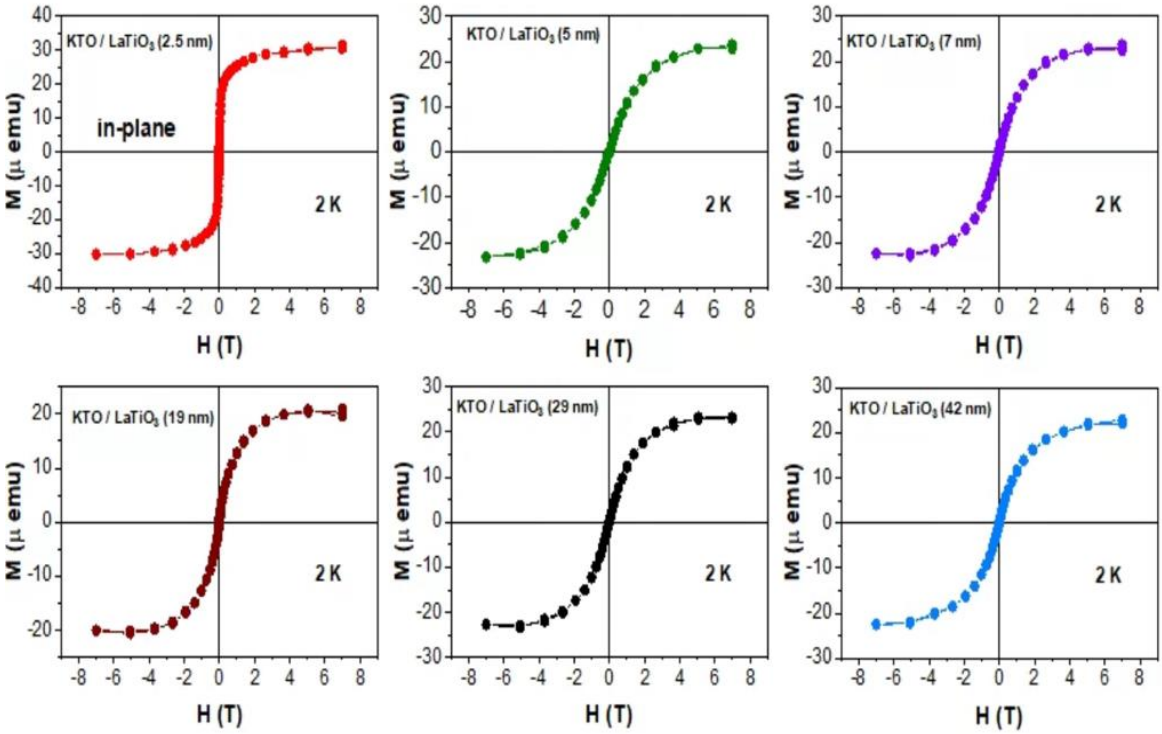

Figure S4. 4. In-plane magnetization hysteresis loops of KTO (111)/$LaTiO_3$ samples at various thickness of the t_{LTO} overlayer, measured at temperature of 2 K.

The out- of -plane magnetic field dependence of the magnetic moment behaviors for KTO (111) /$LaTiO_3$ at various temperatures from 2 K up to 80 K are shown in Fig. S4.5.

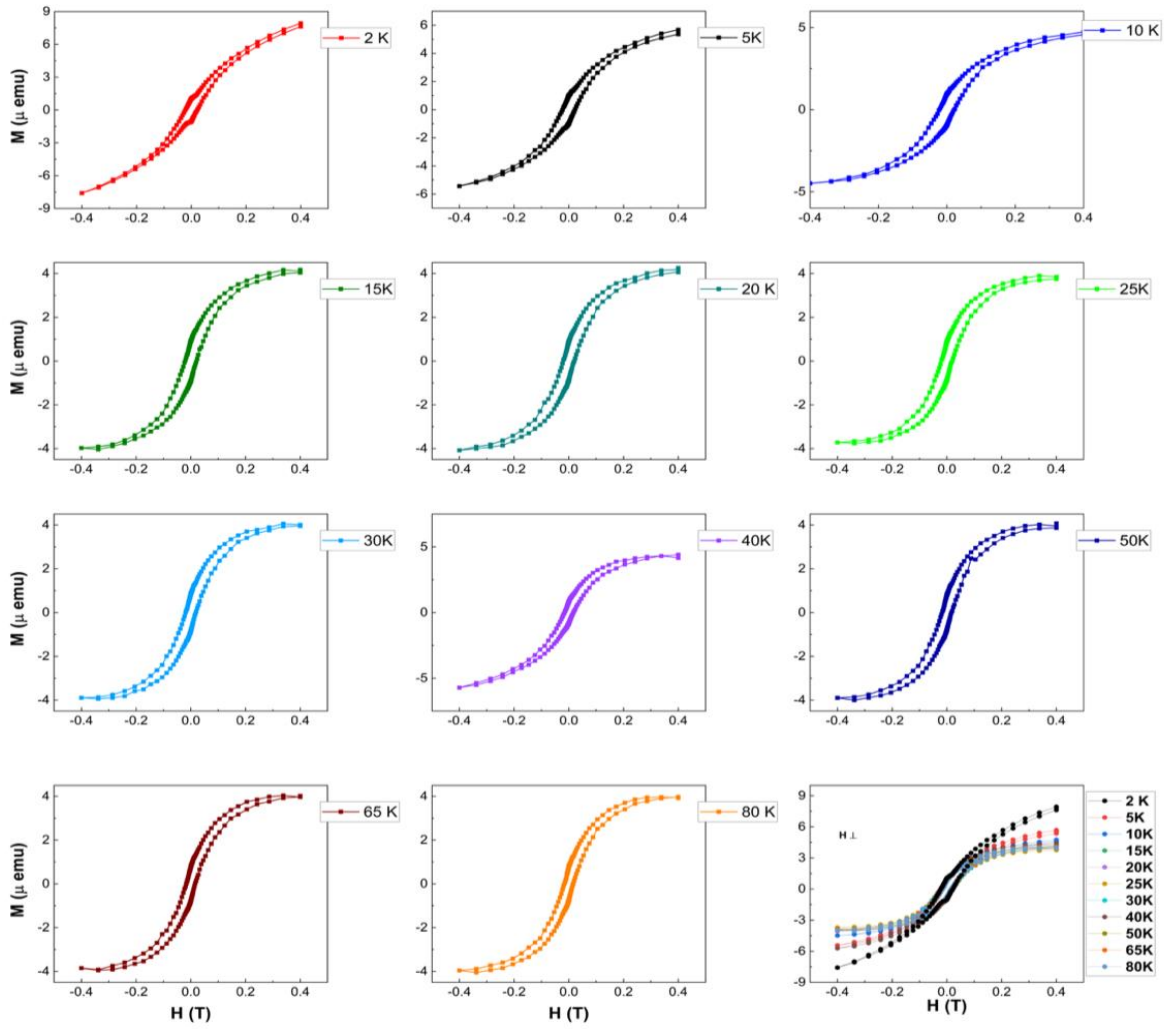

Figure S4.5. Magnetization M (H) hysteresis loops of KTO (111)/$LaTiO_3$ (2.5 nm) sample measured as function of temperature from 2 K to 80 K, below 15 K a small square kink near zero field is observed in the hysteresis loops.

Fig. S4.6 displays the out of plane magnetic field dependence of the transverse Hall resistance at 2 K for KTO (111) /LTO and KTO (110)/LTO samples showing a linear slope at higher fields. Fig. S4.7 depicts an exemplary sample, showing the data anti-symmetrizing procedure that was used to remove the ordinary Hall effect contribution to obtain only the anomalous Hall effect contribution at 2K.

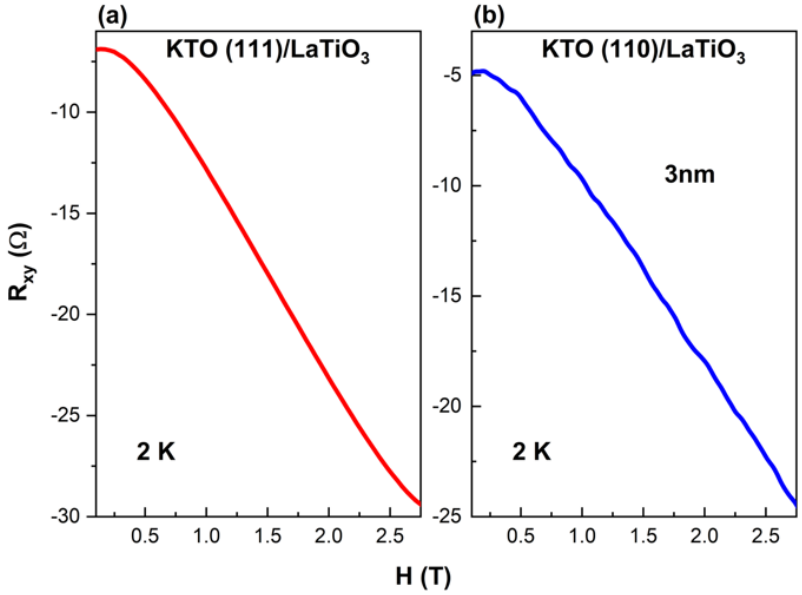

Figure S4. 6. (a) Transverse resistance R_{xy} versus out of plane magnetic field showing a linear behavior at high fields that is used for estimation of the sheet carrier density for (a) KTO (111) /LTO (3 nm) and (b) KTO (110)/ LTO (3 nm).

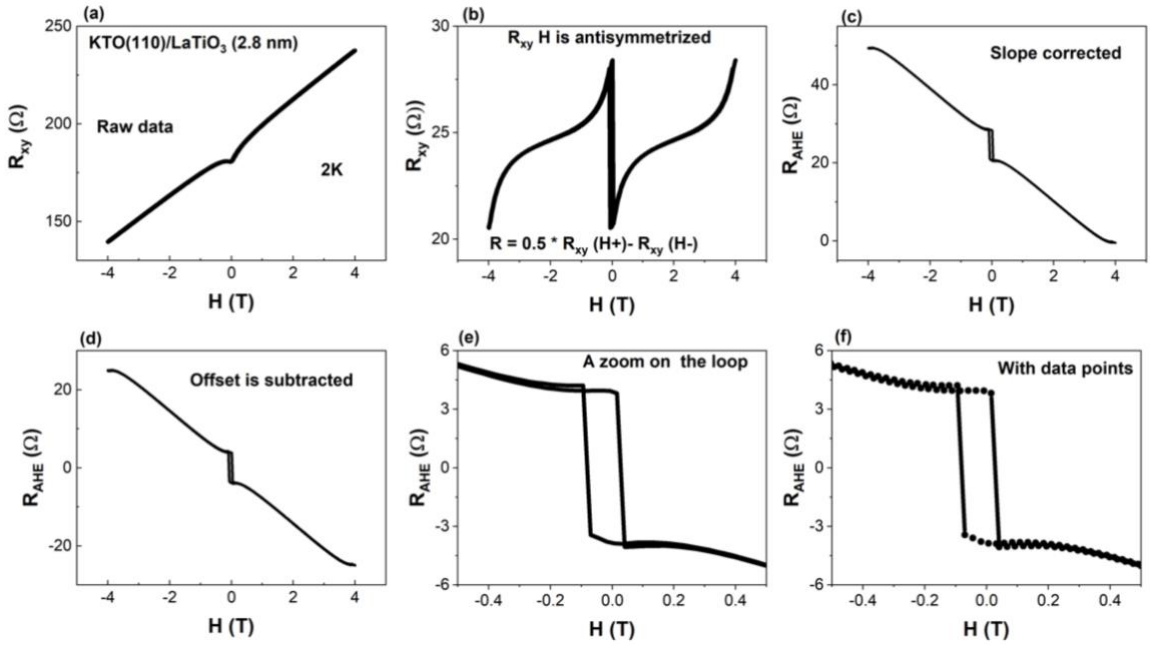

Figure S4. 7. The procedures that were used for anti- symmetrizing the transverse Hall resistance R_{xy} data. (a) As-measured R_{xy} (H) data. (b) Anti- symmetrized R_{xy} component as

obtained from $\boldsymbol{R} = \frac{\boldsymbol{R_{xy}(H_+)-R_{xy}(H_-)}}{\boldsymbol{2}}$. (c) Linear interpolation of the high field data is used for the slope correction. (d) The offset is removed by subtracting R - $\frac{(\boldsymbol{R_{max}}) + (\boldsymbol{R_{min}})}{\boldsymbol{2}}$. (e) Final result of the anomalous Hall effect hysteresis loop. (f) Same data as in (e) but showing the corrected data points.

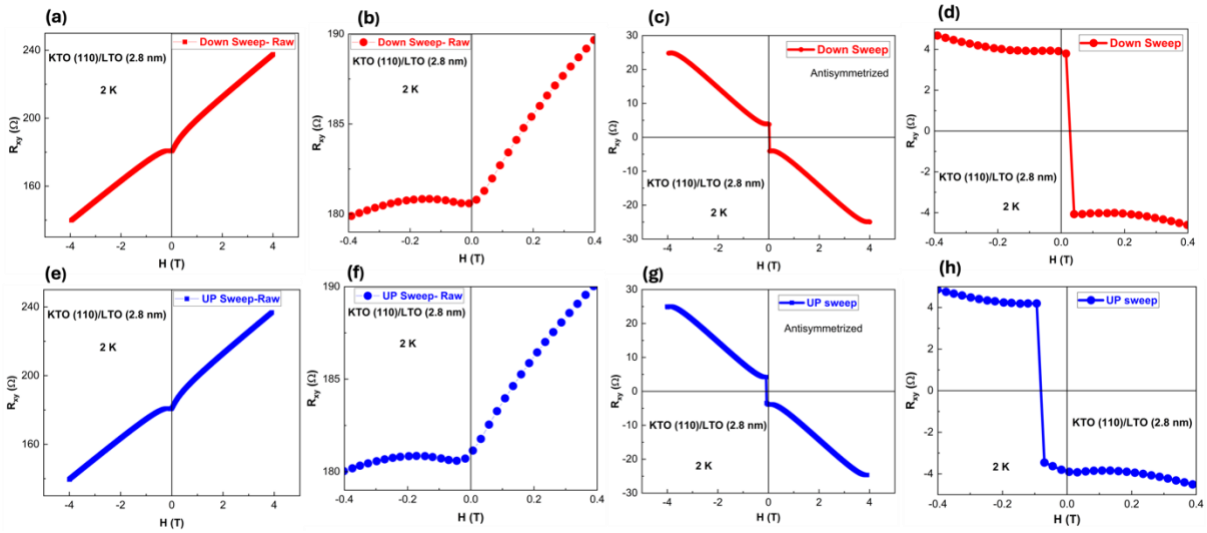

Figure S4. 8. Antisymmetrization procedures of the transverse R_{xy} component for each branch of both sweeping field (Down, Up) separately of an exemplary KTO (110)/$LaTiO_3$ (2.8 nm) sample measured by Van Der Pauw method, (a) Raw data representing R_{xy} vs. H measurement for down sweep of field direction, (b) A zoom on the raw data of (a), (c) The anti-symmetrized R_{xy} vs. H of the down sweep measurement, (d) A zoom on the plot of (c) for down sweep, (e) Raw data representing the R_{xy} vs. H measurement for up sweep of field direction, (f) A zoom on the raw data of up sweep of (a), (g) The anti- symmetrized R_{xy} vs. H of up sweep measurement, (h) A zoom on the raw data of down sweep shown in (g) , (the anti-symetrization details are described in the figure above).

We performed the anti-symmetrization procedures on each branch of the sweeping magnetic field (up) and (down) separately as shown here in Fig. S4.8. The I-V characteristic curve of one exemplary sample of KTO (110)/LTO measured at 150 mK is shown in Fig. S4.9, indicates the superconductivity at transition temperature lower than that of KTO (111)/LTO samples.

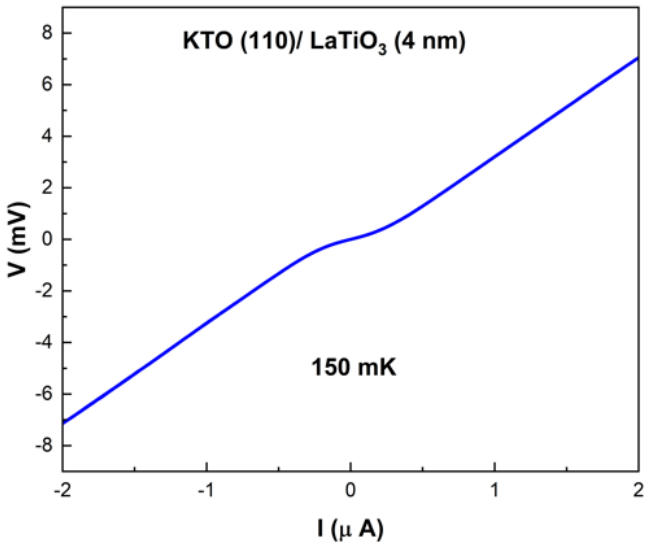

Figure S4. 9. V-I curve of a KTO (110)/LTO (4 nm) sample measured at ~ 150 mK, showing a very small critical current as compared to the critical current observed for KTO (111) /LTO (4 nm) samples with the same width (2.2 mm).

4.5.5. **Density functional theory (DFT):**

To understand the possible origin of observed ferromagnetism and uncover if it is interfacial induced, we performed density functional theory calculations. The DFT calculations were made with a slab geometry [1]. Bulk LTO is insulating and exhibits a large 0.5 eV Mott gap, yet the DFT calculations clearly show that thin layers of LTO on both KTO (110) and KTO (111) become metallic. In Fig. 4.8 (a), the TiO_6 tilting angles, θ, calculated in the 8-f.u.-thick LTO over layers on KTO (111) and KTO (110), are plotted as a function of the layer position outwards from the KTO/LTO interface. In orthorhombic LTO, the angle of optimally rotated TiO_6 octahedra, $\theta = 26^o$, represents the key structural factor which determines its energy band gap and the G-type antiferromagnetism. When the tilt angle goes below ~20^o the Ti–O bond length decreases, thereby giving rise to the insulator-to-metal transition [2]. The latter takes place, as shown in Fig. 4.8 (a), at both the (111) and (110) interfaces of KTO/LTO as

well as at the vacuum surfaces. Fig. 4.8 (b) shows the interlayer deformation in the 8-f.u.-thick LTO overlayers.

These structural deformations, which are obtained as the relative change of interlayer distance with respect to the bulk value, can be compared with our experimental data. In bulk LTO, the Ti -3d orbital filling corresponds to $t_{2g}^1 e_g^0$ and, according to our calculations, each Ti has a magnetic moment of about 0.7 μ_B. The four Ti atoms in the unit cell order antiferromagnetically with respect to each other according to a G-type structure that shows the lowest energy. The ferromagnetically ordered configuration of LTO, that is unfavorable energetically by 1.5 eV/f.u., results in a shrinkage of the bulk energy band gap to a nearly zero value of ~50 meV. Similar to other perovskite interfaces, the inversion symmetry which is broken at the KTO/LTO interface thereby lifts the 2DEG spectral degeneracy. Since, however, the crystal inversion symmetry is broken in bulk LTO this factor of reduced symmetry cannot critically affect the magnetic ordering of LTO, which is more sensitive to the TiO_6 octahedra tilting. As Fig.5c shows, the Ti magnetic moments within an interfacial layer of KTO/LTO (111) are ordered ferromagnetically to each other. Further from the interface, the Ti moments within each layer are ordered antiferromagnetically resembling their bulk configuration. Interestingly, at the LTO (111) surface layer we find that the Ti have a moment of 0.8 μ_B which are ordered ferromagnetically but in an opposite direction to that of the ferromagnetic interfacial Ti moments.

4.5.6. **Methods of DFT calculations**

Ab initio calculation of the 2DEG that emerges at the KTO / LTO interface was reported first for the (001) interface [41]. For this orientation each oxide is polar and, therefore, the polar discontinuity at the TaO_2/LaO interface could allow for the formation of a 2DEG. Recently, Maznichenko et al.[54], have simulated from first principles the (110) and (111) LTO/KTO interfaces, using a superlattice model. It has been shown that the 2DEG densities of all three interfaces are formed by the 3d- and 5d-states of interfacial Ti and Ta in the ratio 2:1. In the LTO/KTO (001) 2DEG, each Ti–Ta interfacial pair gives one electron while this amount increases from 1.24 electron up to 1.75 electron at the (110) and (111) interfaces, respectively[54]. A key reason is the" under tilting "of the TiO_6 octahedra within the LTO, as

compared to the bulk tilting angle. This" under tilting "seen near the interfaces destroys the small Mott band gap of LTO. At the (001) and (111) interfaces the mechanism of" under tilting "is complemented by the polarity-induced charge transfer making these two effects inseparable. As for the (110) interface, its 2DEG cannot be attributed to the polar discontinuity and, thus, the" under tilting "is critically important there. The relatively high density of states of the conducting electrons at the (110) and (111) interfaces may be a decisive factor in their becoming superconducting in contrast to LTO/KTO (001) which is metallic but not superconducting [53].

In this work, we simulate from first principles the (110) and (111) interfaces of LTO/KTO focusing on the magnetism of the LTO overlayers. The electronic properties and structural optimization of LTO/KTO were computed using the VASP code [87] within the Perdew-Burke-Ernzerhof generalized-gradient approximation [88] (GGA-PBE) to the exchange-correlation potential. The electron-ion interactions were described by projector-augmented wave pseudo-potentials. The electronic wave functions were represented by plane waves with a cutoff energy of 450 eV. Ionic relaxations were performed using the conjugate-gradient algorithm until the Hellmann-Feynman forces became less than 1.2×10^{-2} eV/Å. After relaxation of each LTO/KTO supercell the spin-polarized density of states (DOS) was computed using the tetrahedron method on the Γ-centered and dense k-mesh. Additionally, the DOS and band structure calculations, E(k), were performed also in the presence of SOC using the noncollinear VASP option [89]. This allows us to treat the 2DEG system with both the Rashba type and non-Rashba spin splitting. For the Mott insulator LTO, the U parametrization [90] of U_{eff} = 2.3 eV was applied to the 3d orbitals of Ti that gives for orthorhombic (Pnma) lanthanum titanate (i) the band gap of 0.5 eV, (ii) the G-type antiferromagnetic structure and (iii) the Ti magnetic moment of 0.7 μ_B.

For the LTO/KTO (110) interface, we used a 240-atom supercell which contains the 8-f.u.-thick LTO overlayer and a 8-f.u.-thick KTO substrate. Each in-plane layer contains four f.u.s of the ABO_3 perovskite. Here we used a set-up, within the slab geometry with a vacuum layer of 10 Å. The LTO/KTO (111) interface was simulated using a 140- atom 8-f.u.-thick/4-f.u.-thick supercell, where each atomic layer contains two f.u.c of ABO_3. Except for the two bottom

KTO layers which mimic the substrate, all other atoms of the supercell were allowed to relax. The experimental lattice parameters of orthorhombic LTO were used for the in-plane geometry. This set-up allows for all degrees of freedom, including the O tilting in LTO, its G-type antiferromagnetism and open surface.

Origin of ferromagnetism (Oxygen vacancies model vs. surface passivation)

We have carried out additional calculations to inspect the potential role of oxygen vacancies at the $KTaO_3$ substrate surface in the evolution or affecting the magnetism at KTO/LTO interfaces. The calculations of oxygen vacancies are based on relativistic models in which the spin orbit coupling effects due to Ta atoms are considered. Various concentrations of oxygen vacancies at the surface of $KTaO_3$ substrate are created to prob the possible change and in the magnetic moment values per vacancy accordingly. Figure S4.10, illustrates the density of states as function of the fermi energy at 0.0, 0.69, 1.23, 4.17 % concentrations of oxygen vacancies at KTO surface and the corresponding magnetic moment per vacancy is shown in each case. The schematic of magnetization density in $KTaO_3$ with 4.17 % concentrations of the vacancies is shown in Fig. S4.11.

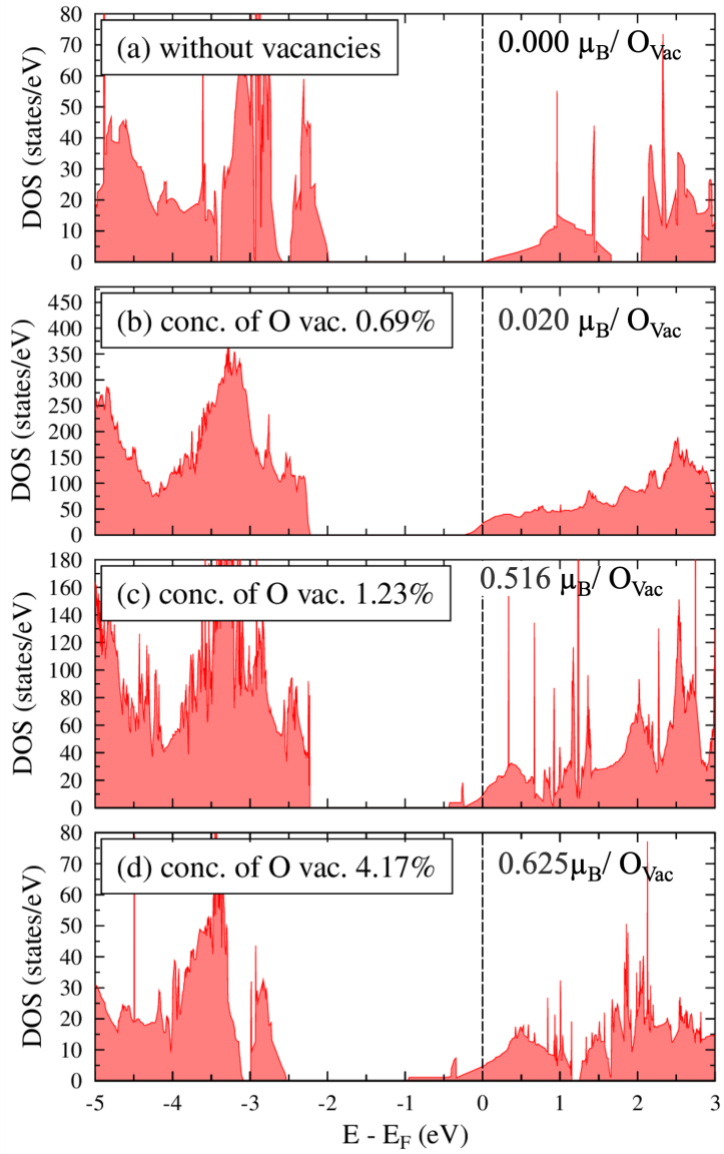

Figure S4. 10. Density of states as function of the energy of $KTaO_3$ (a) Perfect stoichiometric $KTaO_3$ without any oxygen vacancies, (b) Oxygen vacancy deficient $KTaO_3$ considering vacancies concentrations of ~ 0.69 %, and (c) with considering oxygen vacancies concentrations of ~ 1.23 % and (d) at oxygen vacancies concentrations of 4.17 %.

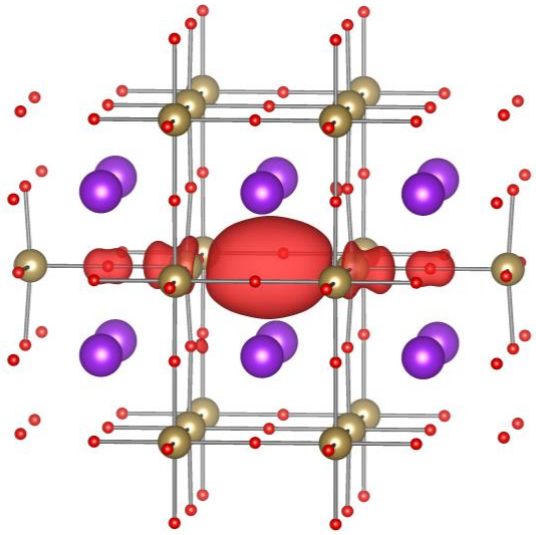

Figure S4. 11. Magnetization density of oxygen deficient $KTaO_3$ substrate in case of ~ 4.17 % oxygen vacancies concentrations as calculated by density functional theory (DFT).

The potential effect of surface passivation on the induced ferromagnetism at KTO/LTO interfaces is inspected by the DFT via introducing oxygen excess on the surface of LTO layer as shown in Fig. S4.12 (a, b) The result of surface passivation indicates the magnetism vanishes when the surface is passivated.

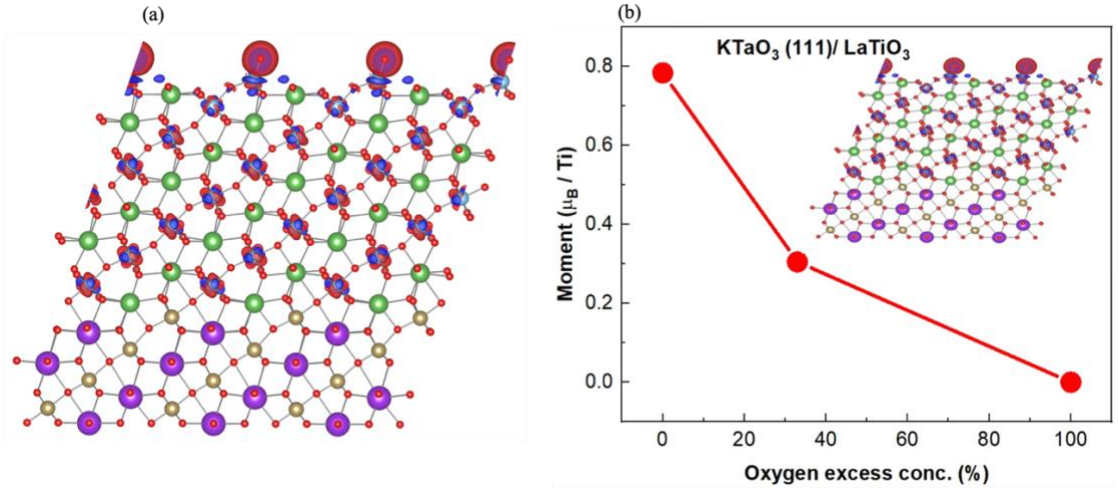

Figure S4. 12. Surface passivation model. (a) A sketch shows the passivation of Ti atoms with oxygen, (b) The calculated magnetic moment per titanium atom as function of oxygen excess concentrations as calculated by DFT ab-initio calculations.

4.5.7. **Structure and magnetism in KTO (100)/LTO case**

The RSMs scans of KTO (100)/ LTO sampels at various t_{LTO} as seen in Fig. S4. 13 shows the absence of strain as compared to case of KTO (111)/LTO samples for example. The absence of strain in the KTO (100)/LTO case may correlate with the absence of superconductivity in (100)-oriented KTO interfaces. To elucidates this and for confrimation, a detailed investigatinons and further study would be very interesting.

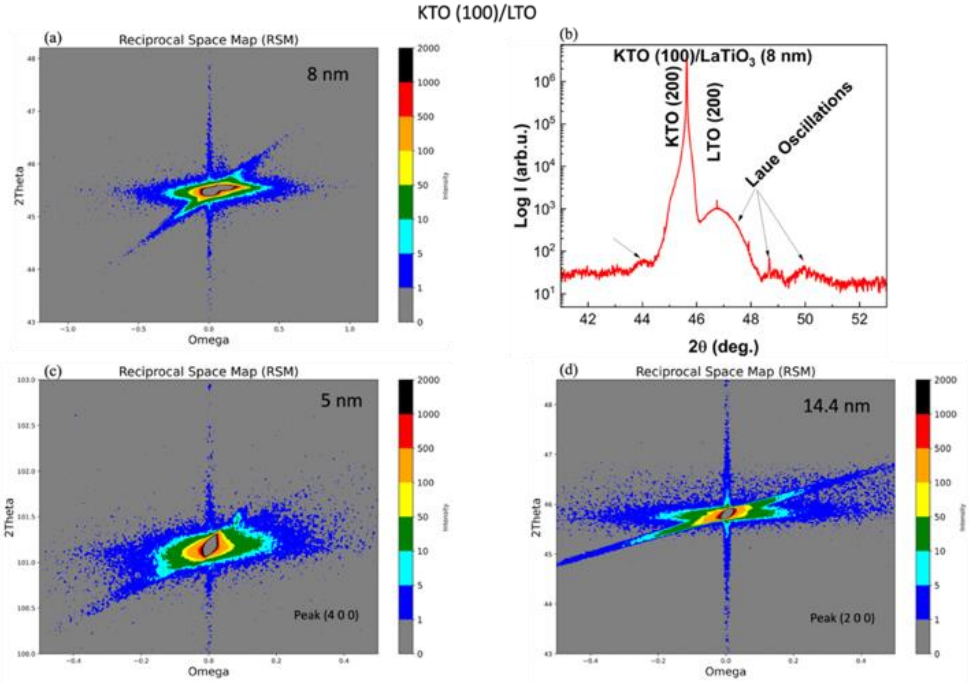

Figure S4. 13. Reciprocal space mapping (RSM) for (a) KTO (100)/LTO (8 nm), (b) XRD-pattern of same sample shown in (a), (c) RSM for KTO (100)/LTO (5 nm) (d) RSM for (14.4 nm) sample.

The electrical and magnetic transport measurements showed the observation of ferromagnetic ordering in KTO (100)/LTO thin films, this was supported by the anomalous hall effect hysteresis loops (Fig. S4. 14) and butterfly magnetoresistance hysteresis loops at 2 K (See Fig. S4.14 (b) as well as in-plane magnetization loops art 2 K (Fig. S4. 14 (c)).

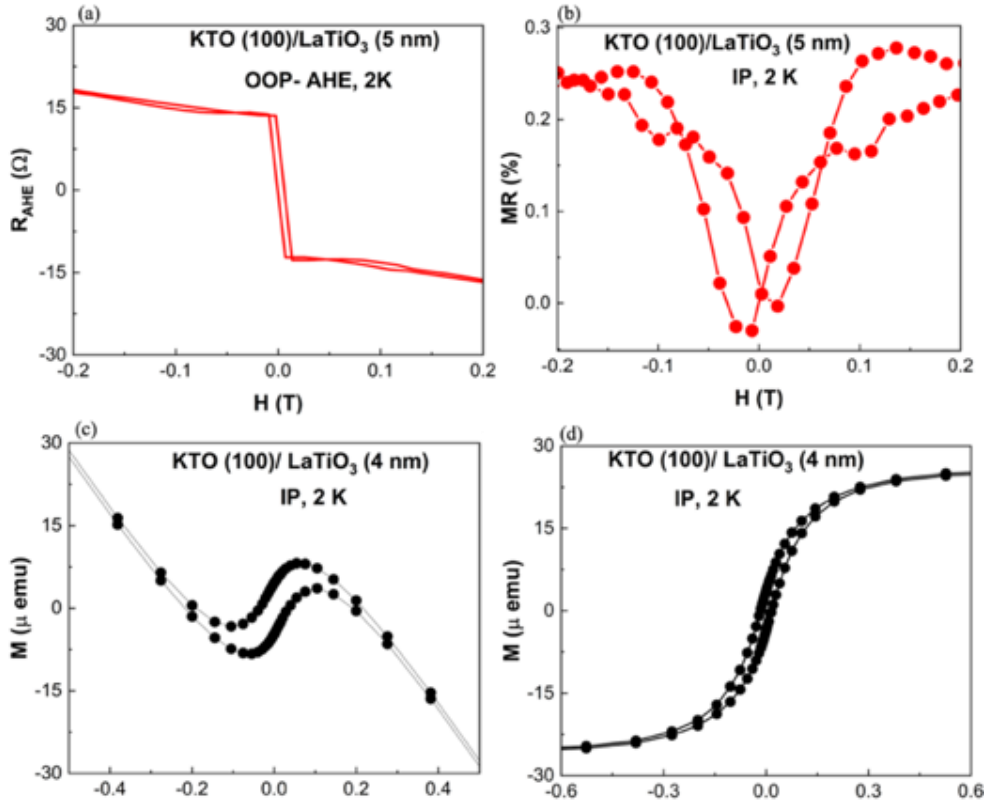

Figure S4. 14. Magnetic field dependence of the transverse resistance measured at 2 K for KTO (100)/LTO (5 nm) sample, (b) Magnetoresistance showing the butterfly shaped hysteresis loop for the same sample at 2 K measured within an IP magnetic field configuration, (c) The magnetic field dependence of magnetic moment measured at 2 K for KTO (100)/LTO (4 nm) sample (As measured), (d) The same data in (c), but with subtraction of the substrate moment of the (as -measured KTO substrate).

5. Proximity induced effects at the 2DEGs based interfaces: $KTaO_3/LaTiO_3$ /TiN

Atomically sharp heterointerfaces can exhibit exotic physical properties beyond those of the constituent materials. One very interesting such interface is that formed by a superconducting layer and a non-superconducting magnetic material. Here, we show that the superconducting transition temperature (T_c) in an overgrown TiN_x layer formed on the ferromagnetic oxide $KTaO_3$/ $LaTiO_3$ (LTO) 2DEGs can be tuned via proximity effects. A thin LTO layer is first epitaxially grown on a $KTaO_3$ (111) single crystalline substrate followed by growth of superconducting TiN. Transport data indicates the formation of a two-dimensional electron gas (2DEG) at the KTO (111)/LTO interface in addition to the emergence of ferromagnetism below 45 K establishing a spin-polarized 2DEG. The T_c of a thin layer of TiN grown on top of KTO/LTO is modestly enhanced which we attribute to an interplay of the spin-polarized 2DEG with the superconducting islands resulting in a reduced disorder in TiN. More interestingly, we found that the interfaces of a lower T_c result in a higher upper critical field (H_c) value. One possible interpretation of such anomaly in the H_c behavior could be attributed to the formation of a new superconducting layer at the interface. Such coupling can be of potential importance providing opportunities in enabling superconducting spintronics for quantum computing applications.

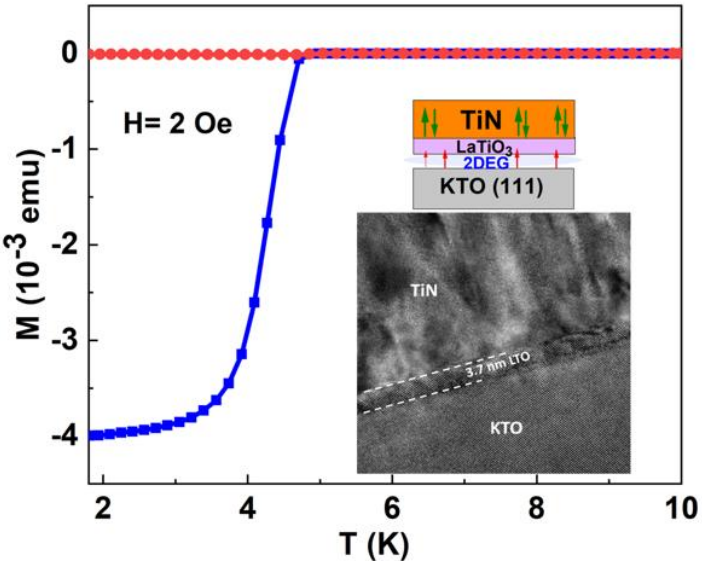

5.1. **Introduction**

The engineering and control of the physical properties of interfaces are fundamental to the operation of many technologically relevant devices and for the emergence of novel phenomena. Of particular interest are interfaces between metallic or superconducting layers and magnetic materials, especially antiferromagnetic (AFM) materials, which could allow for mediation of the interactions that form Cooper pairs and, thereby, provide a path towards high-temperature superconducting engineered interfaces. Conventional s-wave superconductivity and ferromagnetism are known to be antagonistic phenomena that lead to the suppression of proximitized superconductivity in the ferromagnetic material on very short-length scales[91-93]. Similarly, the T_c of the high-temperature superconductor $YBa_2Cu_3O_{7-\delta}$ is suppressed in proximity to layers of the ferromagnet (FM) $La_{0.7}Ca_{0.3}MnO_3$ [94]. A long rang proximity of ferromagnetic materials such Co with superconducting nanowires is also investigated[95]. Materials without any long-range ferromagnetic order have also been extensively explored in heterointerfaces with superconducting materials. These include semiconducting layers as in GaN/NbN heterostructures,[96] antiferromagnetic layers (AFM) as in $LaFeO_3$/FeSe heterointerfaces[97] and doped $SrTiO_3$ / FeSe [98]. Liu et al. ascribed the origin of interfacial superconductivity in $EuTiO_3$/FeSe to the role of antiferromagnetic spin fluctuations[99] and AFM spin fluctuations were attributed to be the origin of interfacial induced superconductivity at the interface between two non-superconducting materials, such as in the $Sb_2Te_3/Fe_{1+y}Te$

heterostructure[100]. Whereas Hubener et al. showed a reduction of T_c in Cr/V/Cr heterostructures[101].

Thus, the exploration of FM or AFM layers to influence superconducting order at an interface is highly interesting. In this work, we explore interfaces formed between thin layers of the AFM $LaTiO_3$ (LTO) and the nitride superconductor TiN_x. Bulk LTO is a G-type antiferromagnet with a perovskite crystal structure and exhibits a Mott insulator transition at ~120-146 K[102-104] . LTO displays a metallic 2DEG behavior at the interface with $SrTiO_3$ (STO)[105,106].Moreover, LTO exhibits canted spins at low temperatures due either to a Jahn-Teller distortion or to an antisymmetric Dzyaloshinski-Moriya exchange interaction (DMI) and, thereby, is a weak ferromagnet[107-109]. TiN_x is a superconductor that has been reported to exhibit a homogenous disordered superconductivity state (associated with a pseudo gap above $T_c \sim 7$ K). The resistance of TiN thin films drops to zero at a transition temperature that varies with the thickness of the film[15,110,111]. Bulk TiN is considered to be a conventional type- I superconductor that has a superconducting transition temperature of T_c =5.6 K in pure single crystals[112]. However, the highest reported T_c for thin films of thickness $\geq$ 700 nm is ~5.25 K[113,114]. Being a disordered superconductor, TiN is an interesting candidate for exploring and understanding the physical phenomena of pseudo-gapped superconductors. Experimental and theoretical work has been performed on the interplay between superconductivity and disorder as well as the role of superconducting islands in disordered superconductors such as TiN_x[115-117].

Here we report experimental results concerning the tuning of superconductivity in disordered superconducting titanium nitride TiN_x thin films grown in proximity to LTO thin layers in the heterostructure KTO/LTO/TiN_x system. The heterostructures were grown using a dual molecular beam epitaxy (MBE) growth module Veeco-GEN10, designed specifically for nitride and oxide film growth respectively, which are in-situ connected to each other via a central storage UHV ($1x10^{-11}$ Torr) chamber.

5.2. **Experimental Methods**

The growth of oxides and nitrides layers such as LTO and TiN_x samples were performed using a VEECO GEN10 molecular beam epitaxy (MBE) cluster system having two separate growth chambers, dedicated to oxide and nitride growth, respectively. A central chamber contains a robot for the automated transfer of wafers between the two chambers. The base pressures in the growth and robot chambers are maintained at $< 2\times10^{-10}$ Torr using a combination of turbo-, ion-, and cryo-pumps. High-purity elements were evaporated by high-temperature retractable effusion cells. An ozone source and radio frequency plasma sources allowed for reactive oxygen and nitrogen at pressures of 8×10^{-8} and 1×10^{-5} Torr, respectively. KTO substrates (SurfaceNet GmbH) were cleaned in acetone, methanol, and isopropanol, each for 15 mins, respectively. Then the substrates were outgassed at 200 ^{o}C for 30 mins in a load lock chamber ($< 10^{-8}$ Torr) before being introduced into the growth chambers. The substrates were further cleaned at 850 ^{o}C for 1 hour before performing the LTO growth at ~800 ^{o}C. After LTO growth the samples were transferred to the nitride chamber for TiN growth at ~750 ^{o}C. The film surface quality was monitored using in-situ RHEED. The surface topography was inspected by performing atomic force microscopy (Bruker Scan-Asyst Dimension Icon- PT system) revealing very good surface quality despite the in-situ transfer between the oxide and nitride chambers. (see supporting information for more details) Rutherford backscattering spectroscopy was used to determine the elemental composition and thickness of the grown films. For high-resolution (S) TEM imaging, electron-transparent lamellae were prepared using an FEI Nova 600 Nanolab focused ion beam (FIB) microscope. The cross-sectional lamellae were investigated in a JEM-F200 electron microscope equipped with a Schottky-type electron source and an annular dark field (ADF) detector at an accelerating voltage of 200 kV. The viewing direction was along KTO [1-10]. The magnetic properties were measured using the ultra-low field module in a Quantum Design superconducting quantum interference device (SQUID- MPMS3) magnetometer using both the DC-mode and VSM modes. The 4-probe and Hall-bar devices were fabricated using optical lithography in the cleanroom. First, channels with areas of 20 × 100 μm^2 and 5 × 100 μm^2 were defined using a negative photoresist (Allresist® AR-N 4340), and then argon ion beam milling using an SCIA coat 200 system was used to pattern the metal films. Second, contacts were formed using a positive photoresist

(Allresist® AR-P 3540T) and argon ion beam sputter deposition of electrical contacts formed from Ti (3nm)/Au (70nm) using an SCIA coat 200 system. The crystal structure of the as-grown films was determined using a high-resolution four-circle D8- Bruker x-ray diffractometer system. The electrical and magnetic transport properties of the samples and devices were performed in a Quantum Design physical property measurement system (Dynacol, PPMS-9T). The DC- measurements are performed using an applied current 0.5- 0.6 mA via the Keithley 6221 current sources and Keithley 2182 voltage meters. The current-voltage measurements were performed in the PPMS using an applied AC-current by using the Stanford lock-in amplifiers in which the applied alternative current I_{ac} equals 5V/100 KΩ, the frequency f is from 13 Hz to 19 Hz, the time constants are from 200 ms to 300 ms and the sensitivity = 500 μV.

5.3. **Results and discussion**

The crystal structure of the grown thin film samples ($LaTiO_3$, TiN, and $LaTiO_3$/TiN) on KTO (111) was investigated using high-resolution X-ray diffractometry (HR-XRD). Figure 5.1 shows the XRD patterns of various thin films ($LaTiO_3$, TiN, $LaTiO_3$ /TiN) grown on KTO (111) single crystal showing their epitaxial growth. The inset enlarges the scan range around KTO (111) which consists of a clear LTO peak orienting in the same direction as that of the substrate. The measured lattice parameter of the grown LTO layers ($a_{LTO.\,(111)}$ = 3.95 Å) was found to be very close to that of the KTO substrate having a lattice mismatch of ≈ 0.8%. The temperature dependence of the sheet resistance R_s (T) of the as-grown KTO/LTO samples is shown in Figure 3.16 for several thicknesses t_{LTO} of LTO along (110)- and (111)- oriented KTO substrates. The films are metallic to low temperatures with high residual resistance ratio (RRR~ 100) for certain t_{LTO}. Clear evidence for a 2DEG is seen for the KTO (111)/LTO as was explained in chapter 3, with electron mobility reaches 250 cm^2/V. s at 2 K in excellent agreement with LTO/ KTO (100)[41,106].

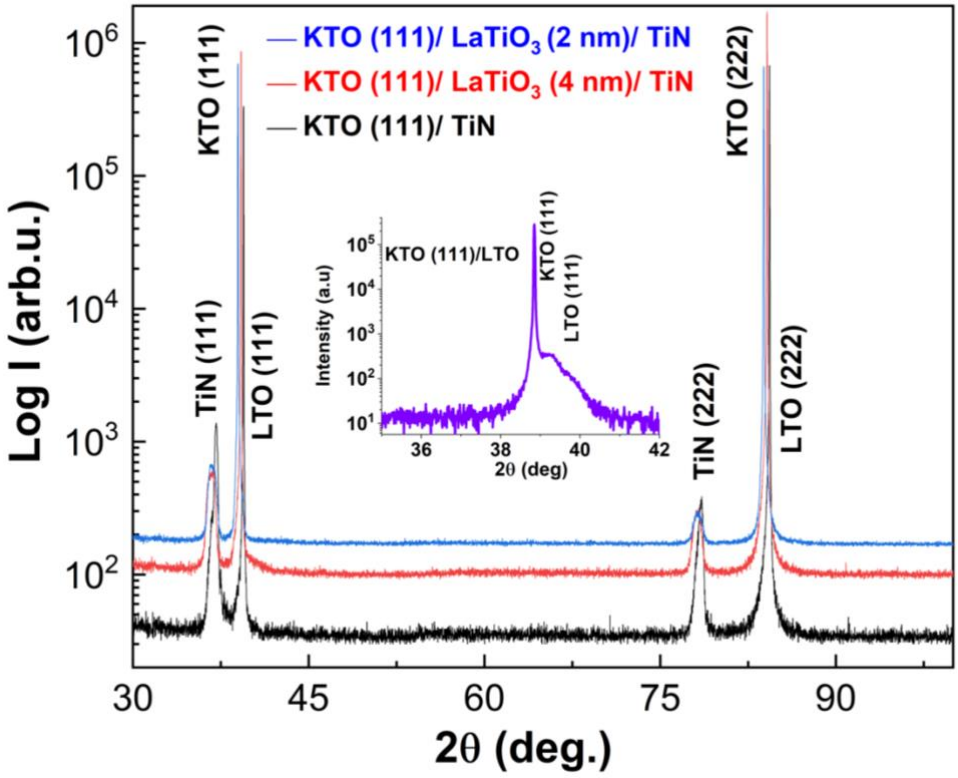

Figure 5.1. X-ray diffraction (XRD) patterns of KTO (111)/LTO, KTO (111)/TiNx, KTO (111)/t_{LTO} LTO/TiN_x with t_{LTO} = 2 and 4 nm. All the samples were grown at the same thickness of TiN (115 nm), and the inset shows a magnified view of the XRD diffraction pattern around the KTO (111) peak.

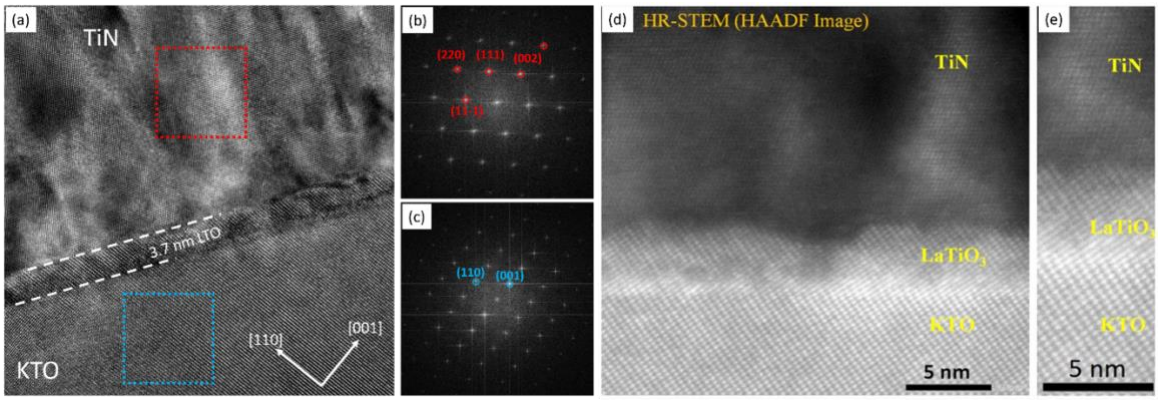

Figure 5. 2. From left to right: (a) HR-TEM image of KTO (111)/$LaTiO_3$/TiN with (b-c) fast Fourier transforms (FFT) of the TiN and KTO regions highlighted as dashed red and blue

boxes; (d-e) HR-STEM high angle annular dark field low and high magnifications images of KTO (111)/$LaTiO_3$/TiN.

High-resolution transmission electron microscopy (HR-TEM) scans were performed to evaluate the structural integrity of the thin film heterostructures. A low magnification cross-sectional TEM image of a KTO/LTO/TiN sample oriented along the KTO <1-10> zone axis is shown in Fig. 5. 2a. Fast Fourier transform (FFT) images from the areas shown as dotted squares in TiN and KTO reveal that these layers have a cubic structure oriented along <111> as shown in Fig. 5. 2b which agrees with the HRXRD $\boldsymbol{2\theta - \omega}$ scans displayed in Figure 1a. HR-STEM HAADF low and high-magnification atomic lattice images in Fig. 5. 2c-d show that the interfaces are atomically sharp without any obvious defects. Thus, the HRTEM investigations show that despite the different growth environments in oxide and nitride MBE chambers (see methods for more details), we obtain high-quality single-crystalline defect-free thin films.

Fig.5.3(a) shows a Superconducting transition from resistivity versus temperature measurements for the KTO/TiN and KTO/LTO/TiN samples. A 25 nm thick TiN film shows the T_c of 3.7 K. Inset shows the LTO layer thickness-dependent superconducting transition temperature. When a thin AFM LTO layer is inserted at the KTO/TiN interface T_c is found to be slightly changed. However, when the thickness of the TiN film is significantly increased to 115 nm, a significant enhancement of T_c up to 5 K was found for the thinnest (0.39 nm) LTO layer, as shown in Fig. 5.3(b). This confirms the role of the LTO layer in the tuning and enhancement of the superconducting state at the interface. The dependence of the electrical resistance on the out-of-plane magnetic field for several temperatures below T_c is shown in Fig. 5.3(c), 5. 3(e), and Fig. 5.3(f) for KTO/LTO (t_{LTO})/ TiN (115 nm) samples with t_{LTO} = 0, 0.39 and 0.59 nm. The corresponding variation of R with temperature is shown in Fig. 5. 3(d) for several fields for the t_{LTO} = 0.39 nm sample.

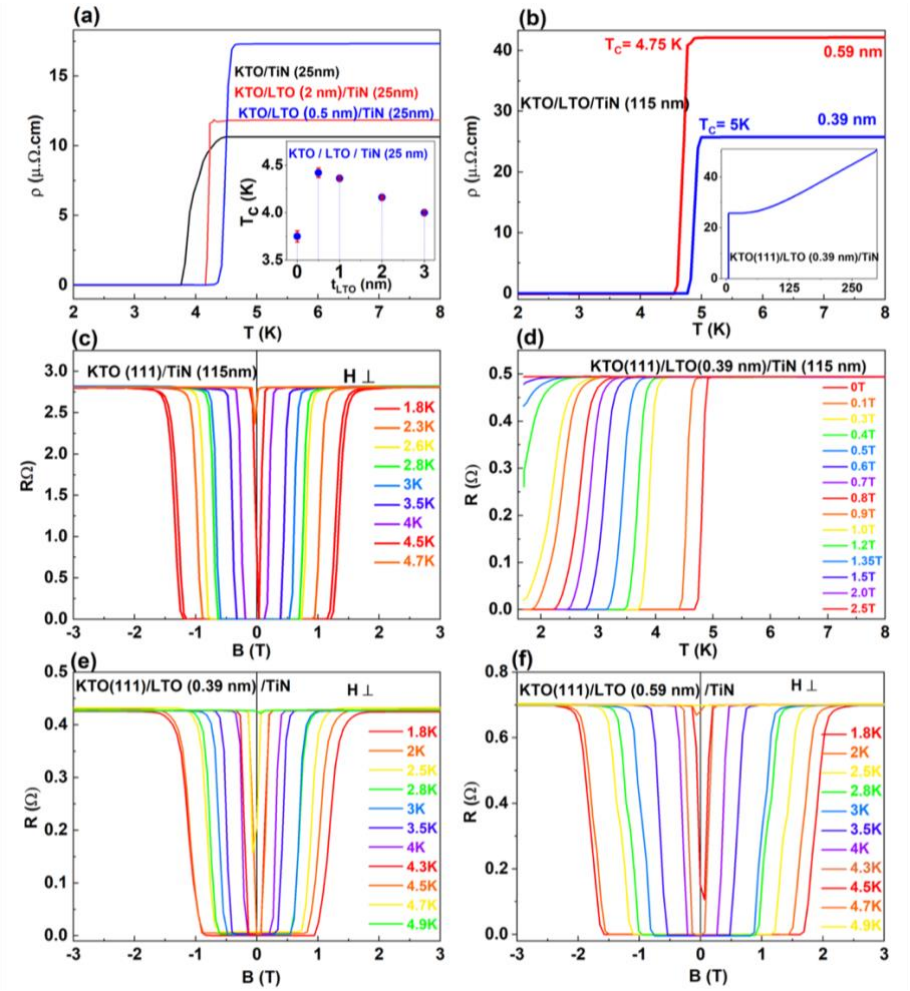

Figure 5.3 (a) Temperature dependence of the electrical resistivity ρ (T) showing superconducting transition (T_c) for samples KTO (111)/TiN (25 nm) and KTO/LTO/ TiN. The inset shows the variation of T_c as a function of the LTO layer thickness where the TiN thickness (25 nm) is the same for all samples, (b) ρ(T) for KTO (111)/ LTO/ TiN (115 nm). The inset shows ρ (T) from 300 K to 2K for KTO/LTO (0.39 nm)/TiN (115 nm), (c) magnetic field dependence of the electrical resistance of KTO (111)/ TiN (115 nm) at different temperatures, (d) temperature dependence of the electrical resistance for KTO (111)/ LTO (0.39 nm)/ TiN (115 nm), (e and f) magnetic field dependence of the resistance at different temperature of KTO (111)/ LTO (0.39 nm)/ TiN (115 nm) and KTO (111)/LTO (0.59 nm)/ TiN (115 nm).

Interestingly, there is no correlation between T_c and the critical magnetic field. For example, despite the higher T_c observed in the t_{LTO} = 0.39 nm sample, the critical magnetic field is lower than that in the t_{LTO} = 0.59 nm. The critical field for the sample without the LTO layer exhibits

an intermediate value. To confirm whether the superconductivity is bulk-like, the Meissner effect of magnetic field expulsion was measured, for the sample with t_{LTO} = 0.39 nm. Fig. 5. 4(a) shows zero-field cooling (ZFC) and field-cooling (FC) curves. For zero-field curves, first, the sample was cooled down to 2K at zero field then the data was collected in the warming-up step while the field was set to 2 Oe. Whereas for FC data, the sample cooling-down and warming-up steps were carried out in presence of the field and the data was recorded while the sample was warming up. Inset shows the volume susceptibility curve calculated from the ZFC curve. The sample shows a nearly complete Meissner effect with ~ 99.2 % volume fraction field expulsion.

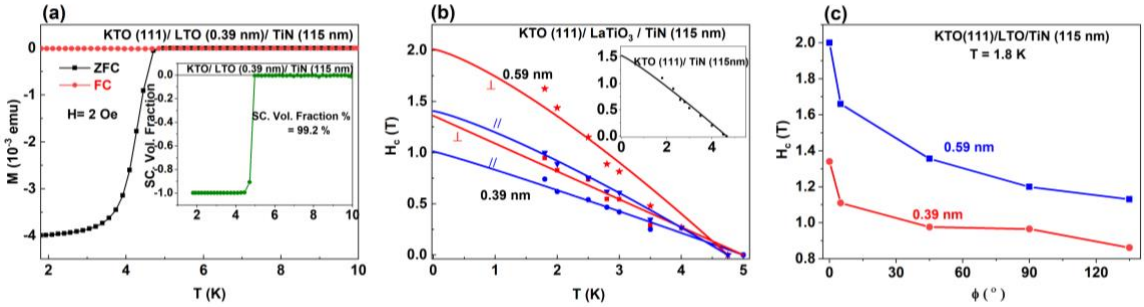

Figure 5. 4. (a) Zero-field and field cooling curves measured at 2 Oe, and the inset shows the superconducting volume fraction of the t_{LTO} = 0.39 nm sample. (b) Hc versus T_c for out-of-plane and in-plane magnetic field configurations for the t_{LTO} = 0.39 and 0.59 nm samples. The solid lines fit the Ginz burg-Landau (GL) formula to the data (ref.32). The inset shows OOP data for the sample with t_{LTO} = 0. (c) Angular dependence of H_c at T= 1.8 K for the t_{LTO} = 0.39 and 0.59 nm samples.

Fig. 5. 4(b) illustrates the critical field (H_c) values for two superconducting KTO/LTO (t_{LTO})/TiN (115 nm) samples for t_{LTO} = 0.39 and 0.59 nm, measured for both in-plane (||) and out of -plane (⊥) magnetic field orientations. same measurements were carried out for 5 samples with different t_{LTO}. In each case, H_c is higher for the field in an out-of-plane configuration. In contrast to the Ginzburg-Landau theory, these measurements demonstrate that the samples with higher T_c showed lower H_c which is unconventional[118]. Similarly, we determine H_c for intermediate angles in addition to the in-plane and out-of-plane geometries.

Fig. 5. 4(c) shows the angular dependence of H_c (1.8 K) from which we observe that the sample with t_{LTO} 0.59 nm holds higher H_c for all angles as compared to the t_{LTO} 0.39 nm sample.

Please note that we observed the formation of a ferromagnetic spin-polarized 2DEG at the KTO/LTO interfaces for few nm thick samples as shown in the results addressed in chapter 4 [119-122]. This clearly manifests that the coupling of spin-polarized 2DEG with superconductivity can induce exotic properties, such as it causes the enhancement in the superconducting transition temperature T_c of overgrown TiN_x. The observed unusual dependence of H_c on T_c for the KTO/LTO/TiN (115 nm) as seen in Fig. 5. 4(b) is a consequence of a peculiar disordered superconducting state in TiN. Ghosal et al. found that the high-disorder system turns into superconducting islands, having a large pairing amplitude, connected by an insulating sea [123]. Similarly, Dubi et al. demonstrated that the disorder resulted in the formation of islands processing high superconducting order[124]. Such disordered superconductors exhibiting unusual properties needed to be treated via unconventional approaches. Furthermore, it has been reported that when the disorder increases, the correlations between these superconducting islands are suppressed which can give rise to a new superconducting state due to the merging of these islands or a superconducting-insulating state weakly coupled via the Josephson effect[115,117,125]. Hence, we demonstrate that the proximity of the magnetic LTO layer to the TiN superconductor suppresses the disordered state of the LTO/TiN interface system due to the merging of the islands. As a result, this interface unusually shows higher values of H_c despite the lower T_c [115,124].

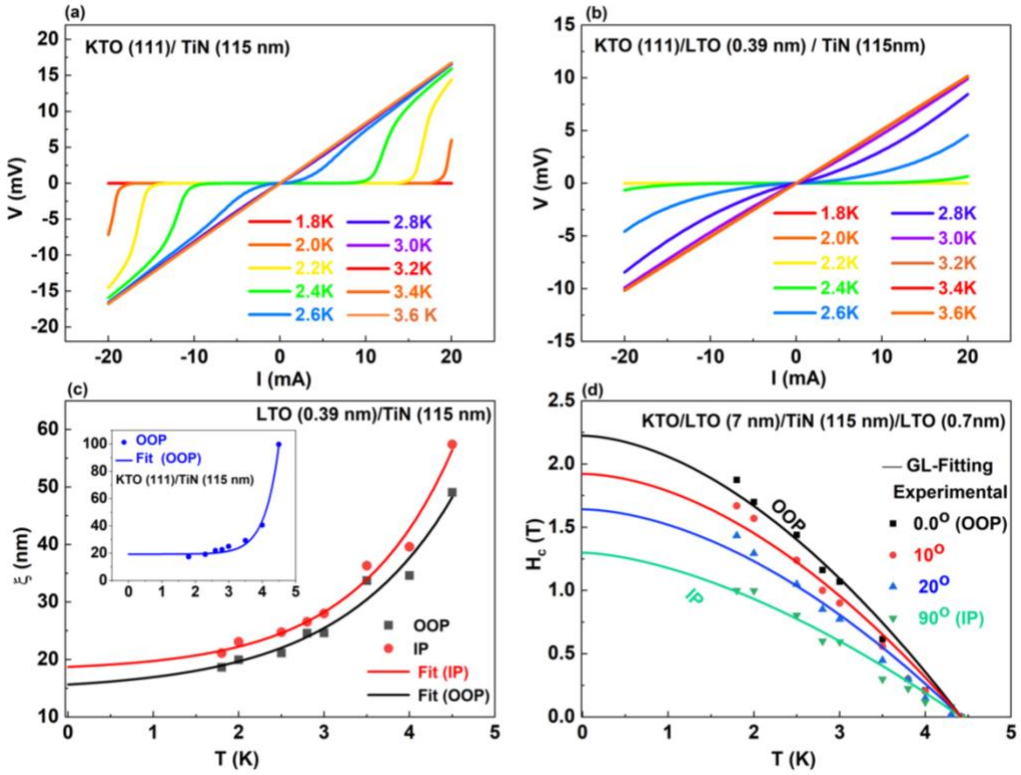

Figure 5. 5. Voltage vs ac current curves that are measured in an OOP field of 0.7 T at several temperatures for (a) KTO/TiN (115 nm) and (b) KTO/LTO (0.39 nm)/TiN (115 nm) samples. (c) ξ as a function of T_c for KTO/ LTO (0.39 nm)/ TiN (115 nm). (d) Critical field versus temperature plot for the tri-layer heterostructure KTO/LTO (7nm)/TiN (115 nm)/ LTO (0.7 nm) for several angles made by the field with sample plane, whereas the solid lines fit the GL equation to the experimental data.

Fig. 5. 5(a) and Fig. 5. 5(b) shows ac-current vs. voltage characteristic curves obtained while applying an out-of-plane magnetic field of 7 kOe for the KTO/TiN (115 nm) and KTO/LTO (0.39 nm) /TiN (115 nm) samples at various temperatures. It is evident that the superconducting state is suppressed above a critical current. Similar plots for KTO/ TiN (115 nm), KTO/LTO (0. 39 nm)/ TiN (115 nm), and KTO/LTO (0. 59 nm)/ TiN (115 nm) samples at zero field are shown in the SI. Fig. 5. 5(c) depicts the coherence length ξ (T_c), for the KTO/LTO (0. 39 nm)/ TiN (115 nm) sample, which is determined by employing GL theory to the H_c vs T_c data acquired in out-of-plane (OOP) and in-plane (IP) configurations. It is found

that the ξ (T_c) is larger (smaller) for OOP (IP). A similar trend is observed for the KTO/LTO (0. 59 nm)/ TiN (115 nm) sample (see SM).

To have a deeper understanding on the role of the ferromagnetic KTO/LTO layer on superconducting TiN, the other set of films was prepared in which the TiN superconducting layer is sandwiched between LTO layers. Fig. 5.5(d) shows the measured critical field versus temperature plot for such trilayer heterostructure, KTO/LTO (7 nm)/TiN (115 nm)/LTO (0.7 nm). This sample shows a larger value of H_c as compared to the bi-layer structures. In addition, this sample shows an unusual upward feature in the H_c (T_c) curves at low temperatures for all orientations of a magnetic field. However, the T_c (4.42 K) of the trilayer is smaller than that of the bilayer, H_c of the trilayer is found to be larger than that of the bilayer. This manifests that the unusual trend of increased H_c despite of low T_c is observed only for the bilayer system which can be ascribed to the interplay of spin-polarized 2DEG that proximities with the disorder superconducting islands of TiN. Note that in the case of the tri-layer system not only H_c is larger but also the coherence length ξ is larger than those in the bi-layer systems.

The enhanced superconductivity of the grown TiN thin films via the proximity of $LaTiO_3$ with TiN in the bi-layer samples is ascribed to the correlation interactions between the spin-polarized 2DEG and the disorder superconducting islands. The enhancement in transition temperature at a lower thickness of the LTO layer is due to the higher electron mobility of 2DEG. However, an unusual increase of H_c when a_{LTO} is 0.59 nm is found as compared to a_{LTO} =0.39 nm. This anomaly is in contradiction to the usual concept of H_c (T_c) where the larger T_c leads to a larger H_c. But this concept applies if the coupling with the 2DEG did not lead to any correlation's effects at the interface. Therefore, if we supposed that the proximity effects and coupling of the spin-polarized 2DEG (KTO (111)/LTO) with disorder TiN induce a new superconducting layer at the interface, then attributing this large value of H_c (a_{LTO} =0.59 nm) will become no longer unusual, which means that the evolution of a new superconducting interface of a larger upper critical field value. On the other hand, this anomaly of the critical field might be also referred to as the competition between the pairing interactions in proximity to two layers of different electron mobility values in presence of a spin-polarized 2DEG (at a_{LTO} = 2.5 and 8 nm)[126].We endorse the former interpretation as a possible reason.

The observed upward curvature of the upper critical field H_c (T) at low temperatures below T_c in the case of the trilayers system can be attributed to two possibilities. It can be due to spin-orbit scattering effects, but this possibility is usually occurring when the H_c exceeds the Pauli paramagnetic limit. Which is not matching with our case whereas the upper critical field here is less than 1.86 T_c [44]. The other potential reason behind this observed upturn curvature of H_c can be attributed to the possibility of formation of a two-band superconductivity in the interfacial proximity of KTO/LTO/TiN/LTO.

5.4. **Conclusions**

We report two main observations in our epitaxial-grown heterostructures, the emergence of a novel spin-polarized 2DEG at the interface of KTO (111)/$LaTiO_3$ and the modest enhancement of superconductivity in TiN_x thin film through the proximity to the spin-polarized 2DEG in KTO (111)/LTO. The superconductivity in thin films of TiN, which has previously been shown to have a disordered superconducting state in which superconducting islands are weakly coupled, is explored here in heterostructures with thin magnetic LTO layers. We find that the superconducting ordering temperature of 115 nm thick TiN films is influenced by proximity to a 2DEG formed at the interface between thin films of LTO grown on KTO (111). We find evidence for magnetism in the 2DEGs from a Kondo minimum observed in resistance versus temperature measurements of the 2DEG and from the hysteretic behavior of the magnetoresistance. The T_c of the TiN film is slightly enhanced when deposited on the KTO/LTO 2DEG and, moreover, the upper critical field has an anomalous dependence on T_c. The anomaly behavior of the upper critical field as function of the LTO layer thickness is probably attributed to an evolution of a new superconducting layer at the interface. We ascribe this to spin-polarized 2DEG-induced correlations coupled with the disordered superconducting state in TiN.

5.5. **Supplementary materials (SM- 5)**

Fig. S5.1 displays surface topography scans obtained via atomic force microscopy. The topographic images of KTO (111)/LTO (5 nm) reveal an excellent rms roughness value of less than 0.2 nm for both LTO and LTO/TiN on KTO (111) substrates. The KTO (111)/LTO configuration shows fine step terraces on the film surface, indicating the high quality of the LTO thin films grown on KTO (111) substrates.

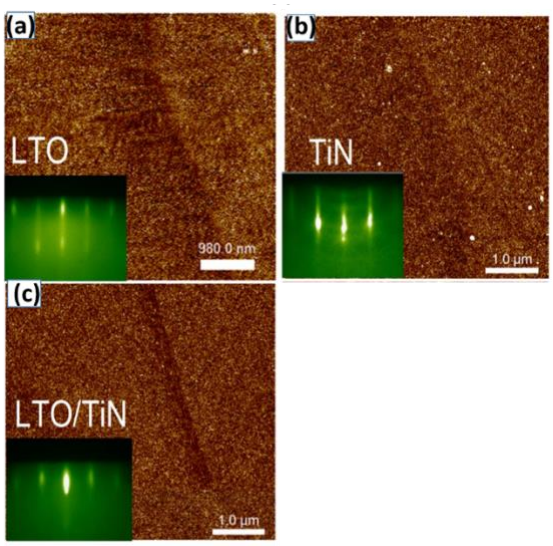

Figure S5.1. Atomic force microscopy (AFM) images at different scales. From a-c the AFM and RHEED images (shown in the insets) of KTO/LTO (30 nm), KTO/TiN (115 nm) and KTO (111)/LTO (0.59 nm)/ TiN (115 nm), respectively.

Reflection high-energy electron diffraction (RHEED) patterns were recorded in situ during molecular beam epitaxy (MBE) growth. The AFM images for KTO (111)/LTO (30 nm), KTO (111)/LTO (0.59 nm)/TiN (115 nm), and KTO (111)/TiN (115 nm) are shown in Fig. S5.1(a-c). The observed streaky RHEED patterns (shown in the inset to Fig.s1) align with the low rms surface roughness values from AFM, affirming the high-quality growth of both oxide and oxide/nitride interfaces.

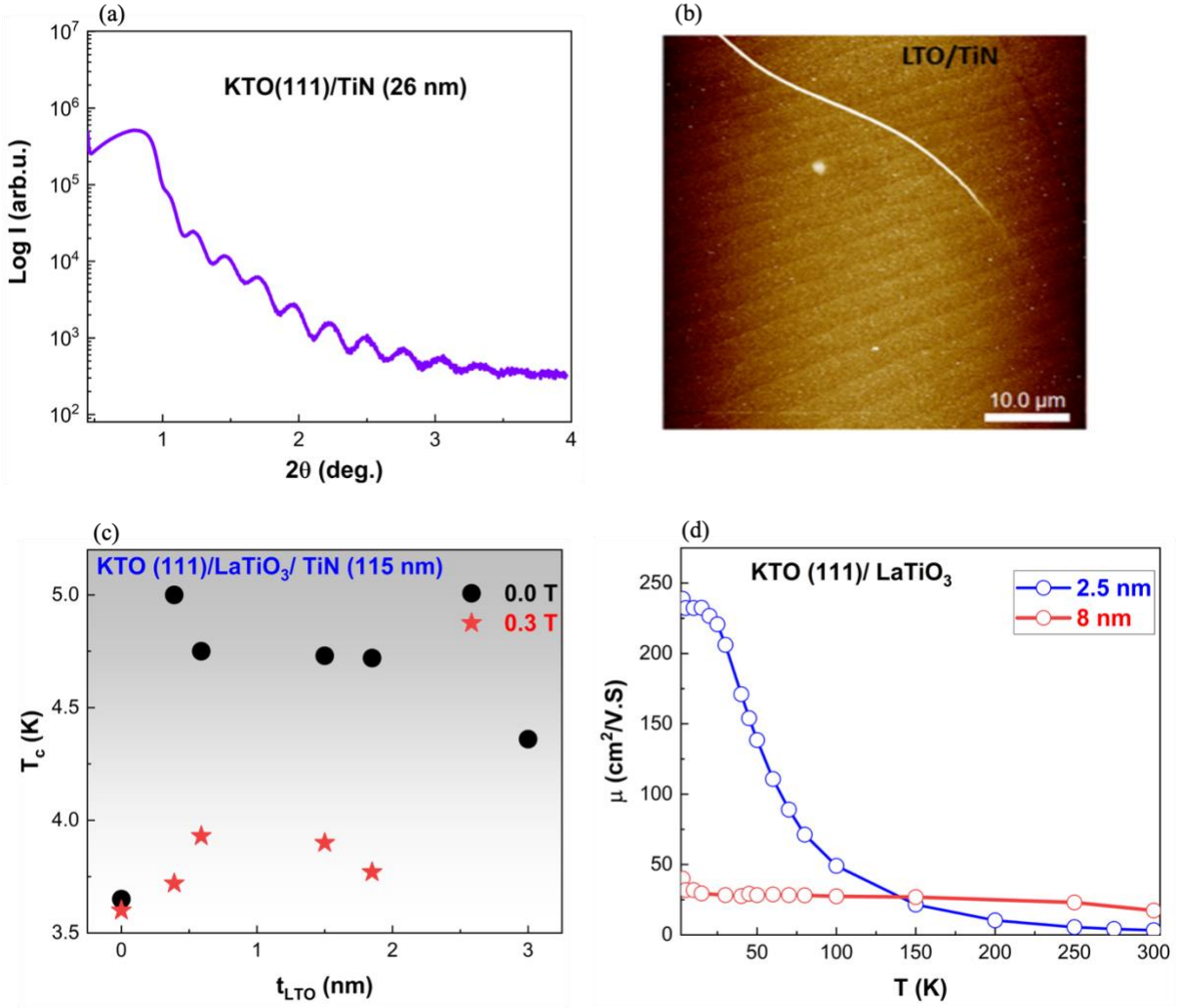

Figure S5.2. (a) X- ray reflection (XRR) of the grown KTO/TiN (28 nm) sample, (b) The AFM image of KTO /LTO/TiN (115 nm) at scan size of 50 µm x 50 µm (c) Temperature dependence of the 2D electron mobility in the 2DEG KTO (111)/$LaTiO_3$ system at different thickness. (d) Phase diagram of the grown superconducting KTO/LTO/TiN (115 nm) at different thickness of LTO layer.

The thickness of the KTO (111)/TiN film was measured using x-ray reflectivity (XRR), as illustrated in Fig. S5. 2(a). Fig. S5. 2(b) presents the surface topography of KTO/TiN over a large scan area of 50 × 50 µm², revealing the formation of step terraces on the film surface. Fig. S5. 2(c) displays the thickness dependence of the 2DEG mobility at the KTO (111)/LTO

interface. A phase diagram of the KTO/LTO/TiN heterostructure, depicting LTO thickness variations under different magnetic fields, is provided in Fig. S5. 2(d).

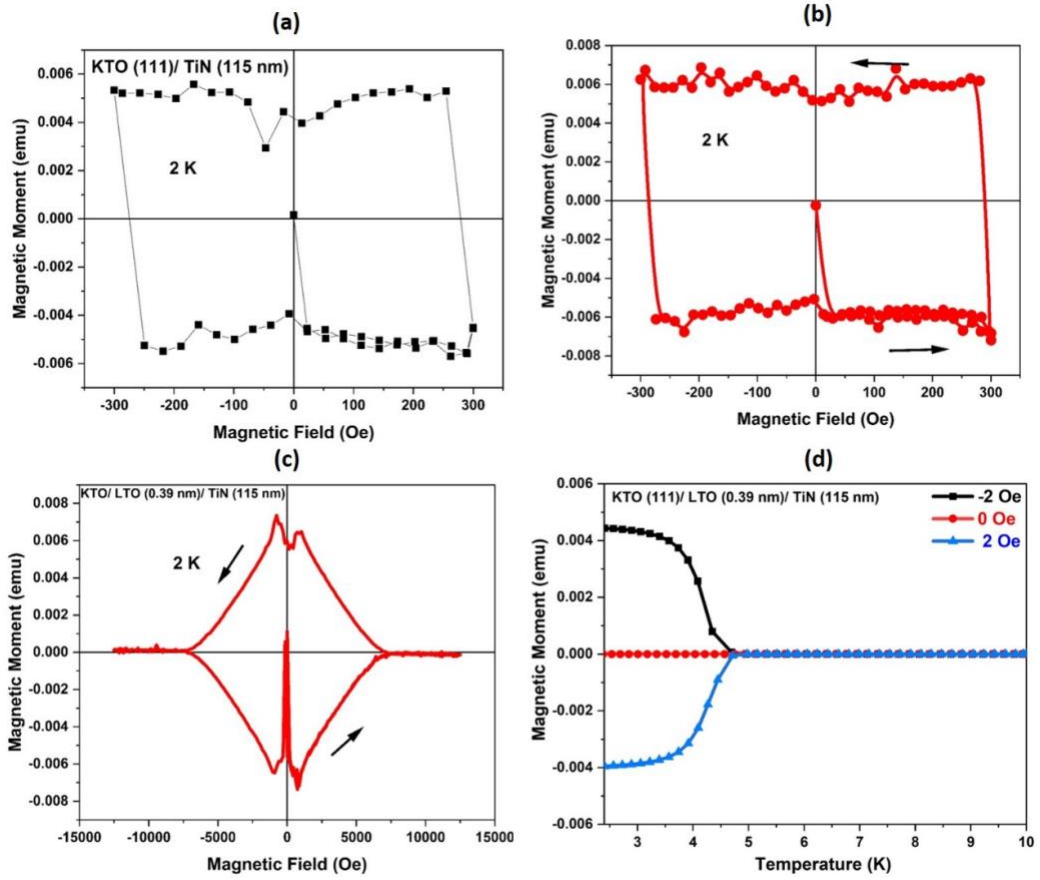

Figure S5. 3. The hysteresis loop at 2K of (a) KTO/ TiN (115 nm), (b) KTO (111)/ LTO (0.39 nm)/ TiN (115 nm) samples. (c) The hysteresis loop of the same sample but at a larger axis range of magnetic field. (d) Zero-field cooling and field cooling curves of KTO (111)/ TiN (115 nm). The zero-field cooling and field cooling of KTO (111)/ LTO (0.39 nm)/ TiN (115 nm) at 0 Oe, 2 Oe and -2 Oe applied field.

The magnetic field dependence of magnetic moment for the KTO/ TiN and KTO/LTO/TiN samples is shown via the magnetic hysteresis loops at low and large values of the applied magnetic fields as shown in Fig. S5. 3 (a-c) at temperature 2 K. The asymmetric behavior of the hysteresis loops at large values of magnetic fields is due to the complete penetration of the vortices, and the magnetization becomes no longer dependent on the field.

Fig. S5. 3(d) illustrates the observation of Meissner effect and perfect diamagnetism in the grown KTO (111)/ LTO (0.39 nm)/TiN (115 nm) film.

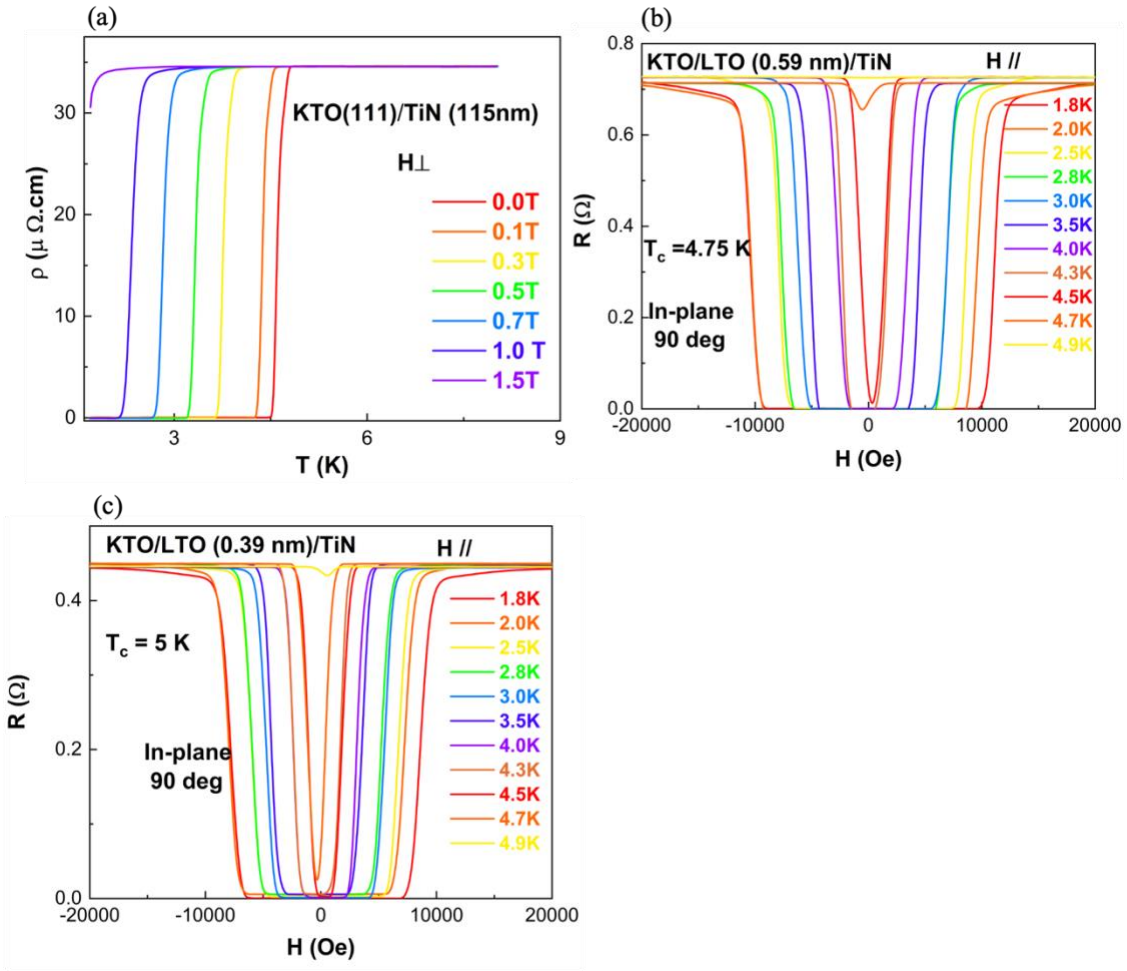

Figure S5. 4. (a) Temperature dependence of electrical resistivity in KTO (111)/TiN (115 nm) at out of – plan configuration. (b) In-plane magnetic field dependence of resistance of KTO (111)/LTO (0.59 nm)/ TiN (115 nm) at various temperatures. (c) The in-plane magnetic field dependence of resistance of KTO (111)/LTO (0.39 nm)/ TiN (115 nm) at different temperatures.

Fig. S5. 4 illustrates the transport properties of the grown KTO (111)/TiN (115 nm) film and the other bi-layer heterostructures KTO (111)/LTO/TiN (115 nm) as a function of the magnetic field and temperature in the out-of-plane (OOP) and in-plan (IP) configurations.

Fig. S5. 5 demonstrates the AC- current-voltage curves of the grown KTO (111)/ TiN (115nm) and KTO (111)/LTO (0.59 nm)/TiN (115nm) heterostructure interfaces in presence of an out-of -plane applied magnetic field to study its behavior as a function of the magnetic field.

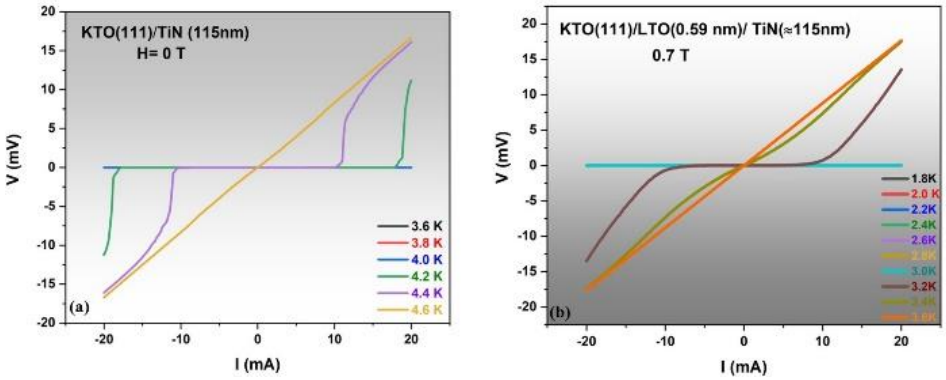

Figure S5. 5. Current-voltage curves in (a) KTO (111)/ TiN (115 nm), (b) KTO (111)/ LTO (0.59 nm)/ TiN (115 nm) and (c) KTO (111)/ LTO (0.39 nm)/ TiN (115 nm) at zero Oe field. (d) KTO (111)/ LTO (0.59 nm)/ TiN (115 nm) at 0.0 T applied field.

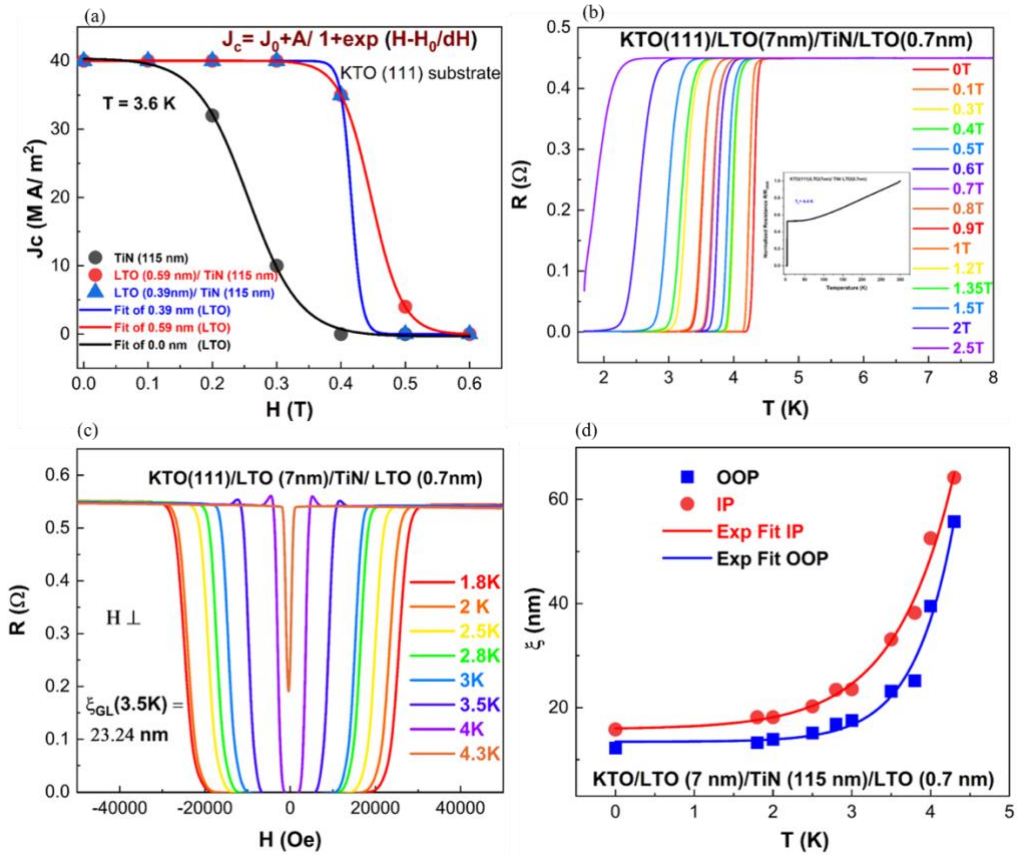

Figure S5. 6. (a) Magnetic field dependence of the critical current density J_c at 3.6 K. (b) Temperature dependence of resistance in KTO (111)/LTO (7 nm)/ TiN (115 nm)/ LTO (0.7 nm) device at different temperatures, the inset shows the temperature dependence of the resistance from room temperature down to 2 K. (c) The out of –plane magnetic field dependence of resistance of KTO (111)/LTO (7 nm)/ TiN (115 nm)/ LTO (0.7 nm) at different temperatures. (d) Temperature dependence of the coherence length in KTO (111)/LTO (7 nm)/ TiN (115 nm)/ LTO (0.7 nm) device.

The critical current density as a function of magnetic field was calculated for KTO/TiN (115 nm), KTO/LTO (0.59 nm)/TiN (115 nm), and KTO/LTO (0.39 nm)/TiN (115 nm) samples, with the fit shown according to the equation in the inset of Fig. S5. 6a. Fig. S5. 6 (b, c) displays the temperature and magnetic field dependence of the electrical resistance of the trilayer KTO (111)/LTO (7 nm)/TiN (115 nm)/LTO (0.7 nm) heterostructure in an out-of-plane configuration. The coherence length as function of temperature is shown in Fig. S5. 6(d) alongside with the fitting curves of the coherence length.

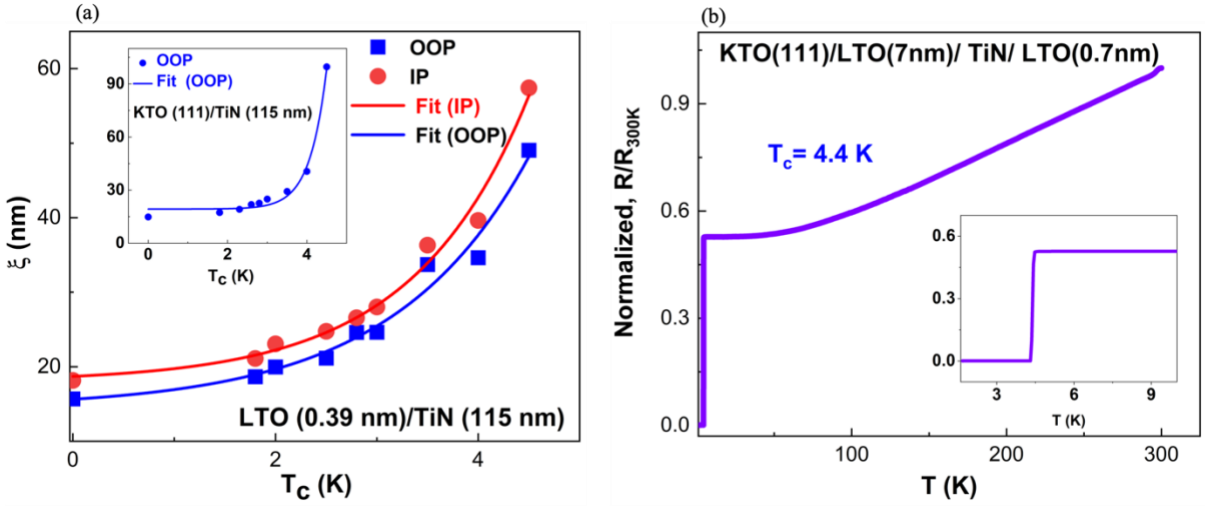

Figure S5. 7. (a) The coherence length of the KTO (111)/LTO (0.59 nm)/ TiN (115 nm) device, the inset shows the coherence length of the pristine KTO (111)/ TiN (115 nm) sample. (b) The temperature dependence of the normalized electrical resistance of KTO (111)/LTO (7 nm)/ TiN (115 nm)/ LTO (0.7 nm) device.

Fig. S5. 7(a) presents the coherence length as a function of the transition temperature in the bilayer heterostructure KTO (111)/LTO (0.59 nm)/TiN (115 nm) device, shown in both out-of-plane (OOP) and in-plane (IP) configurations. Fig. S5. 7(b) illustrates the temperature dependence of electrical resistance in the trilayer heterostructure (KTO/LTO/TiN/LTO), highlighting the superconducting transition temperature at Tc = 4.42 K.

6. Conclusions

This work presents a comprehensive study that integrates both experimental and theoretical findings, addressing multiple aspects of oxide thin film heterostructure interfaces. It begins with the epitaxial growth of high-quality thin films using state-of-the-art molecular beam epitaxy (MBE) techniques, followed by detailed structural and surface characterization through in-situ reflection high-energy electron diffraction (RHEED), high-resolution x-ray diffraction (XRD), x-ray photoelectron spectroscopy (XPS), and atomic force microscopy (AFM). The research thoroughly investigates the electrical and magnetic transport properties of these oxide-based interfaces using advanced low-temperature probes, including the physical property measurement system (Dynacol), Bluefors for millikelvin measurements, and the superconducting quantum interference device (SQUID) for magnetic characterization. The primary aim was to explore novel phenomena at oxide interfaces of ultra-thin film layers, specifically to identify candidates capable of exhibiting both interfacial superconductivity and ferromagnetism as potential alternatives to $SrTiO_3$-based systems.

Significantly, in late 2021, our results were the first to reveal the formation of two-dimensional electron gases (2DEGs) at (110)- and (111)-oriented $KTaO_3/LaTiO_3$interfaces, shown by a detailed thickness dependence study, in which we also estimated the critical thickness for the formation of 2DEGs at KTO/LTO interfaces. Here, $LaTiO_3$ (a Mott insulator) and $KTaO_3$ (a band insulator), where the strong spin-orbit coupling (SOC) from Ta atoms in $KTaO_3$ is more than an order of magnitude greater than that in $SrTiO_3$. Remarkably, we observed interfacial superconductivity at these 2DEGs with an onset temperature of 4 K and zero resistivity below 1 K, as shown in temperature-dependent resistivity measurements. The transition temperature surpasses that of $SrTiO_3$- based interfaces by more than an order of magnitude. Interestingly, unlike the previous reports, our results showed that the superconductivity is not only due to KTO side but is also due to the $LaTiO_3$ side, this is evidenced by the observation of non-monotonic behavior of the superconducting transition temperature (T_c) as function of the $LaTiO_3$ thickness, both T_c and I_c are peaked at an optimum

value of LTO thickness and below that thickness and above it they decreases taking a dome-like shape. This supports that superconductivity is a result of contributions from both KTO (Ta) and LTO (Ti) electrons.

Furthermore, our experiments provided robust evidence of emergent ferromagnetism in two dimensions along both (110)- and (111)-oriented 2DEGs at the KTO/LTO interfaces. This is supported by butterfly hysteresis magnetoresistance loops and out-of-plane magnetization hysteresis as well as x-ray magnetic circular dichroism (XMCD) at 2 K, which is attributed to an interface-induced ferromagnetism due to the strong spin-orbit coupling from KTO which gave rise to the observation of anomalous hall effect at KTO/LTO interfaces. The density functional theory calculations (DFT) attributed the origin of the ferromagnetism to the TiO_6-octahedral tilting Notably, the ferromagnetic 2DEGs exhibited high electron mobility, reaching ~250 $cm^2/V{\cdot}s$ at 2 K and ~20 $cm^2/V{\cdot}s$ at 300 K, marking these as the highest spin-polarized 2DEGs observed along these orientations. Most notably, our results indicate the exotic coexistence of ferromagnetism and superconductivity within the high-mobility, spin-polarized 2DEGs at the KTO/LTO interfaces, representing a significant advancement in the study of oxide heterostructures. We inspected the potential correlations of the observed phenomena with the structural properties of the KTO/LTO, in which we found that both KTO (110)/ LTO and KTO (111)/LTO imposes strains, the strain is pronounced at the interface which correlates with the trend of the anomalous hall resistivity in KTO/LTO. Interestingly, the KTO (100)/LTO interfaces did not show presence of significant strain, which may or may not have a relation with the absence of superconductivity at the KTO (100) surfaces, and interfaces.

We successfully grew high-quality heterostructure interfaces of $KTaO_3/LaTiO_3/TiN$ using in-situ transfer between oxide and nitride chambers. Despite the distinct environments (ozone and nitrogen plasma) and varying growth conditions, we achieved epitaxial single-phase growth along $KTaO_3$ (111) and KTO (100) substrates. We investigated the properties at the interface of a ferromagnetic oxide-based two-dimensional electron gas (2DEG) system (KTO/LTO) in proximity to a superconducting nitride layer (TiN) by adjusting the 2DEG layer thickness. TiN, a well-known candidate for disordered superconductivity, has recently been shown to support Cooper pairing above the transition temperature. Our experiments demonstrated the ability to tune the superconducting transition temperature (T_c) of TiN through

the KTO/LTO interfaces. Notably, we observed that thinner LTO layers corresponded to a higher T_c. Interestingly, however, our results revealed that a lower T_c coincided with a higher critical field (Hc), which is atypical. One possible explanation is the formation of a novel superconducting layer at the TiN interface, influenced by the proximity of the spin-polarized 2DEG layer.

7. Perspectives and Thoughts

It is very crucial for the future study to understand the mechanism of superconductivity and electron paring in the 2DEGs formed at (111) and (110) – oriented $KTaO_3$/ $LaTiO_3$ interfaces. The reason of the absence of superconductivity along (100) – oriented interfaces ambiguous and not fully understood, the debates still ongoing on this context. Our future study will be focusing on the understanding of the physical origin behind this puzzling absence of superconductivity in the 2DEGs at $KTaO_3$ (100)/ $LaTiO_3$ interfaces. Additionally, uncovering the mechanism of the superconductivity in $KTaO_3$ (110) and (111)/ $LaTiO_3$ interfaces.

It is essential to investigate the role of various functional perovskite overlayers as alternatives to the $LaTiO_3$ layer to assess their potential in inducing ferromagnetism and superconductivity at the interface with the $KTaO_3$ substrate. Candidates like $LaFeO_3$, $LaNiO_3$, and $EuTiO_3$ should be studied for comparison with $LaTiO_3$. This will help determine whether the strong spin-orbit coupling at the $KTaO_3$ interface is the sole mechanism responsible for the observed interfacial ferromagnetism or if other factors, such as structural influences, may also contribute.

As a PhD researcher and through the work that have been done in this thesis, through the experiments I conducted, the analyses I performed, and the data I interpreted, I have developed a strong conviction that the mechanisms responsible for ferromagnetism and the anomalous Hall effect at these interfaces are influenced not only by strong spin-orbit coupling but also by other critical factors. These include epitaxial growth, closely matched lattice constants, significant epitaxial strain, and the presence of two-dimensional conductivity.

To further explore this, we need to examine the effect of inserting another perovskite oxide layer between $KTaO_3$ and $LaTiO_3$, which could provide additional insight (see Fig. 7.1). Another intriguing question arises: if strong spin-orbit coupling is indeed the primary mechanism behind the observed interfacial ferromagnetism in $KTaO_3$/$LaTiO_3$ two-dimensional electron gases (2DEGs), would substituting $KTaO_3$ with another material exhibiting strong

spin-orbit coupling yield a similar effect? For instance, using Pt or Ta in place of $KTaO_3$ and combining them with $LaTiO_3$ or other perovskites like $LaFeO_3$ or $LaNiO_3$ could reveal more about the role of spin-orbit coupling and deepen our understanding of the mechanisms behind interface-induced ferromagnetism as shown in the schematics reprsented in Fig.7.1.

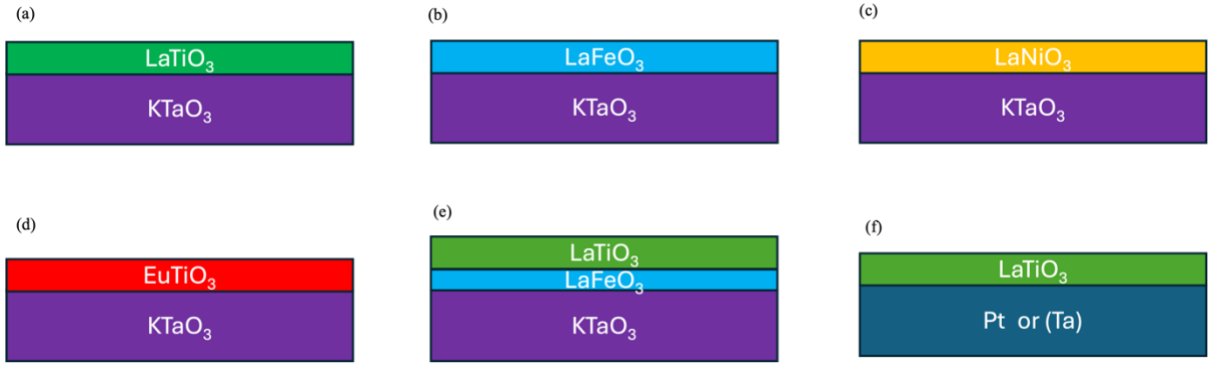

Figure 7. 1. Schematic of future planned study to understand the possible mechanism of the interface- induced ferromagnetism in KTO/LTO based interfaces (a) $KTaO_3/LaTiO_3$, (b) $KTaO_3/LaFeO_3$, (c) $KTaO_3/LaNiO_3$, (d) $KTaO_3/EuTiO_3$, (e) $KTaO_3/LaFeO_3/LaTiO_3$ and (f) Pt (Ta) /$LaTiO_3$ interfaces.

8. Contributions

Mostafa Marzouk and Stuart Parkin conceived the PhD projects, designed the experiments regularly discussed the plans and the results. Thin film samples were grown by Mostafa Marzouk using using state-of-the-art molecular beam epitaxy (Veeco GEN 10-MBE). Mostafa Marzouk also conducted *in-situ* RHEED analysis, structural characterizations (XRD, XRR, RSM, and ϕ-scans), surface topography investigations (AFM), and X-ray photoelectron spectroscopy (XPS) measurements. Electrical and magnetic transport measurements were performed by Mostafa Marzouk using the physical propert measurment systme (PPMS) and superconducting qunatum interference device (SQUID-MPMS3) system. Malli Tangi and Pierre Jean Zermatten helped in the initial calibration of the metal evaporation and ozone sources at the first run. Ilya Kostanovski conducted Rutherford backscattering spectrometry (RBS) measurements. Density functional theory (DFT) calculations were performed by Igor Maznichenko, Sergey Ostanin, and Arthur Ernst, following extensive discussions with Mostafa Marzouk, Banabir Pal, and Stuart Parkin. Katayoon Mohseni and Holger Meyerheim developed a fitting model for the truncation rod measurements obtained using a liquid Ga X-ray source. Ultra-low-temperature (millikelvin range) transport measurements were carried out by Banabir Pal and Mostafa Marzouk using a BlueFors system, and they jointly analyzed the data. Anupam Singh performed X-ray magnetic circular dichroism (XMCD) measurements at the ALBA Synchrotron and conducted the initial data analysis; interpretation of the XMCD results was performed collaboratively by Anupam Singh and Mostafa Marzouk. High-resolution scanning transmission electron microscopy (STEM) was conducted by Hakan Deniz on the KTO/LTO samples, with help form Norbert Schammelt in preparing thin lamellae via focused ion beam (FIB) milling.

For the oxide/nitride interface studies presented in Chapter 5, all thin films were also grown by Mostafa Marzouk using MBE, who also performed *in-situ* RHEED analysis, ex-situ AFM, and

X-ray diffraction characterizations. Mostafa Marzouk carried out the magnetic properties which were measured by SQUID MPMS3-VSM, and the electrical transport measurements which were conducted using Dynacol Quantum Design PPMS systems (9 T and 14 T). Hall bar patterning on the thin films was performed by Zhong Wang using photolithography techniques. Wenjie Zhang contributed to the AC (I–V) transport measurements, specifically measuring two KTO/LTO/TiN samples, which had initially been characterized by Mostafa Marzouk through DC transport measurements.

Mostafa Marzouk performed the comprehensive analysis and interpretation of all experimental results and for writing the thesis as well as the related manuscripts. Stuart Parkin supervised the overall project and the thesis preparation during the supervison of Mostafa throughout his PhD thesis work. Inna Vishik provided guidance to Mostafa, and she was engaged in regular scientific discussions.

Acknowledgments

First and foremost, I am profoundly grateful to the God, the eternal source of strength and guidance, especially during challenging times.

I am deeply grateful to my PhD supervisor, Stuart Parkin, for his unwavering support, guidance, and remarkable impact on both my career and personal growth. His mentorship and guidance have been invaluable in developing my critical thinking and introducing me to innovative research methods and life-management strategies. I am especially thankful for his patience and encouragement throughout this journey. Working within his esteemed group, under the leadership of one of the leading pioneers in materials physics, has been a true privilege. One aspect I particularly appreciate about Stuart is his openness—his door is always open for discussions, and he is an exceptionally flexible and supportive scientist. He has been like a father to me, guiding me in how to become a good scientist.

I also extend my heartfelt thanks to Inna Vishik for her continuous support, mentorship, and invaluable guidance. Her contributions have been pivotal in developing my scientific identity, enhancing my critical thinking, and refining my research skills. Thank you, Inna, for your profound impact on my PhD journey.

To my wife, Mirna, I owe my deepest heartfelt gratitude for her unconditional support, especially during the challenging moments of my PhD journey. Her encouragement has been a cornerstone of my resilience and success, I also thank her for reading my manuscripts and my thesis. The eternal source of support my family, especially my mother, I thank her so much for everything she did for us, I thnak my sister and my brother.

My sincere thanks go to Ruifeng Wang , my co-worker, for his kindness, professionalism, and his careful and very insightful feedback and thoughtful comments on my thesis. I am grateful to Malli Tangi, who taught me how to independently operate, manage, and maintain the MBE system, enabling me to take full responsibility for my sample growth within

the first four months of my PhD. I am thankful to Banabir Pal for the very fruitful collaboration and mentorship during my final year of the PhD, as well as for his meticulous review of my manuscripts. I also appreciate the valuable collaboration with Arthur Ernst, Igor Maznichenko, and Sergey Ostanin on the DFT calculations.

I appreciate the enriching discussions with Ke Zou, Niels Schröter. Special thanks to my colleagues at MPI-Halle —Swapna Mishra, Ajesh Gopi, Ke Gu, Yishen Xie, Jitul Deka, Anagha Mathew, Felix Küster, Atul Pandey, Kajal and Zhong Wang—for their camaraderie and support. I am sincerely grateful to Kristin Flieger for her unwavering support as a PhD coordinator. Her kindness means so much to me, and I deeply appreciate all that she has done. Thank you so much, Kristin! Lastly, I extend my gratitude to Sol Jackebesn, Mathew Gilbert, and Younghyuk Kim for their ongoing collaboration on the superconductivity mechanism in KTO/LTO interfaces. I finally thank Antje, Simone, Kristin, Michael, Mike, Julia, Katja, Frank, Pierre-Jean, Florian, Detlef, Hakan and Holger who were always there to happily introduce needed help and support. To my little family, thank you Mirna and to my whole family thank you so much for everything.

List of Publications

- **Mostafa I. S. Marzouk**, Anupam K. Singh, Igor Maznichenko, Malleswararao Tangi, Sergey Ostanin, Katayoon Mohseni, Ilya Kostanovsky, Pierre- Jean Zermatten, Holger L. Meyerheim, Arthur Ernst, Banabir Pal, and Stuart S.P. Parkin**,** Coexistence of Superconductivity and Ferromagnetism in Two-Dimensional Electron Gases at $KTaO_3/LaTiO_3$ Interfaces, Phys. Rev. Lett, (Submitted), (2024).
- K. Tiwari [λ], **Mostafa I. S. Marzouk**[λ], K. Xiao, M. Tangi and Stuart S.P. Parkin, Real space near-field imaging of Verwey transition in Fe_3O_4, ACS Nano, (submitted), (2024).
- **Mostafa Marzouk**, et al., Room temperature ferromagnetism driven by Ca-doped $BiFeO_3$ multiferroic functional material, J Mater Sci: Mater Electron 31, 5599 (2020). https://doi.org/10.1007/s10854-020-0312

- **Mostafa I. S. Marzouk**, Y. Kim, Morten Amundsen, M. Gilbert, B. Pal, Sol. Jackobsen, Stuart. S. P. Parkin, Unravelling the mechanism of superconductivity in two -dimensional elecgtron gases at $KTOaO_3/LaTiO_3$ interfaces. **In-preparation** (2024).
- **Mostafa I. S. Marzouk**, Swapna Mishra, A. Gopi, B. Pal, Stuart. S. P. Parkin, Josephson junctions based on oxide ferrimagnetic insulator. **In- preparation** (2024).
- **Mostafa I. S. Marzouk** and Stuart. S. P. Parkin., The role of spin-orbit coupling in ferromagentism evolution at eingnieered epitaxial oxide interfaces: $LaTiO_3$ and $LaFeO_3$ as a case study. **In preparation** (2024).
- **Mostafa I. S. Marzouk,** A. Gopi, B. Pal, Stuart Parkin, Tuning the metal-to insulator Verwey transition in Fe_3O_4 thin films grown by molecular beam epitaxy. **In preparation** (2024).

Curriculum Vitae

Mostafa Ibrahim Shehata Marzouk “Mostafa Marzouk”

Personal information

Nationality: Egyptian

EDUCATION

03/2021- 02/2025	Doctoral student; PhD researcher Max-Planck institute of Microstructure Physics (MPI- Halle) Martin-Luther university, Halle, Germany Dissertation ‘Interface- induced Ferromagnetism and Superconductivity in Two- Dimensional Electron Gases’ Supervisor: Prof. Dr. Stuart S. P. Parkin
2018- 2020	Master of Science in Physics, M. Sc., Helwan university, faculty of science, Cairo, Egypt Thesis: "Structural and magnetic study on doped $BiFeO_3$ in magnetic and electric sites as a Perovskite functional material"
2018 - 2019	M. Sc. Internship (Strasbourg, France), Institute of physics and chemistry of materials (IPCMS), Strasbourg university, Strasbourg- France, Advisor: Silviu Colis
2011- 2015	Bachelor of Science in Physics; B. Sc., Faculty of science, Helwan University, Cairo, Egypt

Scientific Activity

- A poster in, ICM: international conference on magnetism, Bologna, Italy, June (2024).
- PhD student talk, "Tunning of Disorder superconductivity in TiN interfaces", in Engineered Quantum Materials: US-German WE-Heraeus workshop, Bad Honnef, Germany, January, (2024).
- A poster in, Gordon Research conference (GRC): Superconductivity, Geneve, Switzerland, May (2023).
- Contributed talk in, Workshop of "Unconventional superconductivity", Munich (2022).
- Contributed talk (Coexistence of ferromagnetism and superconductivity at $KTaO_3/LaTiO_3$ interfaces, international workshop of oxide electronics, IWOE-30, Darmstadt, Germany, September (2024).
- Contributed talk in, SUPERMAX - International Workshop on Superconductivity & Magnetism in f-Electron Quantum Materials under Extreme Conditions, Toulouse, France, October (2024).
- An accepted poster in GRC superconductivity May 2025, Geneve (2025).

Erklärung

Hiermit erkläre ich, Mostafa Marzouk, die vorliegende Arbeit **"Interface- Induced Ferromagnetism and Superconductivity in Two- Dimensional Electron Gases"** selbständig und ohne fremde Hilfe verfasst zu haben. Es wurden keine anderen als die von mir angegebenen Quellen und Hilfsmittel benutzt. Die den benutzen Werken wörtlich oder inhaltlich entnommenen Stellen sind als solche kenntlich gemacht worden. Ich erkläre, die Angaben wahrheitsgemäß gemacht, keine vergeblichen Promotionsversuche unternommen und keine Dissertation an einer anderen wissenschaftlichen Einrichtung zur Erlangung eines akademischen Grades eingereicht zu haben. Ich bin weder vorbestraft noch sind gegen mich Ermittlungsverfahren anhängig.

Halle (Saale), den 19.1.2024

Mostafa Marzouk

References

[1] N. F. Mott and R. Peierls, Proc. Phys. Soc. 49, 72 (1937).

[2] N. F. Mott, Proc. Phys. Soc. A 62, 416 (1949).

[3] N. F. Mott, Rev Mod Phys 40, 677 (1968).

[4] J. H. d. Boer and E. J. W. Verwey, Proc. Phys. Soc. 49, 59 (1937).

[5] J. Hubbard, Proc. R. Soc. Lond. A 276, 238 (1963).

[6] M. T. Greiner and Z.-H. Lu, NPG Asia Materials 5, e55 (2013).

[7] J. Zaanen, G. A. Sawatzky, and J. W. Allen, Phys. Rev. Lett. 55, 418 (1985).

[8] C. Biz, J. Gracia, and M. Fianchini, Int J Mol Sci 23 (2022).

[9] Y. Deng, J. Phys. Conf. Ser. 2386 (2022).

[10] Z. Trabelsi, E. Hannachi, S. A. Alotaibi, Y. Slimani, M. A. Almessiere, and A. Baykal, in *Superconducting Materials: Fundamentals, Synthesis and Applications*, edited by Y. Slimani, and E. Hannachi (Springer Nature Singapore, Singapore, 2022), pp. 1.

[11] A. Ohtomo and H. Y. Hwang, Nature 427, 423 (2004).

[12] N. Reyren, S. Thiel, A. D. Caviglia, L. F. Kourkoutis, G. Hammerl, C. Richter, C. W. Schneider, T. Kopp, A. S. Ruetschi, D. Jaccard, M. Gabay, D. A. Muller, J. M. Triscone, and J. Mannhart, Science 317, 1196 (2007).

[13] C. Liu, X. Yan, D. Jin, Y. Ma, H. W. Hsiao, Y. Lin, T. M. Bretz-Sullivan, X. Zhou, J. Pearson, B. Fisher, J. S. Jiang, W. Han, J. M. Zuo, J. Wen, D. D. Fong, J. Sun, H. Zhou, and A. Bhattacharya, Science 371, 716 (2021).

[14] Z. Chen, Z. Liu, Y. Sun, X. Chen, Y. Liu, H. Zhang, H. Li, M. Zhang, S. Hong, T. Ren, C. Zhang, H. Tian, Y. Zhou, J. Sun, and Y. Xie, Phys. Rev. Lett. 126, 026802 (2021).

[15] K. M. Bastiaans, D. Chatzopoulos, J. F. Ge, D. Cho, W. O. Tromp, J. M. van Ruitenbeek, M. H. Fischer, P. J. de Visser, D. J. Thoen, E. F. C. Driessen, T. M. Klapwijk, and M. P. Allan, Science 374, 608 (2021).

[16] S. Ran, Chris Eckberg, Qing-Ping Ding, Yuji Furukawa, Tristin Metz , Shanta R. Saha, I-Lin Liu, Mark Zic, Hyunsoo Kim, Johnpierre Paglione, and N. P. Butch, Science (2018).

[17] Y. Tokunaga, Japanese atomic energy agency (2019).

[18] Y. Tokunaga, H. Sakai, S. Kambe, T. Hattori, N. Higa, G. Nakamine, S. Kitagawa, K. Ishida, A. Nakamura, Y. Shimizu, Y. Homma, D. Li, F. Honda, and D. Aoki, J. Phys. Soc. Jpn. 88 (2019).

[19] F. Baiutti, G. Christiani, and G. Logvenov, Beilstein J Nanotechnol 5, 596 (2014).

[20] M. Knudsen, Annalen der Physik 28, 75 (1909).

[21] M. Buchner, K. Höfler, B. Henne, V. Ney, and A. Ney, J. Appl. Phys. 124 (2018).

[22] G. Schutz, W. Wagner, W. Wilhelm, P. Kienle, R. Zeller, R. Frahm, and G. Materlik, Phys. Rev. Lett. 58, 737 (1987).

[23] G. Shibata, C. Won, J. Kim, Y. Nonaka, K. Ikeda, Y. Wan, M. Suzuki, T. Koide, A. Tanaka, S.-W. Cheong, and A. Fujimori, J. Phys. Chem. C 125, 12929 (2021).

[24] P. Moetakef, T. A. Cain, D. G. Ouellette, J. Y. Zhang, D. O. Klenov, A. Janotti, C. G. Van de Walle, S. Rajan, S. J. Allen, and S. Stemmer, Appl. Phys. Lett. 99 (2011).

[25] J. Son, P. Moetakef, B. Jalan, O. Bierwagen, N. J. Wright, R. Engel-Herbert, and S. Stemmer, Nat Mater 9, 482 (2010).

[26] A. Annadi, Q. Zhang, X. R. Wang, N. Tuzla, K. Gopinadhan, W. M. Lü, A. R. Barman, Z. Q. Liu, A. Srivastava, S. Saha, Y. L. Zhao, S. W. Zeng, S. Dhar, E. Olsson, B. Gu, S. Yunoki, S. Maekawa, H. Hilgenkamp, T. Venkatesan, and Ariando, Nat. Commun. 4 (2013).

[27] N. Reyren, S. Thiel, A. D. Caviglia, L. F. Kourkoutis, G. Hammerl, C. Richter, C. W. Schneider, T. Kopp, A. S. Ruetschi, D. Jaccard, M. Gabay, D. A. Muller, J. M. Triscone, and J. Mannhart, Science 317, 1196 (2007).

[28] Y. L. Han, S. C. Shen, J. You, H. O. Li, Z. Z. Luo, C. J. Li, G. L. Qu, C. M. Xiong, R. F. Dou, L. He, D. Naugle, G. P. Guo, and J. C. Nie, Appl. Phys. Lett. 105 (2014).

[29] K. Ahadi, L. Galletti, Y. T. Li, S. Salmani-Rezaie, W. Z. Wu, and S. Stemmer, Sci. Adv. 5 (2019).

[30] S. Salmani-Rezaie, L. Galletti, T. Schumann, R. Russell, H. Jeong, Y. T. Li, J. W. Harter, and S. Stemmer, Appl. Phys. Lett. 118 (2021).

[31] J. Biscaras, N. Bergeal, S. Hurand, C. Grossetête, A. Rastogi, R. C. Budhani, D. LeBoeuf, C. Proust, and J. Lesueur, Phys. Rev. Lett. 108 (2012).

[32] J. Biscaras, N. Bergeal, A. Kushwaha, T. Wolf, A. Rastogi, R. C. Budhani, and J. Lesueur, Nat. Commun. 1 (2010).

[33] S. Thiel, G. Hammerl, A. Schmehl, C. W. Schneider, and J. Mannhart, Science 313, 1942 (2006).

[34] R. Erlandsen, R. T. Dahm, F. Trier, M. Scuderi, E. Di Gennaro, A. Sambri, C. K. R. Kirchert, N. Pryds, F. M. Granozio, and T. S. Jespersen, Nano. Lett. 22, 4758 (2022).

[35] G. Herranz, G. Singh, N. Bergeal, A. Jouan, J. Lesueur, J. Gázquez, M. Varela, M. Scigaj, N. Dix, F. Sanchez, and J. Fontcuberta, Nat. Commun. 6 (2015).

[36] A. D. Caviglia, M. Gabay, S. Gariglio, N. Reyren, C. Cancellieri, and J. M. Triscone, Phys. Rev. Lett. 104, 126803 (2010).

[37] G. Singh, C. Guarcello, E. Lesne, D. Winkler, T. Claeson, T. Bauch, F. Lombardi, A. D. Caviglia, R. Citro, M. Cuoco, and A. Kalaboukhov, npj Quant Mater. 7 (2022).

[38] J. A. Bert, B. Kalisky, C. Bell, M. Kim, Y. Hikita, H. Y. Hwang, and K. A. Moler, Nat. Phys. 7, 767 (2011).

[39] D. A. Dikin, M. Mehta, C. W. Bark, C. M. Folkman, C. B. Eom, and V. Chandrasekhar, Phys. Rev. Lett. 107 (2011).

[40] L. Li, C. Richter, J. Mannhart, and R. C. Ashoori, Nat. Phys. 7, 762 (2011).

[41] K. Zou, S. Ismail-Beigi, K. Kisslinger, X. Shen, D. Su, F. J. Walker, and C. H. Ahn, APL Mater. 3 (2015).

[42] H. R. Zhang, Y. Yun, X. J. Zhang, H. Zhang, Y. Ma, X. Yan, F. Wang, G. Li, R. Li, T. Khan, Y. S. Chen, W. Liu, F. X. Hu, B. G. Liu, B. G. Shen, W. Han, and J. R. Sun, Phys. Rev. Lett. 121 (2018).

[43] Z. Chen, Z. R. Liu, Y. Q. Sun, X. X. Chen, Y. Liu, H. Zhang, H. K. Li, M. Zhang, S. Y. Hong, T. S. Ren, C. Zhang, H. Tian, Y. Zhou, J. R. Sun, and Y. W. Xie, Phys. Rev. Lett. 126 (2021).

[44] Z. Zhang, W. Jiang, T. Shao, Y. Qiao, X. Chen, Q. Zhao, M. Chen, R. Dou, C. Xiong, and J. Nie, New J. Phys. 25 (2023).

[45] C. Liu, X. Zhou, D. Hong, B. Fisher, H. Zheng, J. Pearson, J. S. Jiang, D. Jin, M. R. Norman, and A. Bhattacharya, Nat. Commun. 14, 951 (2023).

[46] L. M. Vicente-Arche, J. Bréhin, S. Varotto, M. Cosset-Cheneau, S. Mallik, R. Salazar, P. Noël, D. C. Vaz, F. Trier, S. Bhattacharya, A. Sander, P. Le Fèvre, F. Bertran, G. Saiz, G. Ménard, N. Bergeal, A. Barthélémy, H. Li, C. C. Lin, D. E. Nikonov, I. A. Young, J. E. Rault, L. Vila, J. P. Attane, and M. Bibes, Adv. Mater. 33 (2021).

[47] T. S. Ren, M. C. Li, X. K. Sun, L. L. Ju, Y. Liu, S. Y. Hong, Y. Q. Sun, Q. Tao, Y. Zhou, Z. A. Xu, and Y. W. Xie, Sci. Adv. 8 (2022).

[48] H. Zhang, H. R. Zhang, X. Yan, X. J. Zhang, Q. H. Zhang, J. Zhang, F. R. Han, L. Gu, B. G. Liu, Y. S. Chen, B. G. Shen, and J. R. Sun, Acs Appl. Mater. Interf. 9, 36456 (2017).

[49] P. D. King, R. H. He, T. Eknapakul, P. Buaphet, S. K. Mo, Y. Kaneko, S. Harashima, Y. Hikita, M. S. Bahramy, C. Bell, Z. Hussain, Y. Tokura, Z. X. Shen, H. Y. Hwang, F. Baumberger, and W. Meevasana, Phys. Rev. Lett. 108, 117602 (2012).

[50] J. A. M. van Ostaay, A. R. Akhmerov, and C. W. J. Beenakker, Phys. Rev. B 83 (2011).

[51] H. Nakamura and T. Kimura, Phys. Rev. B 80 (2009).

[52] D.A. Crandles and J. D. G. a. J. E. G. T. Timusk, Physica C (1992).

[53] D. Maryenko, I. V. Maznichenko, S. Ostanin, M. Kawamura, K. S. Takahashi, M. Nakamura, V. K. Dugaev, E. Y. Sherman, A. Ernst, and M. Kawasaki, APL Mater. 11 (2023).

[54] I. V. Maznichenko, S. Ostanin, D. Maryenko, V. K. Dugaev, E. Y. Sherman, P. Buczek, I. Mertig, M. Kawasaki, and A. Ernst, Phys. Rev. Lett 132, 216201 (2024).

[55] M. J. Hÿtch, E. Snoeck, and R. Kilaas, Ultramicroscopy 74, 131 (1998).

[56] L. Ranalli, C. Verdi, L. Monacelli, G. Kresse, M. Calandra, and C. Franchini, Adv. Quantum Technol. 6 (2023).

[57] H. Fujishita, S. Kitazawa, M. Saito, R. Ishisaka, H. Okamoto, and T. Yamaguchi, J. Phys. Soc. Jpn. 85 (2016).

[58] A. Brinkman, M. Huijben, M. van Zalk, J. Huijben, U. Zeitler, J. C. Maan, W. G. van der Wiel, G. Rijnders, D. H. Blank, and H. Hilgenkamp, Nat Mater 6, 493 (2007).

[59] F. Wen, Y. Cao, X. Liu, B. Pal, S. Middey, M. Kareev, and J. Chakhalian, Appl. Phys. Lett. 112 (2018).

[60] J. Bréhin, Y. Chen, M. D'Antuono, S. Varotto, D. Stornaiuolo, C. Piamonteze, J. Varignon, M. Salluzzo, and M. Bibes, Nat. Phys. 19, 823 (2023).

[61] J. S. Lee, Y. W. Xie, H. K. Sato, C. Bell, Y. Hikita, H. Y. Hwang, and C. C. Kao, Nat Mater 12, 703 (2013).

[62] D. Stornaiuolo, C. Cantoni, G. M. De Luca, R. Di Capua, E. Di Gennaro, G. Ghiringhelli, B. Jouault, D. Marrè, D. Massarotti, F. M. Granozio, I. Pallecchi, C. Piamonteze, S. Rusponi, F. Tafuri, and M. Salluzzo, Nat Mater 15, 278 (2016).

[63] F. Gunkel, C. Bell, H. Inoue, B. Kim, A. G. Swartz, T. A. Merz, Y. Hikita, S. Harashima, H. K. Sato, M. Minohara, S. Hoffmann-Eifert, R. Dittmann, and H. Y. Hwang, Phys. Rev. X 6 (2016).

[64] K. Ahadi, L. Galletti, Y. T. Li, S. Salmani-Rezaie, W. Z. Wu, and S. Stemmer, Sci. Adv. 5 (2019).

[65] Y. L. Han, S. C. Shen, J. You, H. O. Li, Z. Z. Luo, C. J. Li, G. L. Qu, C. M. Xiong, R. F. Dou, L. He, D. Naugle, G. P. Guo, and J. C. Nie, Appl. Phys. Lett. 105 (2014).

[66] J. A. Bert, B. Kalisky, C. Bell, M. Kim, Y. Hikita, H. Y. Hwang, and K. A. Moler, Nat. Phys. 7, 767 (2011).

[67] H. Zhang, H. R. Zhang, X. Yan, X. J. Zhang, Q. H. Zhang, J. Zhang, F. R. Han, L. Gu, B. G. Liu, Y. S. Chen, B. G. Shen, and J. R. Sun, ACS Appl. Mater. Interfaces. 9, 36456 (2017).

[68] K. Rubi, S. Zeng, F. Bangma, M. Goiran, A. Ariando, W. Escoffier, and U. Zeitler, Phys. Rev. Res. 3, 033234 (2021).

[69] H. R. Zhang, Y. Yun, X. J. Zhang, H. Zhang, Y. Ma, X. Yan, F. Wang, G. Li, R. Li, T. Khan, Y. S. Chen, W. Liu, F. X. Hu, B. G. Liu, B. G. Shen, W. Han, and J. R. Sun, Phys. Rev. Lett. 121 (2018).

[70] Y. T. Zou, H. Shin, H. R. Wei, Y. Y. Fan, B. A. Davidson, E. J. Guo, Q. H. Chen, K. Zou, and Z. G. Cheng, Npj Quantum Mater 7 (2022).

[71] C. J. Liu, X. Yan, D. F. Jin, Y. Ma, H. W. Hsiao, Y. L. Lin, T. M. Bretz-Sullivan, X. J. Zhou, J. Pearson, B. Fisher, J. S. Jiang, W. Han, J. M. Zuo, J. G. Wen, D. D. Fong, J. R. Sun, H. Zhou, and A. Bhattacharya, Science 371, 716 (2021).

[72] P. D. C. King, R. H. He, T. Eknapakul, P. Buaphet, S. K. Mo, Y. Kaneko, S. Harashima, Y. Hikita, M. S. Bahramy, C. Bell, Z. Hussain, Y. Tokura, Z. X. Shen, H. Y. Hwang, F. Baumberger, and W. Meevasana, Phys. Rev. Lett. 108 (2012).

[73] G. E. Jellison, I. Paulauskas, L. A. Boatner, and D. J. Singh, Phys. Rev. B 74 (2006).

[74] V. Fritsch, J. Hemberger, M. V. Eremin, H. A. Krug von Nidda, F. Lichtenberg, R. Wehn, and A. Loidl, Phys. Rev. B 65 (2002).

[75] J. P. Goral and J. E. Greedan, J Magn Magn Mater 37, 315 (1983).

[76] M. Mochizuki and M. Imada, J Phys Soc Jpn 70, 2872 (2001).

[77] B. Keimer, D. Casa, A. Ivanov, J. W. Lynn, M. Zimmermann, J. P. Hill, D. Gibbs, Y. Taguchi, and Y. Tokura, Phys. Rev. Lett. 85, 3946 (2000).

[78] C. Ulrich, A. Gossling, M. Gruninger, M. Guennou, H. Roth, M. Cwik, T. Lorenz, G. Khaliullin, and B. Keimer, Phys. Rev. Lett. 97, 157401 (2006).

[79] A. Tkach, P. M. Vilarinho, and A. Almeida, J. Euro. Cer. Soc. 31, 2303 (2011).

[80] A. H. Al-Tawhid, J. Kanter, M. Hatefipour, D. L. Irving, D. P. Kumah, J. Shabani, and K. Ahadi, J. Electron. Mater. 51, 7073 (2022).

[81] G. van der Laan and A. I. Figueroa, Coordin Chem Rev 277, 95 (2014).

[82] H. Leng, K. Xu, H. Tian, Y. He, Y. Zhao, M. Xu, X. Yu, M. B. H. Breese, H. Zhang, Z. Liu, D. Shen, X. Wu, J. Yi, and L. Qiao, Appl. Phys. Lett. 124 (2024).

[83] J. S. White, M. Bator, Y. Hu, H. Luetkens, J. Stahn, S. Capelli, S. Das, M. Dobeli, T. Lippert, V. K. Malik, J. Martynczuk, A. Wokaun, M. Kenzelmann, C. Niedermayer, and C. W. Schneider, Phys. Rev. Lett. 111, 037201 (2013).

[84] C. W. Schneider, S. Mukherjee, K. Shimamoto, S. Das, H. Luetkens, J. S. White, M. Bator, Y. Hu, J. Stahn, T. Prokscha, A. Suter, Z. Salman, M. Kenzelmann, T. Lippert, and C. Niedermayer, Phys. Rev. B 94 (2016).

[85] I. V. Maznichenko, S. Ostanin, D. Maryenko, V. K. Dugaev, E. Y. Sherman, P. Buczek, I. Mertig, M. Kawasaki, and A. Ernst, Phys. Rev. Lett. 132, 216201 (2024).

[86] L. J. v. d. Pauw, Philips Techn. Rev. 20, 220 (1958).

[87] G. Kresse and J. Furthmuller, Phys. Rev. B Condens. Matter 54, 11169 (1996).

[88] J. P. Perdew, K. Burke, and M. Ernzerhof, Phys. Rev. Lett. 77, 3865 (1996).

[89] G. K. D. Hobbs, J. Hafner, Phys. Rev. B (2000).

[90] V. V. Anisimov, J. Zaanen, and O. K. Andersen, Phys. Rev. B 44, 943 (1991).

[91] H. Meissner, Phys. Rev. 117, 672 (1960).

[92] R. Holm and W. Meissner, Z Phys 74, 715 (1932).

[93] A. I. Buzdin, Rev. Mod. Phys. 77, 935 (2005).

[94] Z. Sefrioui, D. Arias, V. Peña, J. E. Villegas, M. Varela, P. Prieto, C. León, J. L. Martinez, and J. Santamaria, Phys. Rev. B 67 (2003).

[95] J. Wang, M. Singh, M. Tian, N. Kumar, B. Liu, C. Shi, J. K. Jain, N. Samarth, T. E. Mallouk, and M. H. W. Chan, Nat. Phys. 6, 389 (2010).

[96] R. Yan, G. Khalsa, S. Vishwanath, Y. Han, J. Wright, S. Rouvimov, D. S. Katzer, N. Nepal, B. P. Downey, D. A. Muller, H. G. Xing, D. J. Meyer, and D. Jena, Nature 555, 183 (2018).

[97] Y. Song, Z. Chen, Q. Zhang, H. Xu, X. Lou, X. Chen, X. Xu, X. Zhu, R. Tao, T. Yu, H. Ru, Y. Wang, T. Zhang, J. Guo, L. Gu, Y. Xie, R. Peng, and D. Feng, Nat. Commun. 12, 5926 (2021).

[98] J. F. Ge, Z. L. Liu, C. Liu, C. L. Gao, D. Qian, Q. K. Xue, Y. Liu, and J. F. Jia, Nat Mater 14, 285 (2015).

[99] Q. Zou, M. Fu, Z. Wu, L. Li, D. S. Parker, A. S. Sefat, and Z. Gai, Npj Quantum Mater 6 (2021).

[100] J. Liang, Y. J. Zhang, X. Yao, H. Li, Z. X. Li, J. Wang, Y. Chen, and I. K. Sou, Proc Natl Acad Sci U S A 117, 221 (2020).

[101] M. Hubener, D. Tikhonov, I. A. Garifullin, K. Westerholt, and H. Zabel, J. Condens. Matter Phys. 14, 8687 (2002).

[102] M. Mochizuki and M. Imada, Phys. Rev. Lett. 91, 167203 (2003).

[103] M. Mochizuki and M. Imada, J. Phys. Soc. Jpn. 70, 2872 (2001).

[104] C. He, T. D. Sanders, M. T. Gray, F. J. Wong, V. V. Mehta, and Y. Suzuki, Phys. Rev. B 86 (2012).

[105] T. T. Zhang, C. Y. Gu, Z. W. Mao, X. F. Chen, Z. B. Gu, P. Wang, Y. F. Nie, and X. Q. Pan, Appl. Phys. Lett. 115 (2019).

[106] E. N. Jin, L. Kornblum, D. P. Kumah, K. Zou, C. C. Broadbridge, J. H. Ngai, C. H. Ahn, and F. J. Walker, APL Materials 2 (2014).

[107] F. Lichtenberg, D. Widmer, J. G. Bednorz, T. Williams, and A. Reller, Z Phys B Con Mat 82, 211 (1991).

[108] J. P. Goral and J. E. Greedan, Journal of Magnetism and Magnetic Materials 37, 315 (1983).

[109] J. Hemberger, H. A. Krug von Nidda, V. Fritsch, J. Deisenhofer, S. Lobina, T. Rudolf, P. Lunkenheimer, F. Lichtenberg, A. Loidl, D. Bruns, and B. Buchner, Phys. Rev. Lett. 91, 066403 (2003).

[110] U. S. Pracht, M. Scheffler, M. Dressel, D. F. Kalok, C. Strunk, and T. I. Baturina, Phys. Rev. B 86 (2012).

[111] S. Yadav, V. Kaushik, M. P. Saravanan, R. P. Aloysius, V. Ganesan, and S. Sahoo, Sci. Rep. 11, 7888 (2021).

[112] B. T. Matthias, T. H. Geballe, and V. B. Compton, Rev Mod Phys 35, 1 (1963).

[113] M. I. Faley, Y. Liu, and R. E. Dunin-Borkowski, Nanomaterials 11 (2021).

[114] Y. Krockenberger, S.-i. Karimoto, H. Yamamoto, and K. Semba, J. Appl. Phys. 112 (2012).

[115] B. Sacepe, C. Chapelier, T. I. Baturina, V. M. Vinokur, M. R. Baklanov, and M. Sanquer, Phys. Rev. Lett 101, 157006 (2008).

[116] R. Crane, N. P. Armitage, A. Johansson, G. Sambandamurthy, D. Shahar, and G. Grüner, Phys. Rev. B 75 (2007).

[117] V. M. Galitski and A. I. Larkin, Phys. Rev. Lett. 87, 087001 (2001).

[118] M.Tinkham, *Introduction to Superconductivity* (Dover Publications, Mineola, NY, 2004), Vol. 2nd edition.

[119] S. Das, A. Rastogi, L. Wu, J.-C. Zheng, Z. Hossain, Y. Zhu, and R. C. Budhani, Phys. Rev. B 90 (2014).

[120] F. D. Wen, Y. W. Cao, X. R. Liu, B. Pal, S. Middey, M. Kareev, and J. Chakhalian, Appl. Phys. Lett. 112 (2018).

[121] C. A. Jackson and S. Stemmer, Phys. Rev. B 88 (2013).

[122] N. Reyren, M. Bibes, E. Lesne, J. M. George, C. Deranlot, S. Collin, A. Barthelemy, and H. Jaffres, Phys. Rev. Lett. 108, 186802 (2012).

[123] A. Ghosal, M. Randeria, and N. Trivedi, Phys. Rev. B 65 (2001).

[124] Y. Dubi, Y. Meir, and Y. Avishai, Nature 449, 876 (2007).

[125] B. Sacepe, C. Chapelier, T. I. Baturina, V. M. Vinokur, M. R. Baklanov, and M. Sanquer, Nat. Commun. 1, 140 (2010).

[126] M. Bristow, W. Knafo, P. Reiss, W. Meier, P. C. Canfield, S. J. Blundell, and A. I. Coldea, Phys. Rev. B 101 (2020).